An Updated High Precision Measurement of the Neutral Pion Lifetime via the Primakoff Effect

December 10, 2007

A. Gasparian (spokesperson and contact person), P. Ambrozewicz, R. Pedroni
North Carolina A&T State University, Greensboro, NC

P. Martel, D. McNulty, R. Miskimen (spokesperson), A. Teymurazyan
University of Massachusetts, Amherst, MA

D. Dale (spokesperson), P. Cole, T. Forest, O. Kosinov, D.P. Wells
Idaho State University, Pocatello, ID

E. Chudakoff, H. Egiyan, V. Gyurjyan, M. Ito (spokesperson), J.P. Chen, Y. Sharabian, E. Smith
V. Kubarovsky, D. Lawrence, A. Deur
Thomas Jefferson National Accelerator Facility, Newport News, VA

L. Gan (spokesperson), T. Black, X. Li, L. Jiang
University of North Carolina Wilmington, Wilmington, NC

A.M. Bernstein, S. Kowalski
Massachusetts Institute of Technology, Cambridge, MA

D. Sober, H. Crannell, R. Hakobyan, F. Klein, P. Nadel-Turonski
The Catholic University of America, Washington, DC

A. Afanasev, M. Christy, J. Goity, P. Gueye, C. Keppel, L. Tang, L. Yuan
Hampton University, Hampton, VA

E. Clinton
Duke University, Durham, NC

M. Dugger, E. Pasyuk, B.G. Ritchie
Arizona State University, Tempe, AZ

M. Kubantsev
Northwestern University, Evanston/Chicago, IL

A. Asratyan, O. Chernyshov, G. Davidenko, A. Dolgolenko, G. Dzyubenko, V. Goryachev, A. Kamenskii, I. Larin, V. Matveev, V. Semyachkin, A. Sitnikov, V. Verebryusov, V. Vishnyakov
Institute for Theoretical and Experimental Physics, Moscow, Russia

Yu. Goncharenko, A. Meschanin, L. Soloviev, A. Vasiliev, V. Mochalov
Institute for High Energy Physics, Protvino, Russia

M. Khandaker, V. Punjabi, C. Salgado
Norfolk State University, Norfolk, VA

A. Glamazdin, M. Konchatnyi, A. Korchin
Kharkov Institute of Physics and Technology, Kharkov, Ukraine

C. Li, Y. Fu, J. Zhou, J. Feng, S. Zhou
Chinese Institute of Atomic Energy, Beijing, China

B. Ma, Y. Mao
Beijing University, Beijing, China

J. He
Institute of High Energy Physics, Chinese Academy of Sciences, Beijing, China

B. Hu, X. Zhang, W. Luo, L. Ma, Z. Liu
Lanzhou university, Lanzhou , China

W. Briscoe
George Washington University, Washington, DC

S. Gevorkyan, A. Tarasov
Joint Institute for Nuclear Research, Dubna, Russia

I. Aznauryan, A. Margaryan,
H. Voskanyan, A. Ketikyan, A. Shahinyan, A. Petrosyan
Yerevan Physics Institute, Yerevan, Armenia

T.E. Rodrigues
University of São Paulo, São Paulo, Brazil

K. Baker
Yale University, New Haven, CT

I. Nagakawa
RIKEN, Wako, Saitama, JAPAN

H. Lu, X. Yan, Y. Ye, P. Zhu, Y. Jiang
University of Science and Technology of China, Hefei, China

M. Wood
Canisius College, Buffalo, NY

Contents

Abstract

The *PrimEx* Collaboration has proposed to perform a high precision measurement of the two photon decay width of the neutral pion ($\Gamma_{\pi^o \rightarrow \gamma\gamma}$). This measurement will provide a stringent test of the predictions of the U(1) axial anomaly in quantum chromodynamics. The first experimental data set was collected in 2004. A new level of experimental precision has been achieved by using the high intensity and high resolution photon tagging facility in Hall B of Jefferson Lab, and by developing and constructing a state-of-the-art, high resolution electromagnetic calorimeter. A preliminary result on the π^0 lifetime with a precision of $\sim 3\%$ was released at the American Physical Society April meeting in 2007 through an invited presentation as well as at an American Institute of Physics press conference. The desired precision on this measurement is driven by the precision of recently available theoretical calculations performed both in the context of chiral perturbation theory and the QCD sum rule approach. Here, we discuss the analysis status of the existing data and the improvement which can be made with a future run, and thereby request from PAC33 an extension of the π^0 lifetime measurement to reach the ultimate goal of $\simeq$1.4% accuracy.

1 Motivation

An effect of color confinement in quantum chromodynamics (QCD) is that traditional perturbation theory breaks down at large distances and low energies. A quantitative understanding of the strong interaction in this region remains one of the greatest intellectual challenges in physics. Symmetries of QCD in the chiral limit (massless quarks) provide a promising framework for resolving this problem. As the lightest particle in the hadron spectrum, the neutral pion represents the most sensitive platform to study fundamental symmetry issues in quantum chromodynamics at low energy. Spontaneous chiral symmetry breaking gives birth to the π^0 as one of the Goldstone particles and the chiral axial anomaly primarily determines the π^0 lifetime. As such, a precision measurement of the lifetime of the π^0 will provide a fundamental test of QCD at the confinement scale.

2 Theoretical Developments

The two-photon decay mode of the π^0 reveals one of the most profound symmetry issues in quantum chromodynamics, namely, the explicit breaking of a classical symmetry by the quantum fluctuations of the quark fields coupling to a gauge field[1]. This phenomenon, called anomalous symmetry breaking, is of pure quantum mechanical origin. In QCD, there are several observable phenomena that originate from anomalies. One is connected with the couplings of the quarks to the gluons. This is the so called axial anomaly by which the conservation of the axial U(1) symmetry of the classical Lagrangian of QCD is broken even in the limit where two or more quarks are massless, and the so called anomalous divergence of the corresponding axial-vector current becomes proportional to the product $\vec{E}^a \cdot \vec{B}^a$ of the chromo-electric and chromo-magnetic fields. The axial anomaly of interest to us involves the corresponding coupling of the quarks to photons[2]. In the limit of exact isospin symmetry, the π^o couples only to the isotriplet axial-vector current $\bar{q}I_3\gamma_\mu\gamma_5 q$, where $q = (u,\ d)$, and I_3 is the third isospin generator. If we limit ourselves to two quark flavors, the electromagnetic current is given by $\bar{q}(1/6 + I_3/2)\gamma_\mu q$. When coupling to the photon, the isosinglet and isotriplet components of the electromagnetic current lead to an anomaly that explicitly breaks the symmetry associated with the axial-vector current $\bar{q}\ I_3\ \gamma_\mu\gamma_5\ q$, and this in turn directly affects the coupling of the π^o to two photons. The conservation of the axial U(1) current, to which the η' meson couples, as well as the $\bar{q}\frac{1}{2}\lambda_8\gamma_\mu\gamma_5 q$, to which the η meson couples, are similarly affected by the electromagnetic field.

In the limit of vanishing quark masses, the anomaly leads to the $\pi^0 \to \gamma\gamma$ decay amplitude [1, 2]:

$$\mathcal{A}(\pi^0 \to \gamma\gamma) = \frac{\alpha_{em}}{4\pi F_\pi}\epsilon_{\mu\nu\rho\sigma}k^\mu k'^\nu \epsilon^{*\rho}\epsilon^{*\sigma}, \tag{1}$$

or the reduced amplitude,

$$A_{\gamma\gamma} = \frac{\alpha_{em}}{\pi F_\pi} = 2.513 \cdot 10^{-2} GeV^{-1} \tag{2}$$

where $F_\pi = 92.42 \pm 0.25 MeV$ [3] is the pion decay constant, and k and ϵ are respectively photon momenta and polarization vectors.

The width of the $\pi^o \to \gamma\gamma$ decay predicted by this amplitude is

$$\Gamma = M_\pi^3 \frac{| A_{\gamma\gamma} |^2}{64\pi} = 7.725 \pm 0.044 eV, \tag{3}$$

with a 0.6% uncertainty due to the experimental error in F_π. The crucial aspect of this expression is that it has no free parameters that need to be determined phenomenologically. In addition, since the mass of the π^0 is the smallest in the hadron spectrum, higher order corrections to this prediction are small and can be calculated with a sub-percent accuracy.

The current experimental value is 7.84 ± 0.56 eV[3] and is in good agreement with the predicted value with the chiral limit amplitude. This number is an average of several experiments[3] which are discussed in Appendix I. The error of 7% quoted by the Particle Data Book is most likely too low since each of the quoted experiments appears to have understated their errors and also, as can be seen in figure 1, from the much larger dispersion between the different measurements. Even at the 7% level, the accuracy is not sufficient for a test of such a fundamental quantity, and in particular for the new calculations which take the finite quark masses into account. The level of precision of $\simeq 1.4\%$, which is the goal of *PrimEx*, will satisfy these requirements.

The decay amplitude given above is exact only in the chiral limit, *i.e.*, when the $u-$ and $d-$quark masses vanish. In this case, the anomaly is saturated by the π^o pole and the result for the decay amplitude given above is exact. However, the current-quark masses are non-vanishing and are approximately $m_u \simeq 4MeV$ and $m_d \simeq 7MeV$[4]. There are two sources of corrections due to this explicit breaking of chiral symmetry. The first and dominant one results from a combined effect that involves the corrections to the decay constants (because of isospin breaking there is a decay constant matrix in the subspace of the π^0, η and η') and an isospin breaking mixing that gives the physical π^0 a non-vanishing component along the pure U(3) states η and η'. In the absence of isospin breaking this source of chiral symmetry breaking boils down to merely replacing the value of F_π in the chiral limit by the measured value determined from π^+ decay[5, 6]. The second source of corrections is due to the fact that the saturation of the matrix elements of the divergence of the axial current also involves excited mesonic states when chiral symmetry is broken by quark masses. This effect is estimated using QCD sum rules[7] and turns out to be much smaller than the mixing effects.

Stimulated by the *PrimEx* project, several new theoretical calculations have been published in recent years, and are shown in figure 1. The first two independent calculations of the chiral corrections have been performed in the combined framework of chiral perturbation theory (ChPT) and the $1/N_c$ expansion up to $\mathcal{O}(p^6)$ and $\mathcal{O}(p^4 \times 1/N_c)$ in the decay amplitude[8][9]. The η' is explicitly included in the analysis as it plays as important a role as the η in the mixing effects. It was found that the decay width is enhanced by about 4% with respect to the value stated in equation (1). This enhancement is almost entirely due to the mixing effects. The result of this next-to-leading order analysis is $\Gamma_{\pi^0 \to \gamma\gamma} = 8.10$ eV with an estimated uncertainty of less than 1%. Another theoretical calculation based on QCD sum rules[10], also inspired by the *PrimEx* experiment, has recently been published with a theoretical uncertainty less than 1.5%. Here, the only input parameter to the calculation is the η width. The measurement of the decay width of the π^0 with a precision comparable to these calculations will provide an important test of the fundamental QCD predictions.

The proposed measurement at the $\simeq$1.4% accuracy level fills an important experimental gap, namely a precision verification of the predictions of the axial anomaly and the chiral corrections to the decay rate. The so-called "direct" method of determination of $\Gamma_{\pi^0 \to \gamma\gamma}$ lies below the prediction of the axial anomaly[11] and is therefore even more in disagreement with the new predictions which are based on both next-to-leading order chiral theory[8][9] and QCD sum rules[10]. This makes the *PrimEx* experiment even more compelling. It is indeed extremely important that effects of chiral symmetry breaking by the $u-$ and $d-$quark masses, which can be rather precisely predicted theoretically, can actually be experimentally tested thanks to the projected level of precision of *PrimEx*. This would indeed be one of the most precise tests of fundamental aspects of QCD ever achieved.

3 Neutral Pion Photoproduction via the Primakoff Effect

We plan to use quasi-monochromatic photons of energy 4.6-5.7 GeV from the Hall B photon tagging facility to measure the absolute cross section of small angle π^o photoproduction from the Coulomb field of complex nuclei. The invariant mass and angle of the pion will be reconstructed by detecting the π^o decay photons from the $\pi^o \to \gamma\gamma$ reaction.

For unpolarized photons, the Primakoff cross section is given by[12]:

$$\frac{d\sigma_P}{d\Omega} = \Gamma_{\gamma\gamma} \frac{8\alpha Z^2}{m^3} \frac{\beta^3 E^4}{Q^4} |F_{e.m.}(Q)|^2 sin^2\theta_\pi \tag{4}$$

where $\Gamma_{\gamma\gamma}$ is the pion decay width, Z is the atomic number, m, β, θ_π are the mass, velocity and production angle of the pion, E is the energy of incoming photon, Q is the momentum transfer to the nucleus, and $F_{e.m.}(Q)$ is the nuclear electromagnetic form factor, corrected for final state interactions of the outgoing pion.

As the Primakoff effect is not the only mechanism for pion photoproduction at high energies, some care must be taken to isolate it from competing processes. In particular, the full cross section is given by:

$$\frac{d\sigma}{d\Omega_\pi} = \frac{d\sigma_P}{d\Omega} + \frac{d\sigma_C}{d\Omega} + \frac{d\sigma_I}{d\Omega} + 2 \cdot \sqrt{\frac{d\sigma_P}{d\Omega} \cdot \frac{d\sigma_C}{d\Omega}} cos(\phi_1 + \phi_2) \tag{5}$$

where the Primakoff cross section, $\frac{d\sigma_P}{d\Omega}$, is given by equation (4). The nuclear coherent cross section is given by:

$$\frac{d\sigma_C}{d\Omega} = C \cdot A^2 |F_N(Q)|^2 sin^2\theta_\pi \tag{6}$$

and the incoherent cross section is:

$$\frac{d\sigma_I}{d\Omega} = \xi A(1 - G(Q)) \frac{d\sigma_H}{d\Omega} \tag{7}$$

where A is the nucleon number, $Csin^2\theta_\pi$ is the square of the isospin and spin independent part of the neutral meson photoproduction amplitude on a single nucleon, $|F_N(Q)|$ is the form factor for the nuclear matter distribution in the nucleus, (corrected for final state

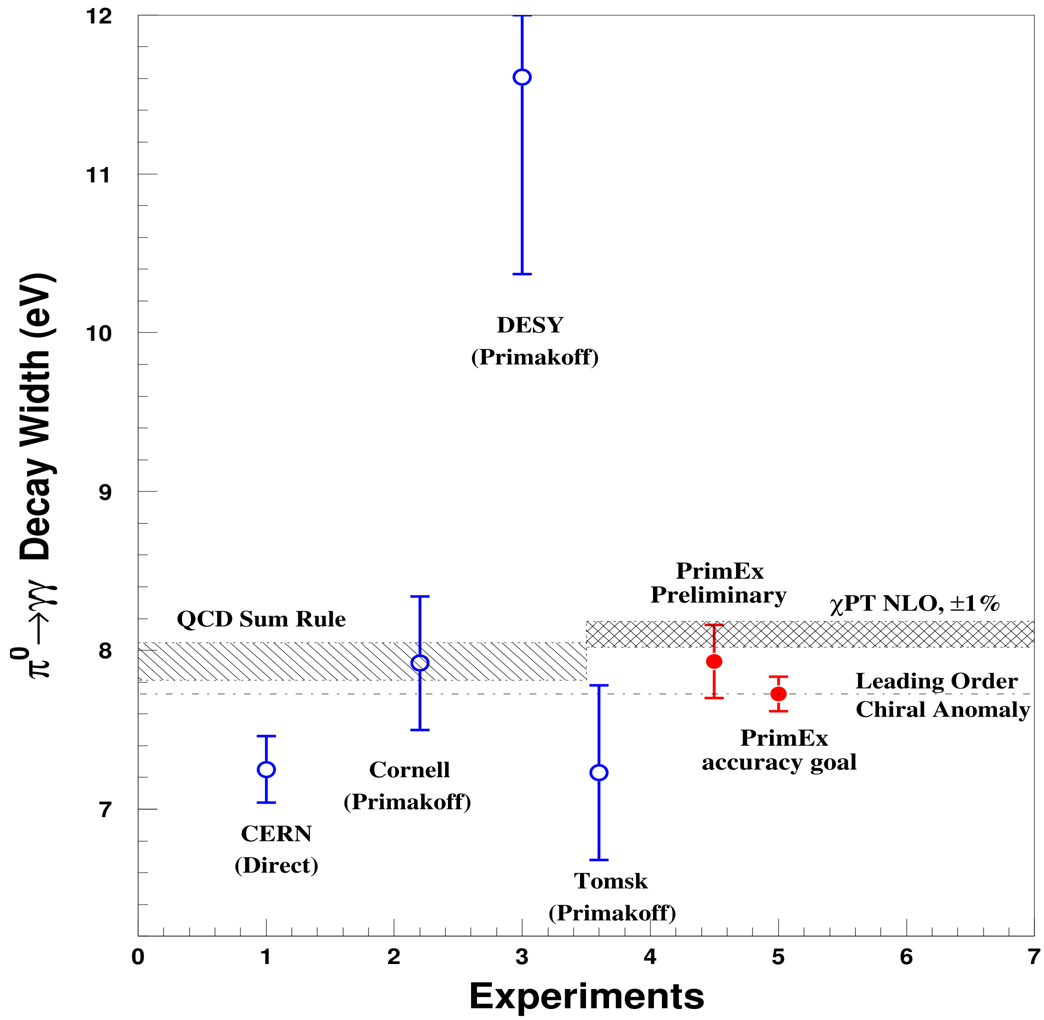

Figure 1: $\pi^o \rightarrow \gamma\gamma$ decay width in eV. The dashed horizontal line is the leading order prediction of the axial anomaly (equation 3)[1, 2].The left hand side shaded band is the recent QCD sum rule prediction and the right hand side shaded band is the next-to-leading order chiral theory predictions. The experimental results with errors are for : (1) the direct method[11]; (2, 3, 4) the Primakoff method [14, 12, 13]; (5) the preliminary result from the first *PrimEx* data set; (6) the expected error for the final goal of the *PrimEx* experiment, arbitrarily plotted to agree with the leading order prediction.

interactions of the outgoing pion), ξ is the absorption factor of the incoherently produced pions, $1-G(Q)$ is a factor which reduces the cross section at small momentum transfer due to the Pauli exclusion principle, and $\frac{d\sigma_H}{d\Omega}$ is the π^o photoproduction cross section on a single nucleon. The relative phase between the Primakoff and nuclear coherent amplitudes without final state interactions is given by ϕ_1, and the phase shift of the outgoing pion due to final state interactions is given by ϕ_2.

Kinematical considerations enable one to separate the Primakoff effect from other photo-pion production mechanisms. The Primakoff cross section is zero for pions emitted along the incident photon direction, has a sharp maximum at an angle $\theta_\pi \sim m_\pi^2/2E_\pi^2$, and falls rapidly to zero at larger angles. It is proportional to Z^2, and its peak value is roughly proportional to E^4. The nuclear coherent cross section for spin zero nuclei is also zero in the forward direction, but has a broad maximum outside the angular region of the Primakoff effect, and falls at larger angles as shown in figure 2, where the amplitudes are normalized to the Cornell data[14], and distortion effects are included. The angular dependence of the Primakoff signal is different from the background processes, allowing $\Gamma(\pi^0 \to \gamma\gamma)$ to be extracted from a fit to the angular distribution of photo-produced π^0. Measurements of the nuclear effects at larger angles are necessary to determine the unknown parameters in the production mechanism and thus make an empirical determination of the nuclear contribution in the Primakoff peak region. Consequently, this experiment requires a π^o detector with good angular resolution to eliminate nuclear coherent production, and good energy resolution in the decay photon detection will enable an invariant mass cut to suppress multi-photon backgrounds.

The production of neutral pions via the Primakoff effect is primarily an electromagnetic phenomenon and, therefore, can be accurately calculated. The main features of the Primakoff effect listed above will be used to test the accuracy of our data: (1) We will take data with sufficient angular resolution to check the shape of the Primakoff peak after the coherent nuclear and nuclear-Primakoff interference amplitudes, which will be determined empirically by larger angle data, have been subtracted; (2) two spin zero targets (^{12}C, ^{208}Pb) will be used. These have form factors which have been well studied by electron scattering experiments, and can be used to test the Z^2 dependence of the cross section; and (3) the E^4 dependence of the peak cross section will be measured in the energy range from 4.6 to 5.7 GeV. The study of the Primakoff peak as a function of these three variables should add a great deal of confidence to the measurement, and can be used to empirically determine the systematic errors.

We submitted our first proposal (E-99-014) to PAC15 in December of 1998. It was approved by PAC15 and reconfirmed in jeopardy review later by PAC22 with an "A" rating. The first experiment on two targets (^{12}C and ^{208}Pb) was performed in 2004. The preliminary results demonstrate that we are able to control the systematic errors with the designed precision, and more beam time is needed to reach the proposed goal of $\sim 1.4\%$ accuracy. In the following sections, we will describe what we have achieved in the first *PrimEx* experiment and what we can improve in a future run.

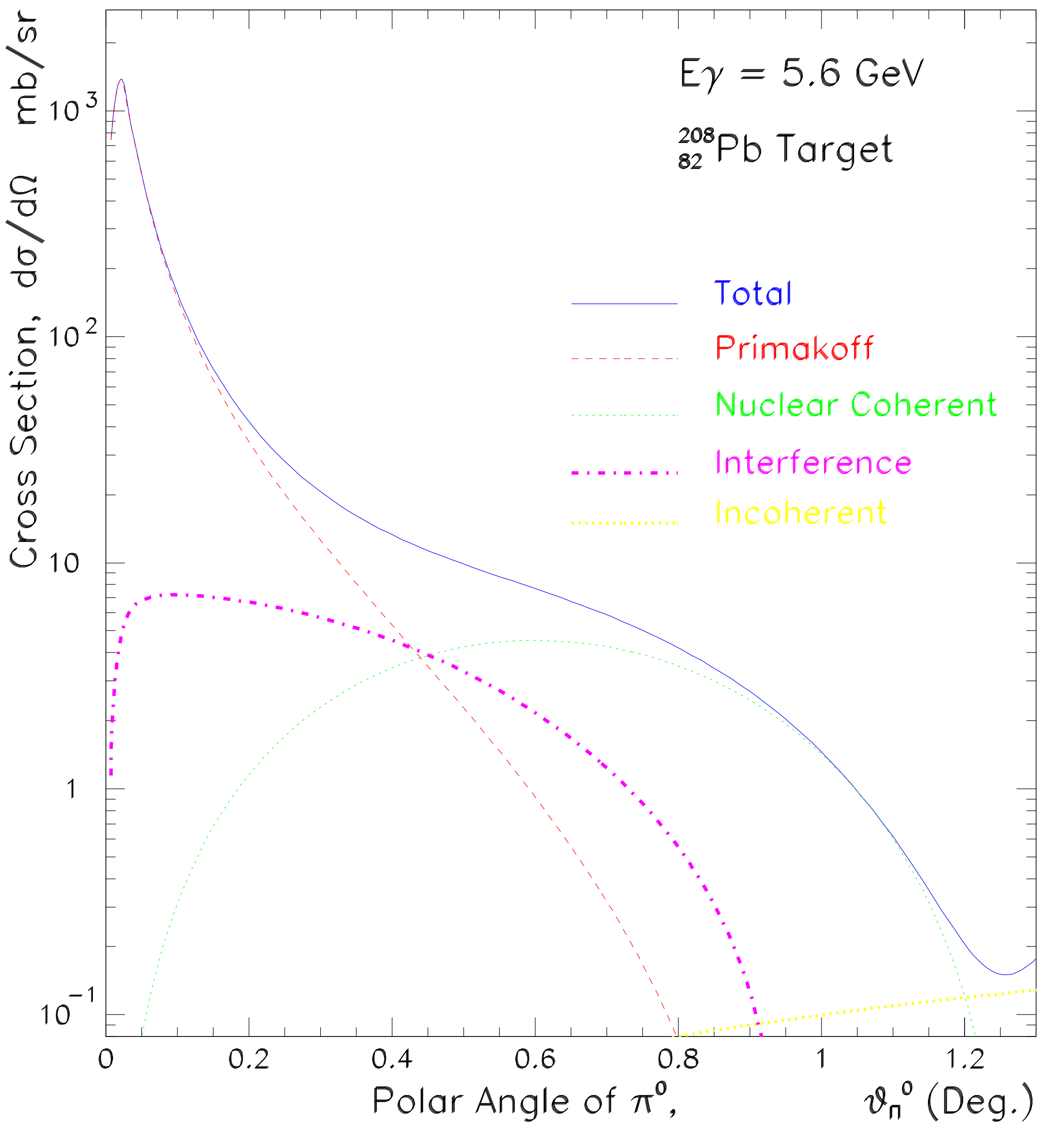

Figure 2: Angular behavior of the electromagnetic and nuclear π^o photoproduction cross sections for ^{208}Pb in the 6.0 GeV energy range.

4 Instrumentation and Experimental Techniques – Current Status and Planned Upgrades

With strong support from Jefferson Lab and a $1 million Major Research Instrumentation award (MRI, PHY-0079840) from the National Science Foundation, the *PrimEx* experimental setup was developed and constructed (See figure 3). The primary experimental equipment includes: (1) the existing Hall B photon tagger for the tagged photon beam; and new development of (2) 5% radiation length solid π^o production targets (^{12}C and ^{208}Pb); (3) a pair production luminosity monitor located just downstream of the π^o production target; (4) a 1m $\times$ 1m high resolution hybrid calorimeter (HYCAL) with a plastic scintillator charged particle veto for detecting π^0 decay photons; (5) a scintillator fiber based photon beam profile and position detector located behind HYCAL for on-line beam position monitoring. Here, we describe the performance of this equipment during the first *PrimEx* run in 2004, as well as our future plans .

4.1 Targets

We propose to use two targets in this experiment, ^{12}C and ^{208}Pb. The carbon target is approximately 380 mil thick (5% R.L.) and uses Highly Ordered/Oriented Pyrolitic Graphite (HOPG) as the target material. The lead target is a rolled metal target approximately 12 mils thick (5% R.L.) and uses 99% enriched ^{208}Pb as the target material. The uncertainties in the effective areal densities of the carbon and lead targets are 0.05% and 0.43%, respectively. Both targets were utilized in the first *PrimEx* run. The methodology for mapping the effective areal densities of the targets ($atoms/cm^2$) and the estimated errors are described in an Appendix to this proposal.

The motivation for using these targets are several. First, they are spin zero nuclei, thus simplifying the form of the Primakoff cross section by virtue of the absence of spin flip amplitudes. Second, as described in detail in Appendix III to this proposal, we have developed procedures for determining their thicknesses and ensuring their uniformity to a high level. Third, they span a range of atomic number, thus providing a test of the validity of the subtraction of various background neutral pion production processes. Fourth, our theorist collaborators in *PrimEx* have invested a considerable amount of effort in understanding and quantifying the background processes in these targets.

4.2 The neutral pion detector

4.2.1 Charged particle veto detector

The veto counter system consists of twelve scintillation paddles with dimensions $120 \times 10 \times 0.5cm^3$ which cover the front face of the HYCAL calorimeter. The purpose of the veto counters is to reject charged particle backgrounds incident on the calorimeter. They are designed to have good efficiency for charged particle detection, and be sufficiently thin so that the probability for photon conversion in the paddles is small. Light is collected from both ends of the paddles using XP2262B PMTs from Photonis and tube bases from Vorg Electronics. The time difference between flight times to the two PMTs is used find the

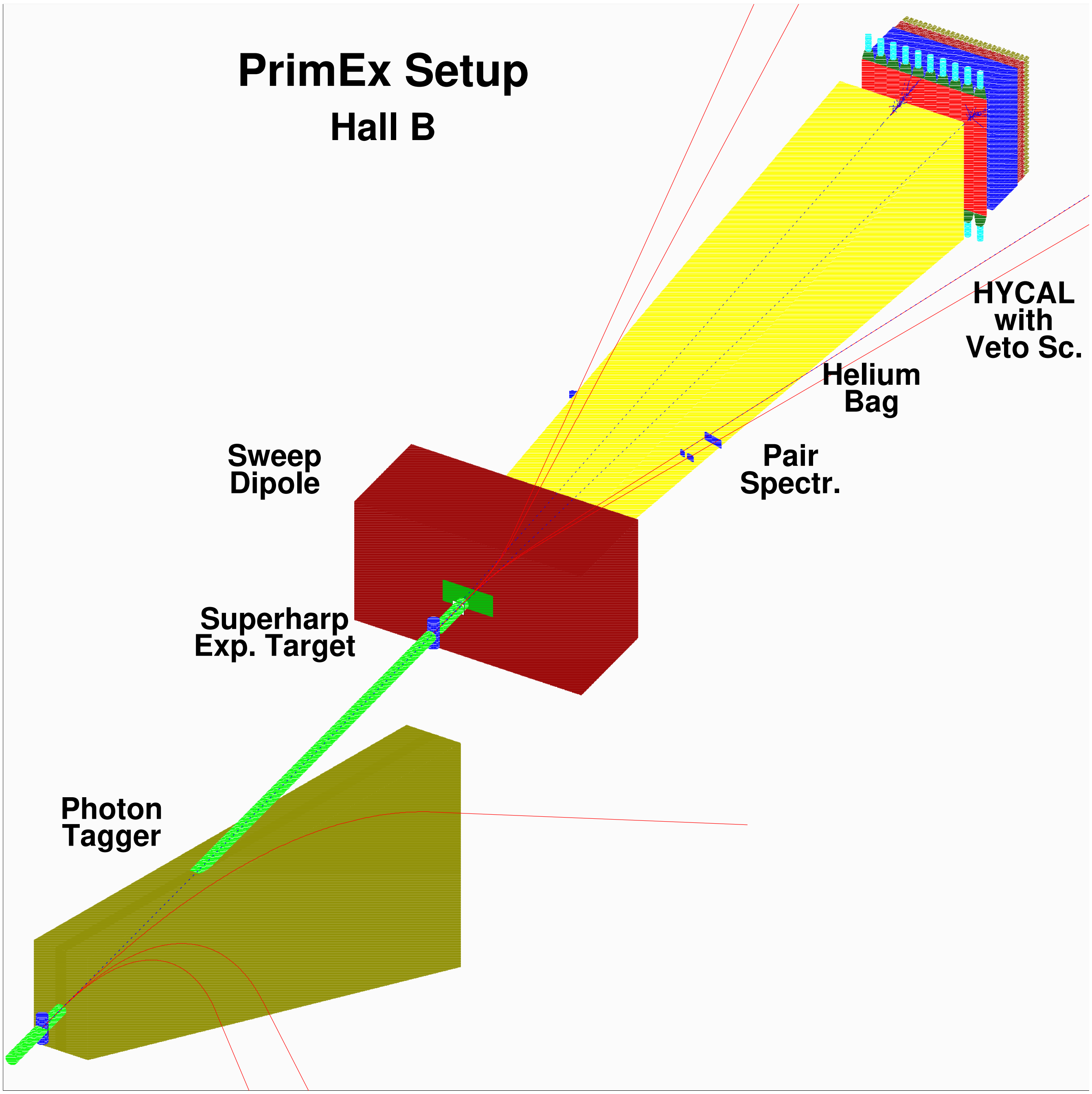

Figure 3: Layout of the *PrimEx* experimental setup.

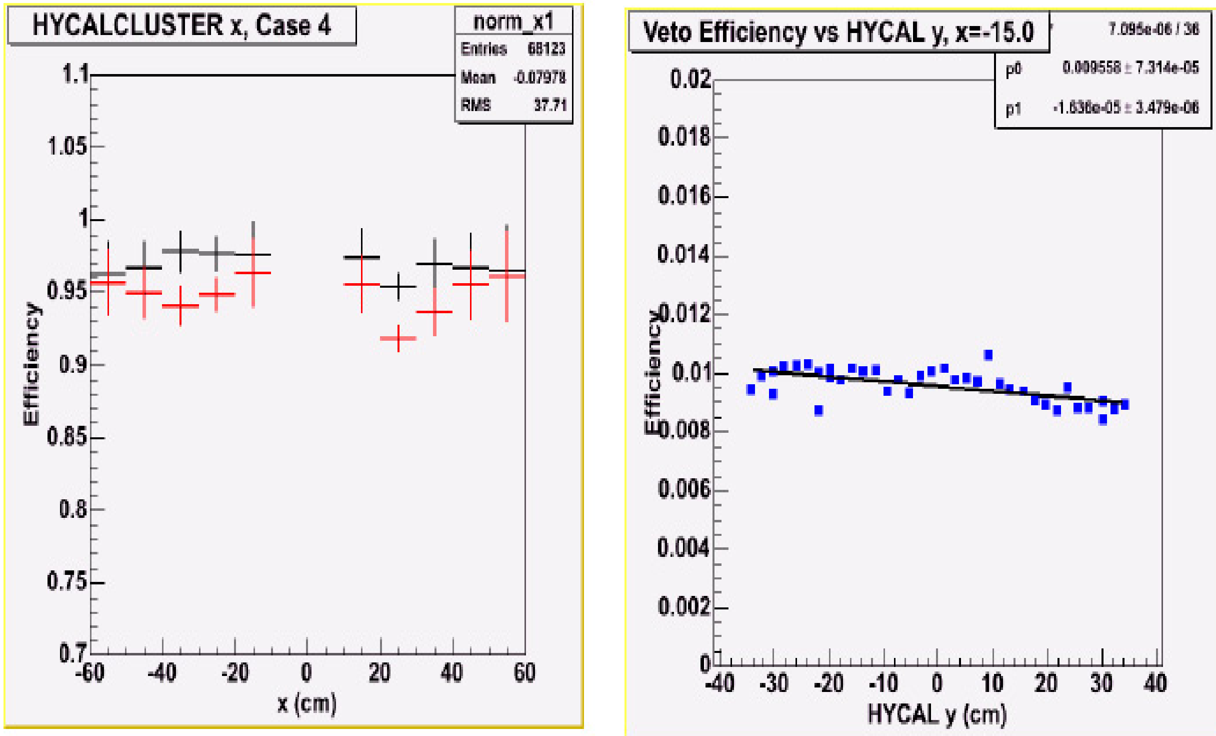

Figure 4: *Left:* Charged particle detection efficiency. The black points are from matching the veto counters with HYCAL by x position and timing. The red data have additional matching in y position. *Right:* Neutral particle misidentification probability for veto counter centered at $x = -15cm$ as a function of y. The black line is a linear fit.

longitudinal coordinate (y) of the hit. The counters were wrapped with an inner layer of Tyvek, and an outer layer of black Tedlar. During the first *PrimEx* run, the PMT gains were matched using special runs where e^+e^- pairs produced at the target were swept into the veto paddles by the pair spectrometer magnet, and we propose to take similar data during our next run. The time-walk effects due to varying signal sizes were observable, but were found to be small and had little effect on the y-position resolution. The veto y-positions, which were calculated from the time difference between the top and bottom PMTs, were calibrated against the hit positions given by HYCAL. The average resolution was determined to be $\pm 4.5cm$, which is within the tolerance of the experiment and corresponds to the width of the counters.

The pair production runs were also analyzed for the charged particle efficiency. The efficiencies were determined by dividing the number of particles detected by a veto counter by the number of particles detected in the region of HYCAL covered by the acceptance of the given veto. Figure 4 (left) shows that the charged-particle efficiency for the veto counters is approximately 95%. For the neutral misidentification analysis, data with low intensity photon beams incident on each veto counter were utilized. Figure 4 (right) shows the neutral misidentification probability for the counter at $x = -15cm$ *versus* the y-position given by HYCAL. The plot shows that the conversion probability is low ($\sim 1\%$) and constant over the length of the counter. The other eleven counters show similar results.

Figure 5 presents "hybrid" mass distributions taken during the 2004 run with the veto cut not applied, and then applied. The hybrid mass is closely related to the two-photon invariant mass distribution, and includes information on the elasticity of the event. In applying the veto cut, there was a requirement that the veto x-y coordinate should match the hit position in HYCAL, and also that there is a timing correlation between the veto counter and HYCAL. The plots are at π^o angles which range from the Primakoff peak to the nuclear coherent region. The figure shows there is a very significant reduction in the background under the π^o mass peak when the veto cut is applied at low angles.

In our π^o analysis effort to date, we have used a global average derived from the π^o analysis to account for photon conversion in the veto counters. We have investigated two methods for obtaining a global average from the data. The first involves integrating the hybrid mass distributions, examples of which are shown in figure 5, without and with the veto cut applied. The percent deviation with the veto cut applied is plotted as a function of angle in the top-left plot of figure 6. Note that figure 5 indicates the veto has a progressively weaker effect on the hybrid mass distributions, and this is borne out in the top-left plot of figure 6, where the veto "effect" asymptotically approaches 3.20% at large angles. The second approach to fixing the average effect of photon conversion involves finding the number of events in the hybrid mass peaks without and with the veto cut applied. The percentage difference as a function of angle is plotted on the top-right plot of figure 6, and those data points are summed into a histogram on the bottom-right plot of figure 6. From this distribution, the average veto conversion effect on the π^o analysis is estimated at 3.23%, which is in good agreement with method #1.

4.2.2 The hybrid electromagnetic calorimeter *HYCAL*

At the incident photon energies of this experiment ($E_\gamma = 4.6 - 5.7$ GeV), the Primakoff cross section peaks at extremely small angles ($\theta_{peak} \simeq 0.02°$). Therefore, in order to identify and extract the Primakoff amplitude, the experimental setup must have sufficient angular resolution for detecting forward produced pions. The pions are identified by detecting the decay photons ($\pi^0 \to \gamma\gamma$) in the multi-channel electromagnetic calorimeter. Good invariant mass resolution in the $\gamma\gamma$ system is also required for the selection of pions from the experimental background. These kinematical variables have strong dependence on both the position and energy measurement accuracies of the calorimeter. In addition, the kinematical constraints imposed by the knowledge of the initial photon energy provided by the tagging system results in a significant improvement of the angular resolution and invariant mass. The combination of the photon tagging facility and high resolution calorimetry is one of the important advantages of our experiment over the previous Primakoff type of experiments. It provides significantly improved invariant mass resolution, which is important for the clean identification of photoproduced pions and high resolution in production angle to extract the Primakoff amplitude from the competing background nuclear processes. A precision experiment also requires a large geometrical coverage for the decay photons. At these energies, in order to detect 70% of the events the calorimeter must have over 1×1 m^2 cross-sectional size at a distance of about seven meters from the production target. To optimize cost and

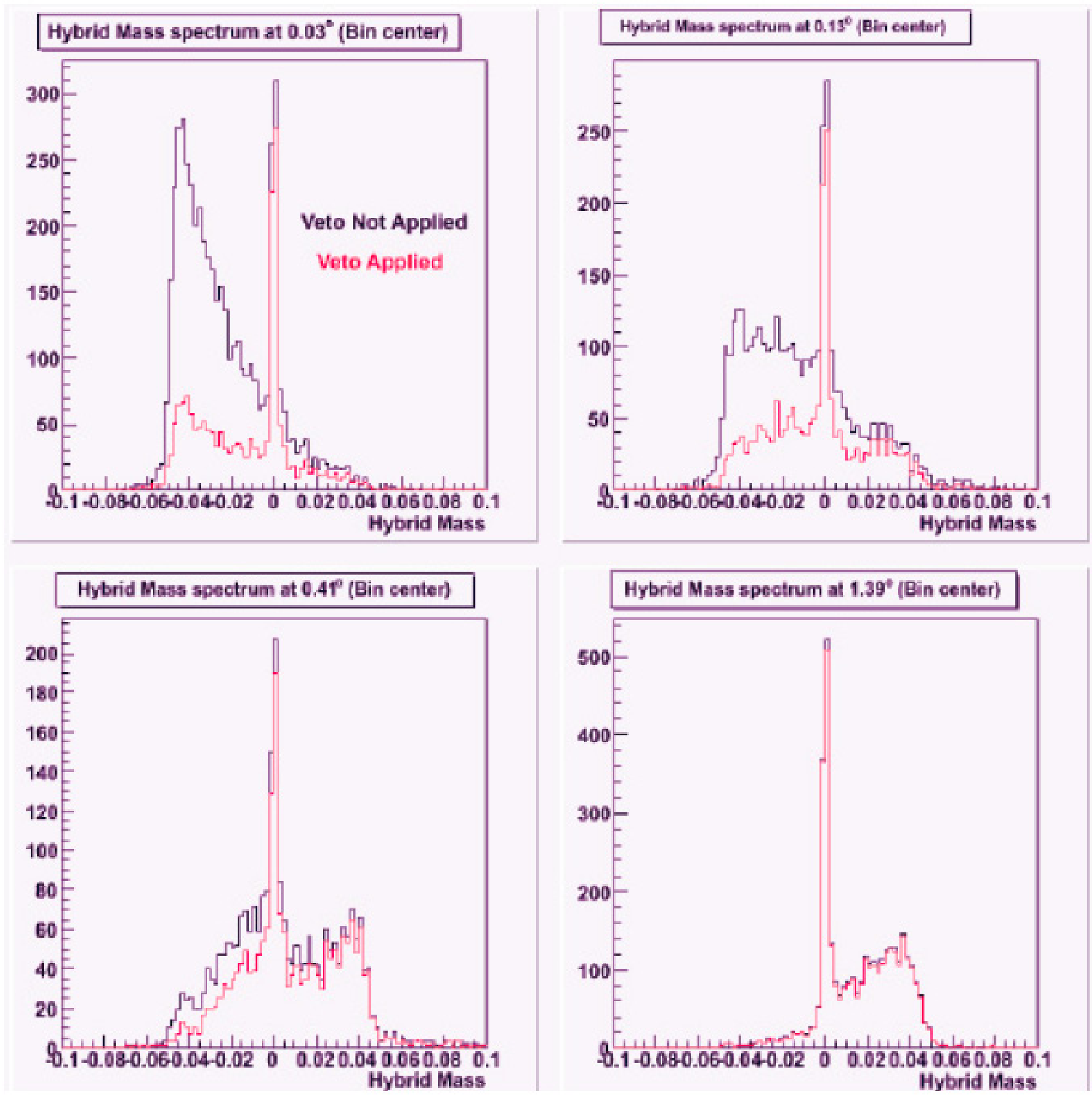

Figure 5: Hybrid mass spectra at angles of 0.03, 0.13, 0.41, and 1.39 degrees without a veto cut (black), and with a veto cut (red).

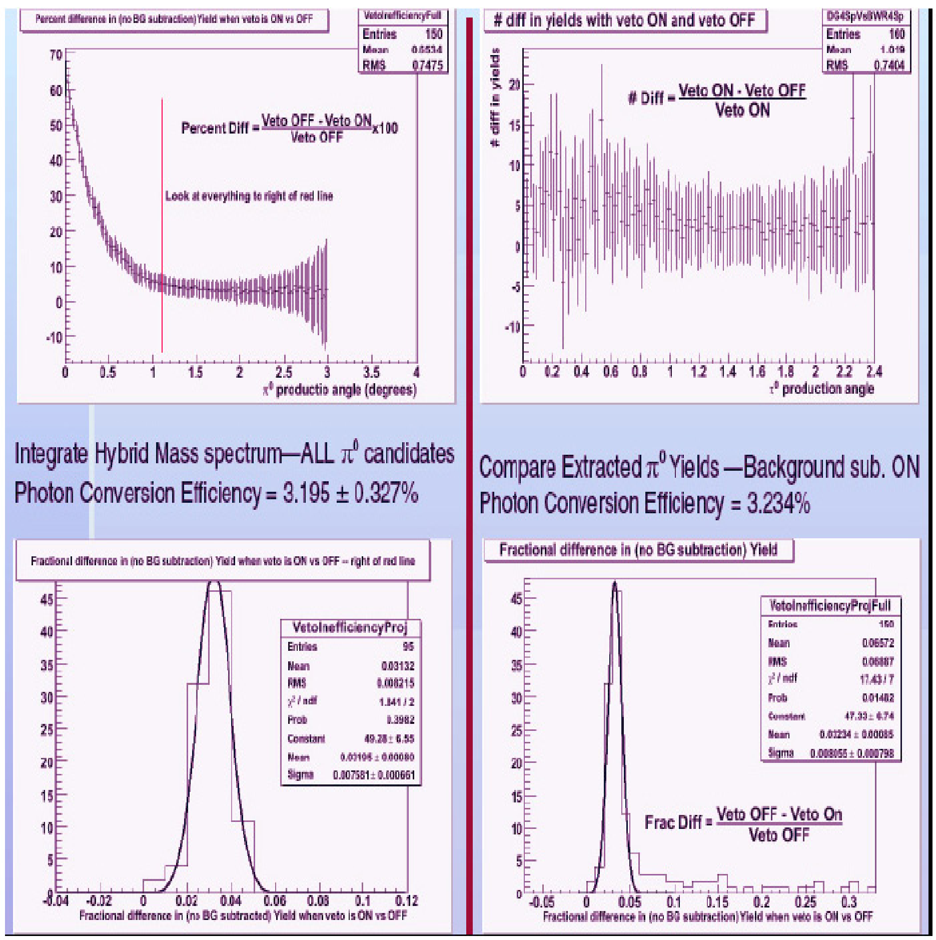

Figure 6: Measuring the veto counter photon conversion efficiency for π^o events.

performance, we have made a decision to construct a hybrid type of calorimeter combining traditional lead glass shower detectors and newly developed high resolution $PbWO_4$ crystal scintillators. The lead glass part of the calorimeter was made of TF-1 GAMS-type Cherenkov detectors ($3.82 \times 3.82 \times 45.0$ cm^3 in size) and was provided by our collaborators from IHEP, Protvino Russia. Each lead glass module was wrapped in aluminized Mylar and viewed with FEU-84 PMT's. These detectors have been used in many other experiments and their characteristics are well understood. They provide stable performance with moderate resolution in both position and energy. For the high resolution crystal part of the calorimeter we have done extensive R&D work to select the crystal type, the manufacturer and the detector structure. In the past few decades, $PbWO_4$ has became a popular inorganic scintillator material for precision and compact electromagnetic calorimetry in high and medium energy physics experiments. The performance characteristics of the $PbWO_4$ crystals before our beam tests had been well known mostly for high energies (>10 GeV)[17] and at energies below one GeV[18]. In order to check the performance of the crystals in the few GeV region and to select the manufacturer, we carried out beam tests with a 6×6 prototype detector consisting of crystals from two different manufacturers: Bogoroditsk (BTCP), Russia and Shanghai (SIC), China. The upper 3×6 section of the detector was assembled from crystals made in Russia, and the bottom section consists of Chinese crystals from SIC. The scintillation light from the electromagnetic shower was detected with Hamamatsu R4125HA photomultiplier tubes coupled to the back of the crystals with optical grease. The prototype detector was moved by remote control in two dimensions perpendicular to the secondary electrons, which were selected by the *PrimEx*/Hall B dipole magnet and the scintillating telescopes. An x and y coordinate scintillation fiber detector (2 mm in fiber size) was used in front of the detector to define the impact points of the electrons. The performance of the crystal prototype was studied with secondary electrons with energies from $E_e = 2$ to 4 GeV. Results on energy and position resolution, and the dependence of crystal detector response on radiation rate were presented at the Calor-2002 International Conference[20]. We have procured 1250 crystal modules from SIC based on the high performance they exhibited in these tests as well as the comparatively lower price per crystal, which was achieved through our collaborators in China (Chinese Institute of Atomic Energy, CIAE). This has enabled us to increase the number of crystals in the calorimeter by more than a factor of two over that envisioned in the original proposal and funded by the NSF MRI award. The increased size of the crystal detectors significantly enhanced the high resolution part of the calorimeter and played a critical role for the π^0 decay width extraction in the current experiment. Each crystal which arrived at JLab from the manufacturer was first tested for mechanical properties (visual inspection and dimensions at four points). A typical distribution of measured sizes at the front of the crystals from one shipment is shown in Figure 7. For those crystals that satisfied the mechanical specifications, the optical transmission *versus* wavelength was measured using the JLab Detector Group's spectrophotometer. Typical transmission spectra are shown in Figure 8 and Figure 9.

Two important criteria have been set for the lead tungstate detector module development - to optimize the light collection from the back side of the crystal and to minimize the mechanical structure in the transverse dimensions. A complete module of the $PbWO_4$ crystal detector is shown in Figure 10. The scintillation light from the electromagnetic shower in the crystals was detected with Hamamatsu R4125HA photomultiplier tubes (PMT) coupled

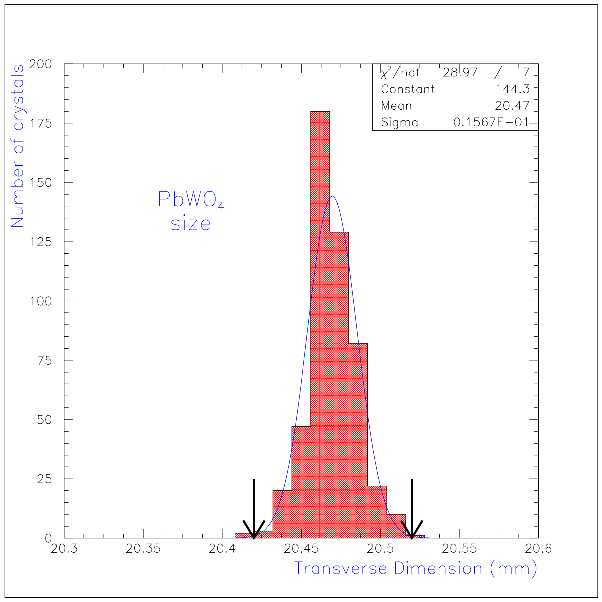

Figure 7: Distribution of front size of crystals from one shipment. Tolerance in size is shown by arrows.

to the back with optical grease. Each crystal was first wrapped in ~63μm VM-2000 reflector (from 3M), then with a 38.1 μm black Tedlar for optical isolation between the blocks. The PMT housings were attached to the crystals with two specially designed brass flanges on the front and back of the crystals, stretched with two 25 μm brass strips.

One of the challenging problems of the hybrid type calorimeters is the potential deterioration of the energy and position resolutions at the boundary region between the two types of radiators (for HYCAL, $PbWO_4$ crystals and lead-glass detectors). The difference in electromagnetic shower development both in longitudinal and lateral directions in $PbWO_4$ and lead glass also requires optimization of the position of the crystal radiators along the lead glass blocks. The first experimental results for the calorimeter characteristics *versus* the crystal z-position for 10-70 GeV electrons have been presented in [21]. Since the longitudinal development of the shower is energy dependent, the optimization of the z-position is energy dependent as well. We have performed extensive Monte Carlo simulations to define the optimum z-position of the $PbWO_4$ radiators along the lead glass blocks for the HYCAL calorimeter. These simulations, which are cross-checked with the experimental data from reference[21], showed that for the few GeV energy region the optimum for the z-position is within the 7-10 cm interval. In order to investigate the performance of the calorimeter at the transition region between the $PbWO_4$ crystals and lead glass detectors, and also to check the calorimeter's engineering concepts in real conditions, a prototype hybrid calorimeter (HYCAL-0) was constructed and tested in 2002 using the intense tagged photon beam. It consisted of 96 lead glass and 77 lead tungstate shower detectors and was assembled in

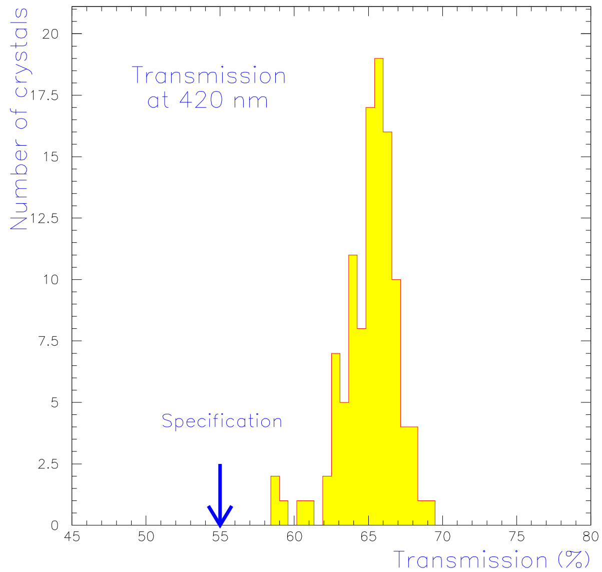

Figure 8: Optical transmission of crystals at 420 nm.

a light-tight iron frame maintained at a stable temperature of T = 11°C. After the two stages of prototyping and successive beam tests, the *PrimEx* collaboration constructed and assembled 1152 $PbWO_4$ crystal shower detectors and 576 lead glass Cherenkov counters as described above (116 × 116 cm^2 area). All individual detector modules were stacked in a specially designed light-tight iron frame, as shown in Figure 11. The light yield of the crystal is highly temperature dependent (∼ 2%/°C). In order to keep the detector array at a stable temperature, the detector assembly was surrounded by thick copper plates with circulating coolants. Temperature stability at the level of $\Delta T = \pm 0.1$°C was achieved during the entire period of data collection. To optimize the shower leakage in the transition region the lead tungstate detector assembly, which is in the central part of the calorimeter, is shifted downstream of the lead glass modules by 10 cm. Four crystal detectors are removed from the central part of the calorimeter (4.1×4.1 cm^2 hole in size) for the passage of the incident photon beam through the calorimeter.

The calorimeter is furnished with rear end readout electronics, with signal cables (two from each channel, for anode and dynode signals), high voltage cables and fiber optics cables to the front part of the calorimeter for the gain monitoring system. After 300 ns delay, the anode signals were digitized by means of a 14-bit charge-sensitive ADC (LeCroy 1881M, integration width=240 ns). The positive dynode signals ware summed group by group to form a total sum from the entire calorimeter for the trigger organization as described in the next sections.

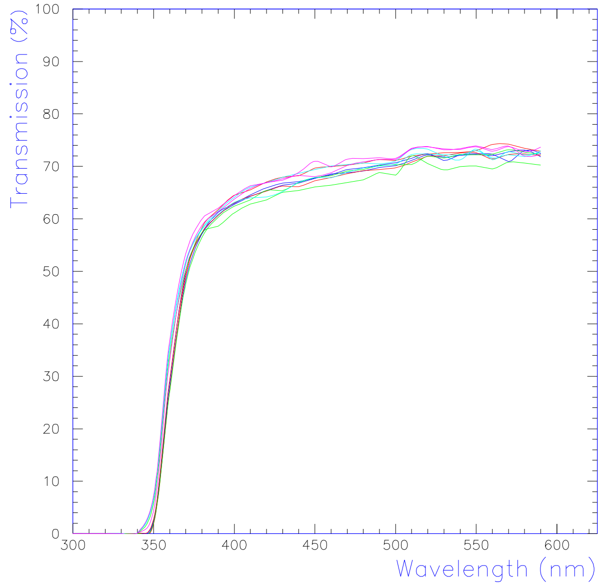

Figure 9: Typical optical transmission of crystals *versus* wavelength.

4.3 The Calorimeter Frame and Transporter

The individual modules of the HYCAL are assembled in a rectangular box inside of the calorimeter frame. The entire assembly weighs over five tons, and is movable in both horizontal and vertical directions in order to place each module in the beam for energy calibration. The transporter, shown in figure 12, has been designed and constructed to provide movement of the entire assembly of the support frame with detectors and thermo-stabilization system, delay cables and gain monitoring system mounted on the bottom of the HYCAL frame and the veto counters on the front of the HYCAL.

The calorimeter is remotely movable so that during the calibration and checkout of each module it can be positioned in the beam of tagged photons with an accuracy of $\pm 2mm$. A schematic drawing of this system is shown in figure 13. After the calibration and channel by channel checkout procedure, the calorimeter was moved to a specially designed support stand for the experiment. A drawing of the calorimeter in the data taking position is shown in figure 14. In this configuration, the accuracy of positioning the detector transverse to the beam is $\pm 0.7mm$. In addition, this system also provides the capability to move the detector along the beam line for different z-positions from the physics target.

When the calorimeter is not being used in the beam, the transporter system provides positioning of the entire calorimeter a few meters above the beam center, on Level 2 of

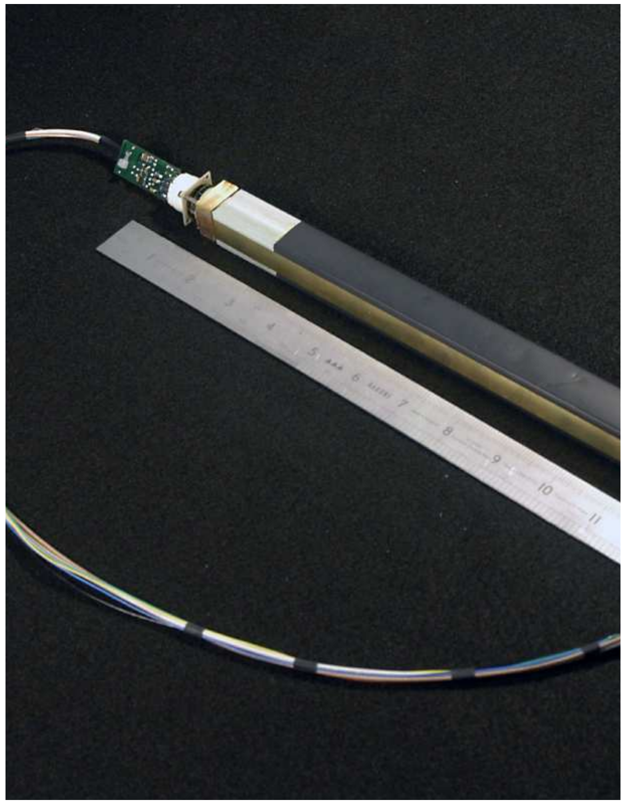

Figure 10: A single $PbWO_4$ crystal shower detector module.

the Hall B beam line. In addition to storage, this configuration allows the HYCAL to be available for re-assembly, maintenance, and testing with cosmic rays.

4.4 Performance of the Calorimeter

As mentioned above, the calibration of the HYCAL was performed with a low intensity tagged photon beam of selected energies ($E_\gamma = 0.5 - 5.5$ GeV), irradiating the centers of each detector module while the calorimeter was in the transporter configuration. Then, a tagged photon beam was scanned across the boundary with 2 mm step size to get data for the position and energy resolutions for the both type of detectors, as well as for the transition region between them.

The reconstructed energy distribution for the 4.3 GeV electrons is shown in figure 15 for three different calibrated ADC sums: the central module; the inner section comprising 3×3 crystals and the array of 6×6 crystals. The energy resolution is obtained using a Gaussian fit of the 6×6 distribution. As can be seen from the figure, an excellent energy resolution of $\sigma_E/E = 1.3\%$ has been achieved for 4.3 GeV. The measured energy resolution *versus* initial photon energy is shown in figure 16. The resolution of the lead glass part of detector is shown in figure 17.

Using the data from the transition region, the energy resolution of the shower cluster was extracted as a function of position. Dependence of the energy resolution *versus* photon impact position is shown in Figure 18. Degradation in resolution as the photon beam passes

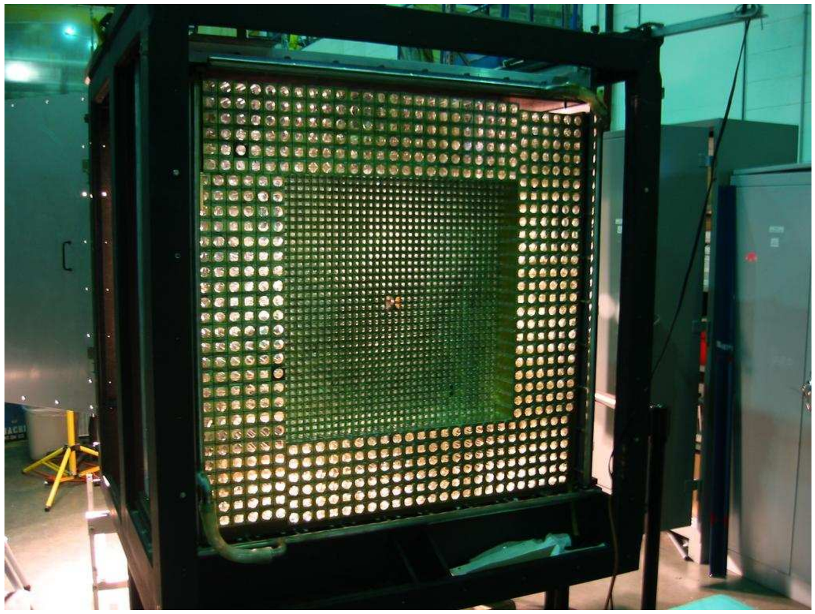

Figure 11: Front view of the HYCAL Calorimeter with all modules in place and before installation of fiber optic cables on front of each channel for the gain monitoring system.

from the last lead tungstate module to the lead glass region is evident and well described by the Monte Carlo simulation. Figure 18 (bottom) shows the relative reconstructed total energy for the same transition region. The $\sim 3\%$ dip at the interface predominantly arises from shower leakage from the uncovered backs and sides of the lead glass blocks.

The impact coordinates of the electromagnetic particles incident on the segmented hodoscopic calorimeters are determined from the energy deposition of the electromagnetic shower in several neighboring counters. In the case of the $PbWO_4$ crystals, the transverse size of the shower is about two times smaller than that in lead glass. As a result, the position resolution in the $PbWO_4$ detector with an optimal cell size should be about twice smaller than that of lead glass detectors. To maximize the position resolution, we have optimized the crystals' transverse dimensions, and have selected them to be 2.05×2.05 cm^2. This size is comparable to the Molière radius (2.2 cm) of the crystal material.

The distribution of the reconstructed coordinates for 4.3 GeV electrons hitting a crystal cell boundary is shown in Figure 19. The linear dependence of the reconstructed coordinates obtained from a logarithmically weighted average of the cell signals *versus* the impact positions is shown in Figure 20. As is well known, there is a rather strong correlation between the position resolution (σ_x) and the point at which the incoming electrons or photons hit the detector face. The bottom plot of the figure shows this dependence for the $PbWO_4$ crystals. The σ_x is smaller (1.28 mm) near the edge of the cell and increases to 2.1 mm at the cell center.

Similar to the energy reconstruction, one can expect degradation in the position resolution in the transition region as the photon beam passes from the last lead tungstate crystal module to the lead glass region. This dependence is shown in Figure 21. Though the simple center-of-gravity reconstruction exhibits typical oscillation of reconstructed *versus* impact

Figure 12: The HYCAL transporter in Hall B.

position with a relatively larger amplitude, the corrected logarithmic method shows a good linear transition from lead tungstate to lead glass regions.

Good position and energy resolutions achieved for the HYCAL calorimeter provided critical improvements in both two gamma invariant mass and production angle reconstructions. As an example, in Figure 22 is shown the two gamma invariant mass distribution extracted from the experimental data set for one angular bin only. An excellent resolution of $\sigma_{\gamma\gamma}$ =2.3 MeV provided precision extraction of events over the experimental background.

4.5 HYCAL Gain Monitoring System

To control the stability of gains for each channel of the calorimeter during the long data taking periods, a gain monitoring system was developed and constructed. This system is based on feeding light pulses from a central LED based light source distributed by fiber optics cables to the front part of each module. The main components of the Light Monitoring System (LMS) are: (1) a light source, (2) a mixing box, (3) a light distribution system, (4) filter wheel, (5) reference detectors and (5) a dedicated data acquisition system. The optical components and the reference detectors, as shown in Figure 23, are mounted in a thermally insulated box whose temperature is controlled at a level of 0.1°C.

Long term stability tests of the prototype LMS system, as well as several beam tests, have been performed. For this tests, the light intensity was monitored with a PIN photodiode and

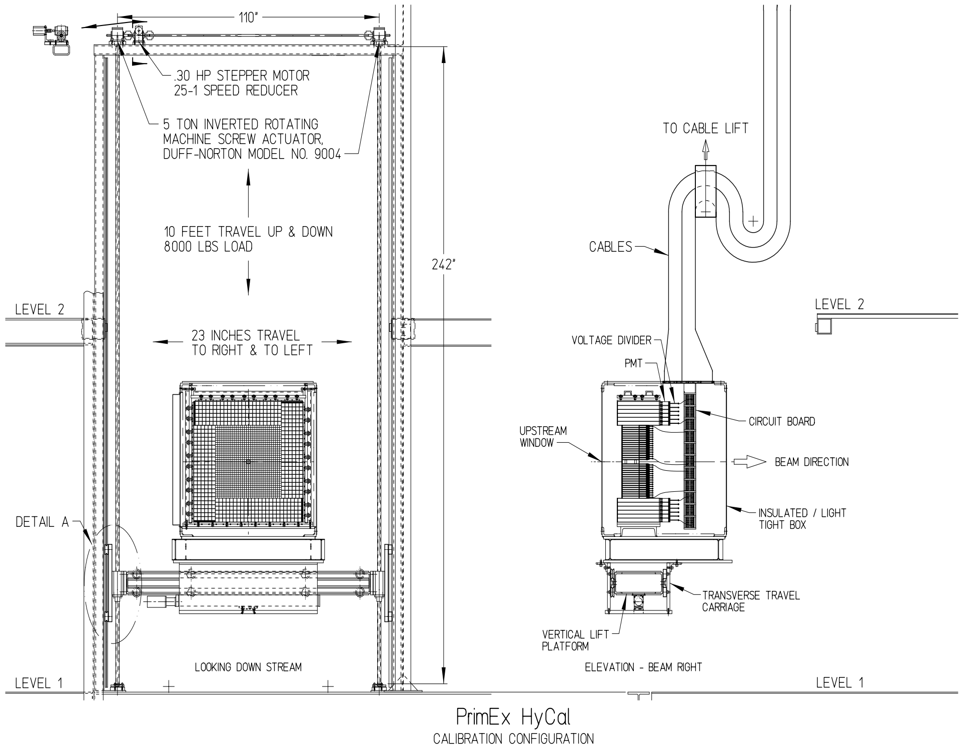

Figure 13: The HYCAL mounted on its transporter.

three reference PMTs. In figure 24, top picture, the distribution of the ratio, PMT_1/PMT_3, for the period of 540 hours is shown. The same ratio plotted *versus* time is presented in the bottom picture.

During the data taking period it was observed that the LMS reference detectors are somewhat sensitive to the change of magnetic field from the pair spectrometer dipole. This change of signals was observed at the level of 1.5% on the reference PMT signals [20]. We plan to fix this problem by adding more magnetic insulation and/or trying to replace the PMTs on the reference detectors with less sensitive photodetectors.

4.6 Luminosity monitoring

The primary advantages of the *PrimEx* experiment over the previous Primakoff experiments arise from the use of the Jefferson Lab Hall-B photon tagging facility to carefully control systematic errors and reduce backgrounds. First, the tagging technique allows for a significantly more accurate knowledge of the photon flux. Second, due to the energy dependence of the Primakoff cross section, it is critical to have a good knowledge of the absolute photon beam energy.

In order to determine the energy of the decaying π^0, each event is recorded in coincidence with a signal from the tagger. The experimental cross section for neutral pion photo-production is given by:

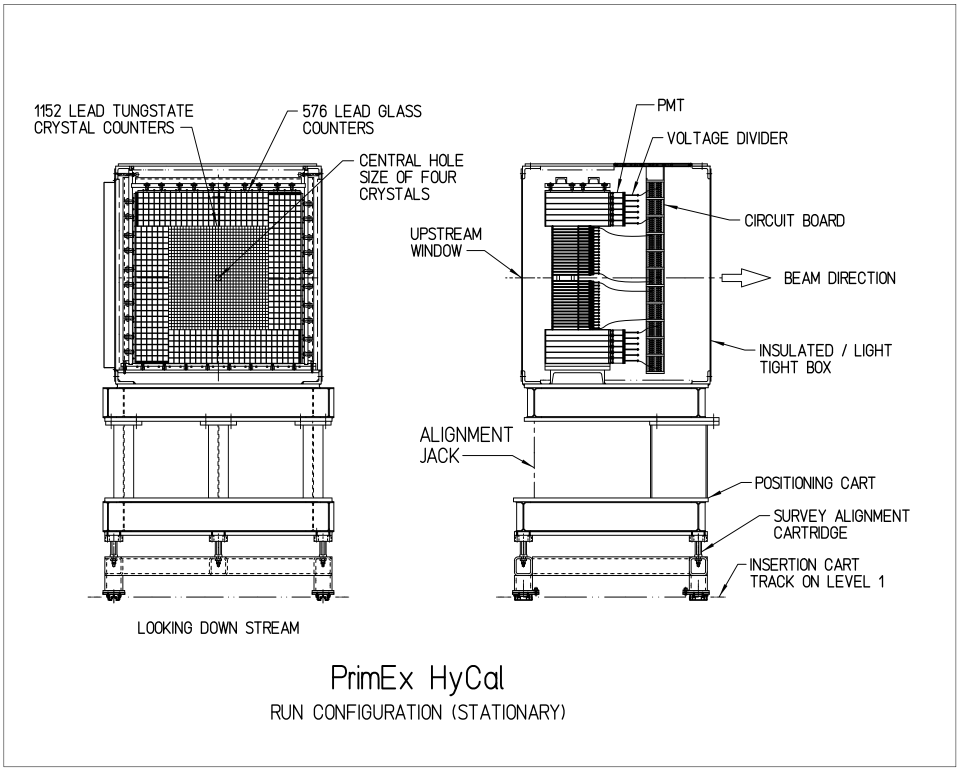

Figure 14: The HYCAL detector on its support stand in the run configuration.

$$\frac{d\sigma}{d\Omega} = \frac{dY_{\pi^0}^{tagged}}{N_\gamma^{tagged} \cdot \epsilon \cdot t \cdot d\Omega} \tag{8}$$

where $d\Omega$ is the element of solid angle of the pion detector, $dY_{\pi^0}^{tagged}$ is the yield of tagged π^o's within solid angle $d\Omega$, t is the target thickness, ϵ is a factor accounting for geometrical acceptance and energy dependent detection efficiency and N_γ^{tagged} is the number of *tagged* photons on the target.

The number of tagged photons per post bremsstrahlung electron can be measured in a calibration run by removing the physics target and placing a lead-glass total absorption counter (TAC) directly in the photon beam. Assuming that the total absorption counter is 100% efficient in detecting photons in the energy range relevant for the experiment, the ratio of Tagger·TAC coincidences to the number of tagger hits, the so called absolute tagging ratio, is then recorded:

$$R_{absolute} = \frac{N_{\gamma \cdot e}^{TAC}}{N_e}|_{calibration} \tag{9}$$

where $N_{\gamma \cdot e}^{TAC}$ is the number of photons registered by the TAC in coincidence with a tagging signal and N_e is the number of electrons registered in tagging counters.

Knowing this ratio, one can determine the tagged photon flux in the data taking run by counting the number of post bremsstrahlung electrons in the tagging counters:

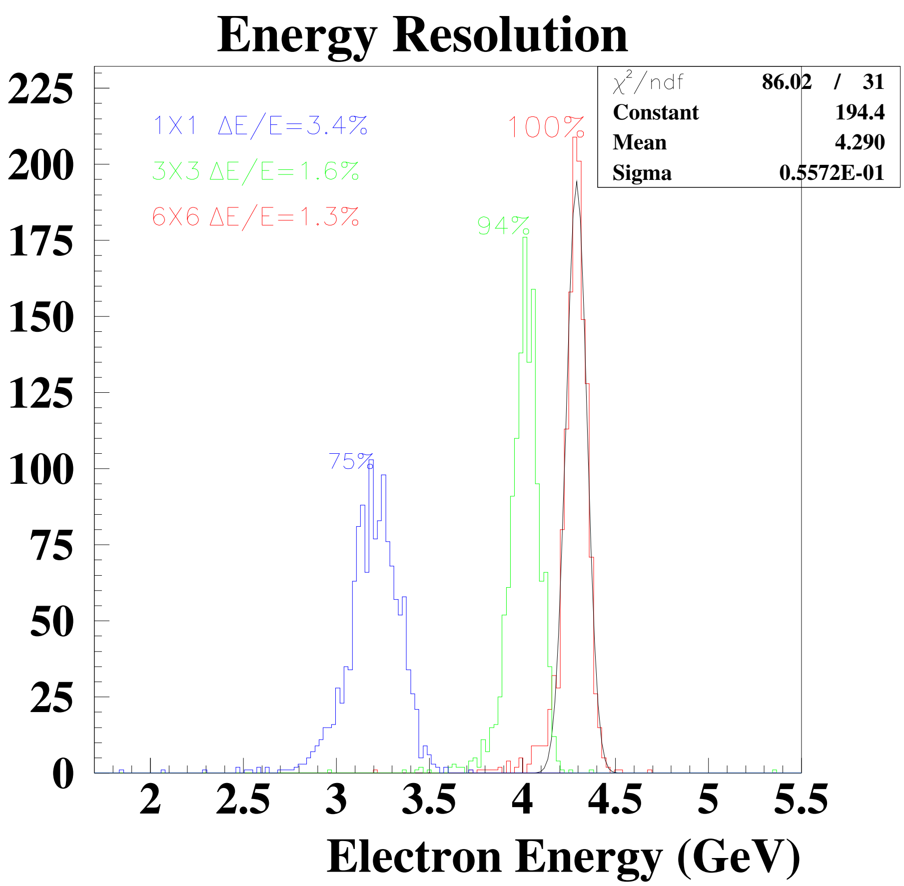

Figure 15: Energy response of a $PbWO_4$ crystal array to 4.3 GeV electrons. Left peak: single crystal; center peak: 3×3 array; right peak: 6×6 array.

$$N_{\gamma}^{tagged}|_{experiment} = N_e|_{experiment} \times R_{absolute} \tag{10}$$

The use of the total absorption counter to calibrate the number of tagged photons per electron in the tagger provides an absolute normalization of the photon flux incident on the π^0 production target. However, these measurements can be performed only at intervals between the data taking. Also in the calibration run, the rate of the total absorption counter is limited, and therefore, the tagging ratio can only be measured at a rate which is reduced by a factor of about one thousand as compared to the data taking run. A pair production luminosity monitor was constructed which is able to measure the relative tagged photon flux over a range of all relevant intensities, and operate continuously throughout the data taking runs. The pair spectrometer uses the physics target as a converter to measure the ratio of the number of $\gamma + A \rightarrow A + e^+ + e^-$ reactions in coincidence with a tagging signal to the number of hits in the tagging counters:

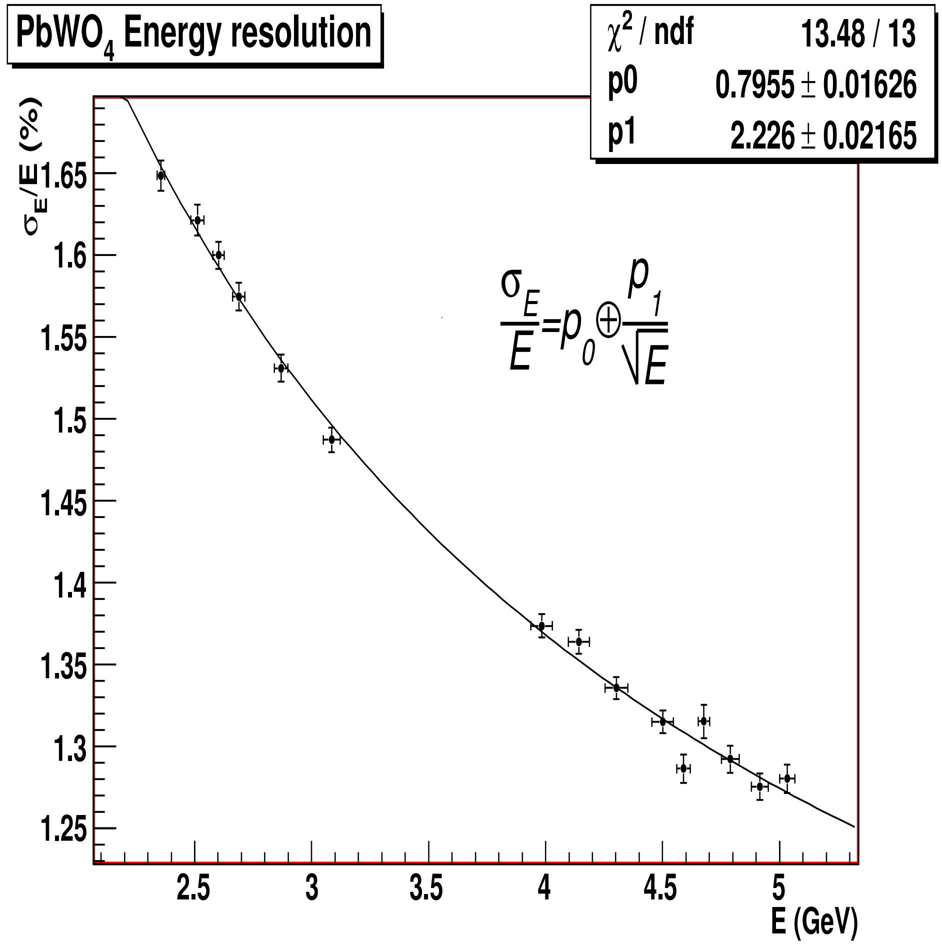

Figure 16: Measured energy resolution *versus* photon beam energy for the $PbWO_4$ part of the calorimeter.

$$R_{relative} = \frac{N^{PS}_{e^+e^- \cdot e}}{N_e}. \tag{11}$$

While this is a relative number, its absolute normalization can be fixed with the TAC. The advantages of the pair spectrometer are that it can operate over the entire range of intensities (of both the flux calibration and data taking runs) and has a smooth, relatively flat acceptance in E_γ covering the entire tagging range. In addition, it provides a nondestructive means of monitoring relative luminosity.

A major contribution to the error bar in the *PrimEx* measurement comes from the knowledge of the photon flux. To achieve the desired precision in the measurement of the π^0 decay width, it is necessary to know the photon flux to 1% or better. It should be noted that such a high precision measurement of the photon flux had not been previously attempted at Jefferson Lab Hall-B. The constant on line monitoring of the relative photon flux is crucial for such a high precision tagged photon flux measurement. As indicated by equation 10, the problem of cross section normalization is reduced to the determination of the number of electrons in the tagging counters and measuring the absolute tagging ratio.

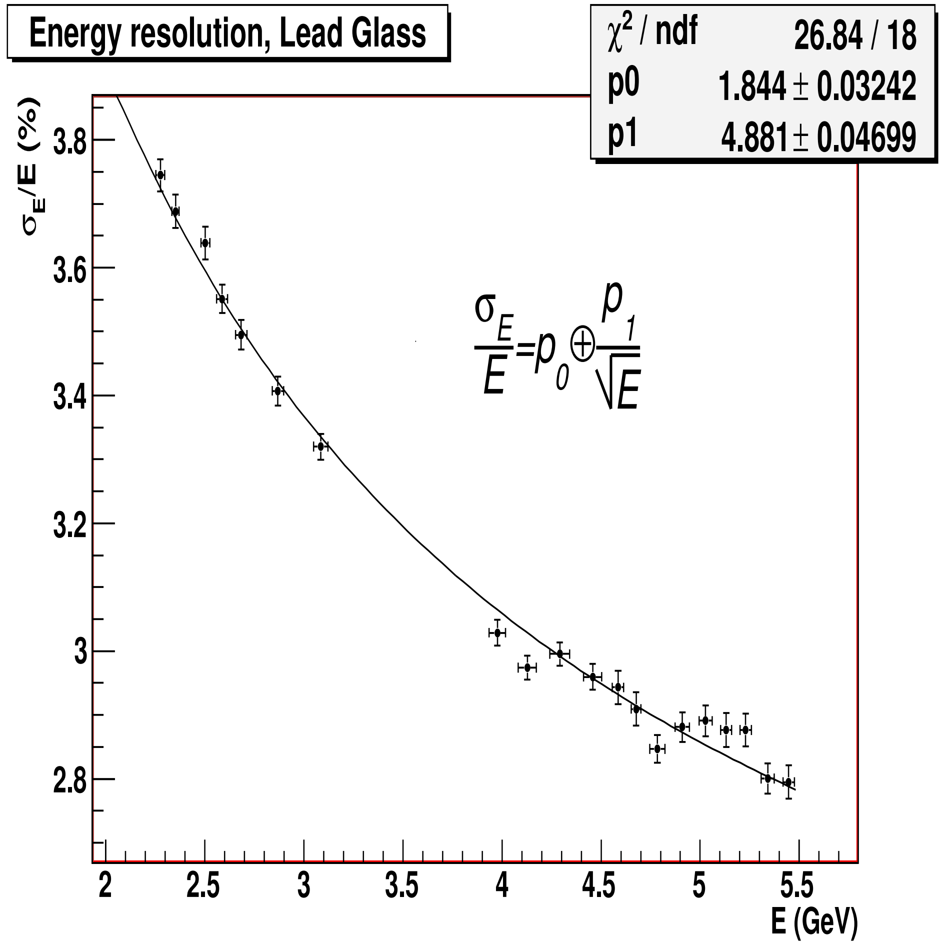

Figure 17: Measured energy resolution *versus* photon beam energy for the lead glass part of the calorimeter.

4.6.1 Absolute tagging ratios

During *PrimEx* data taking in the Fall of 2004, specialized calibration runs were periodically performed to determine the absolute normalization of the photon flux. For a calibration run, the experimental target is retracted and a Total Absorption Counter (TAC) is placed in the path of the photon beam. To avoid the radiation damage to the TAC, the electron beam intensity is lowered to $\sim 70 - 80pA$. The low intensity of calibration runs enables the use of the Tagger Master OR (MOR) signal as the data acquisition trigger. The MOR signal is formed by OR-ing the timing information from all or any of the 61 T-counters. Using the MOR trigger enables one to directly count the number of electrons that hit the tagging counters.

Absolute tagging ratios are defined for each of the T-counters as:

$$R^i_{absolute} = \frac{N^{TAC}_{\gamma \cdot e^i}}{N^i_e} \tag{12}$$

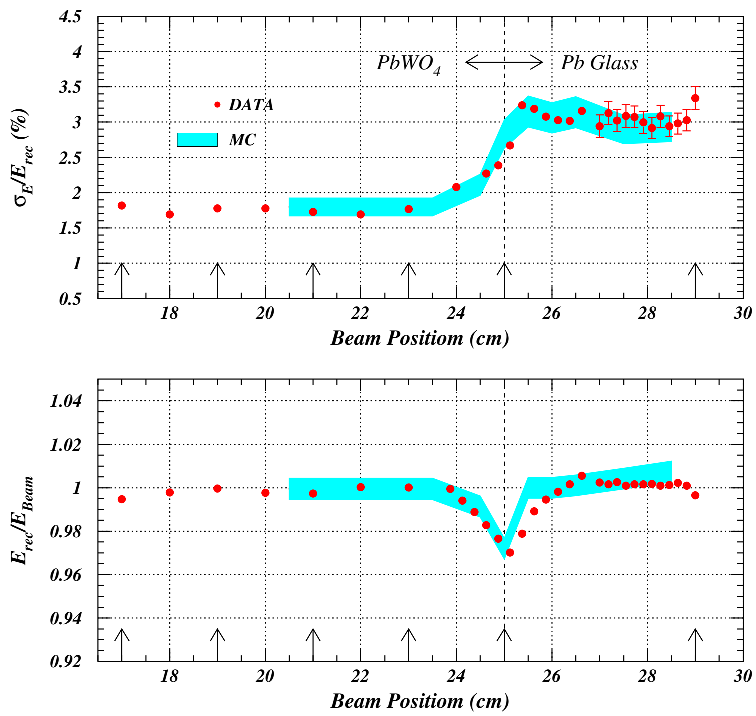

Figure 18: Beam test results for the transition region between $PbWO_4$ and lead glass modules. Top: energy resolution. Bottom: relative reconstructed energy *versus* position. The gray bands indicate Monte Carlo simulations.

where N_e^i is the number of electrons registered in the T-counter i and $N_{\gamma \cdot e^i}^{TAC}$ is the number of photons registered by the TAC in coincidence with an electron in the T-counter i.

A number of possible systematic errors associated with the determination of the absolute tagging ratios were studied in our 2004 run. These included:

- effects of incident electron beam intensity on absolute tagging ratios,
- effects of photon collimator size,
- effects of collimator position misalignment,
- effects of HYCAL scraping due to beam mis-steering,
- long and short term reproducibility of tagging ratios,
- effects of the pair spectrometer dipole field on the tagging ratios,
- absorption in the target.

The details of these studies are given in an appendix, with the general conclusion that the overall uncertainty in the flux determination, both systematic and statistical, was found to be 1%.

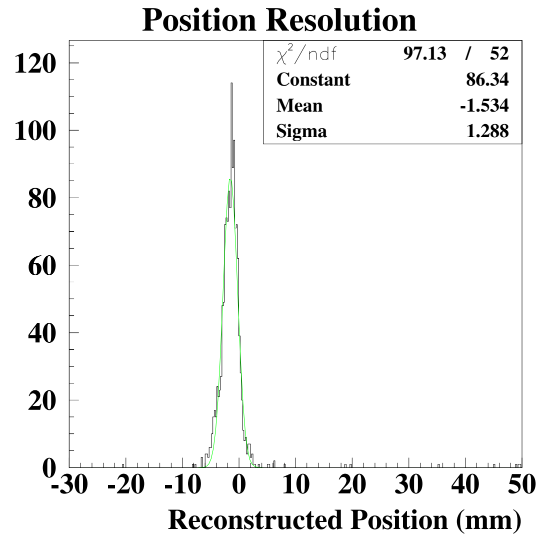

Figure 19: Distribution of reconstructed positions at the boundary between two lead tungstate crystal detectors.

4.6.2 Relative tagging ratios measured with pair production

The pair spectrometer is designed for relative in-situ monitoring of the photon flux. It uses the experimental target to convert a fraction of the photons into e^+e^- pairs. These are deflected in the field of a dipole magnet downstream of the target and are registered in plastic scintillator detectors on both sides of the beam-line. The relative tagging ratios per T-counter are defined as:

$$R^i_{relative} = \frac{N^{PS}_{e^+e^-\cdot e^i}}{N^i_e} \tag{13}$$

where N_{e_i} is the number of electrons registered in T-counter i and $N^{PS}_{e^+e^-\cdot e^i}$ is the number of e^+e^- pairs registered by the PS in coincidence with an electron in T-counter i.

During our production data taking in the Fall of 2004, we utilized a random, (*i.e.* not related to the beam), clock trigger set up to measure $R^i_{relative}$. The use of the random trigger enables a direct counting of the number of electrons in the tagging counters and it gives the advantage of being insensitive to beam intensity variations.

During a test run in 2002, the pair spectrometer was used to verify that the tagging ratios measured at the low intensities of the normalization (TAC) runs, reflect those at the higher rates of the production data taking. This was possible since the pair spectrometer, though a relative measure, is able to operate over a broad range of photon intensities. The results of this study are summarized in figure 25.

In the production run, the relative tagging ratios were found decrease slightly (less than 1%) towards the end of the run. This effect was traced to leakage current from other experimental halls. Data from the pair spectrometer enabled the flux determination to be corrected for this effect.

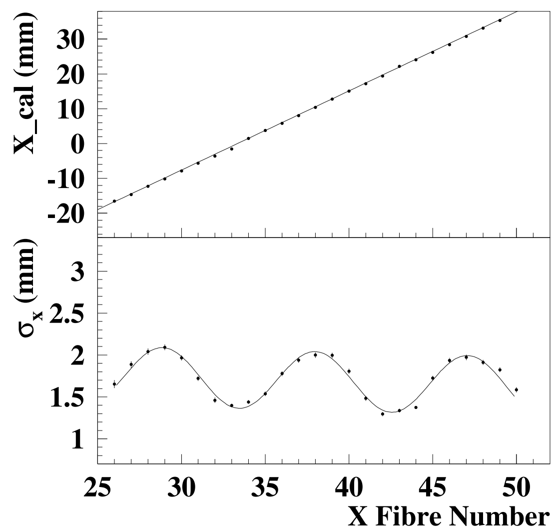

Figure 20: Reconstructed *versus* actual position (top) and position resolution (bottom) across the face of $PbWO_4$ crystal array.

4.7 Photon beam position monitor

A photon beam position detector was constructed by the collaboration that provided continuous real time photon beam position and profile information during the first experiment, as well as information in the data stream for off-line data analysis. This detector consists of two identical modules crossed at right angles to each other (as shown in figure 26) to give the beam profile along both x and y directions. Each module is a linear hodoscope of multi-channel Bicron scintillating fibers (the x module has 61 channels and the y module has 62) forming a plane perpendicular to the photon beam. This detector is mounted on a remotely controlled table with x and y motion placed just behind the HYCAL in the nominal beam path. Each scintillation fiber has dimensions of $2 \times 2 \times 13$ mm^3. The scintillating light from the fibers is transmitted through the light guide and is detected by four 16-channel R5600-M16 Hamamatsu PMTs. A compact electronics module provides 64 channels of amplifier and discriminators for anode signals, then converts them to ECL readout through a time-over-threshold circuit. The ECL signals are sent over to SIS3801-256-flat scalars and read into the EPICS system. During the run, the x and y beam profiles were displayed through a GUI for on-line beam control (shown in figure 27) and read into the DAQ for off-line analysis. This device performed well during the experiment and provided an excellent beam diagnosis tool.

4.8 Data acquisition and trigger

The *PrimEx* data acquisition system must read out over 2200 channels of ADC and TDC information coming from five different detector systems. These include the HYCAL calorimeter, the HYCAL veto, the pair spectrometer, the total absorption counter, and the Hall B

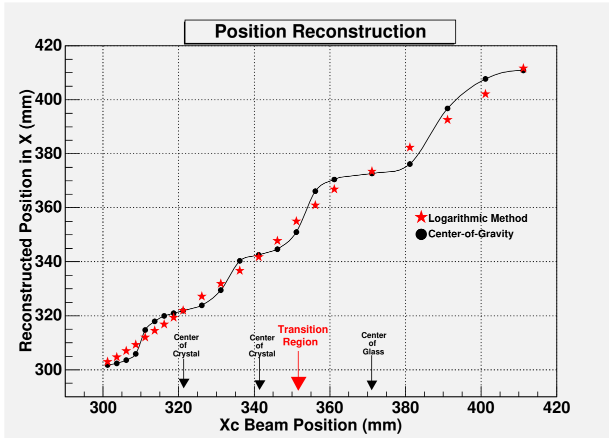

Figure 21: Reconstructed *versus* impact coordinate at the transition region of the HYCAL calorimeter.

photon tagger. The digitization electronics will span at least three Fastbus crates which must be coordinated for proper event reconstruction.

The *PrimEx* data acquisition system is a CODA based Fastbus system utilizing the JLab designed Trigger Supervisor module. In addition to the three Fastbus crates, this system includes one CAMAC crate, one VME crate, and one hybrid VME/VXI crate. Electronics occupying six NIM crates are also needed for the first stages of the trigger. A big advantage of the CODA/Trigger Supervisor system is the ability to run in fully buffered mode. In this mode, events are buffered in the digitization modules themselves allowing the modules to be live while being readout. This significantly decreases the dead time of the experiment. All of the electronics needed for the *PrimEx* DAQ and trigger electronics has been procured and is on site at JLab.

4.8.1 Trigger

The *PrimEx* trigger is formed from the last stage dynode signals from HYCAL. The anode signals are sent directly to the Fastbus ADC modules via long RG58 cables. The trigger initially constructed for the 2004 *PrimEx* run would have looked for multiple clusters in HYCAL separated by at least 15 cm. This was done by fanning in strips of like detectors ($PbWO_4$ and Pb-glass are done separately) which span the calorimeter in both the horizontal and vertical directions. In the $PbWO_4$ region of the calorimeter the strips are either seven or eight detector units wide, and in the Pb-glass the strips are either three or four detector units wide. There are seven such strips in the horizontal direction, and seven strips in the vertical direction. Using strips in this fashion ensures at least 50% of the energy deposited in one cluster will be seen by a discriminator. Each strip was discriminated at a level of one half of the minimum energy π^o decay photon we wish to detect. This level was set to 0.5 GeV since we wish to accept all events with photon energies 1 GeV or higher. The seven strips of each direction are taken to form a 14-bit word which was then used to access an address of a Memory Mapping Unit (CAEN C542). Patterns in which either (i) two non-adjacent strips

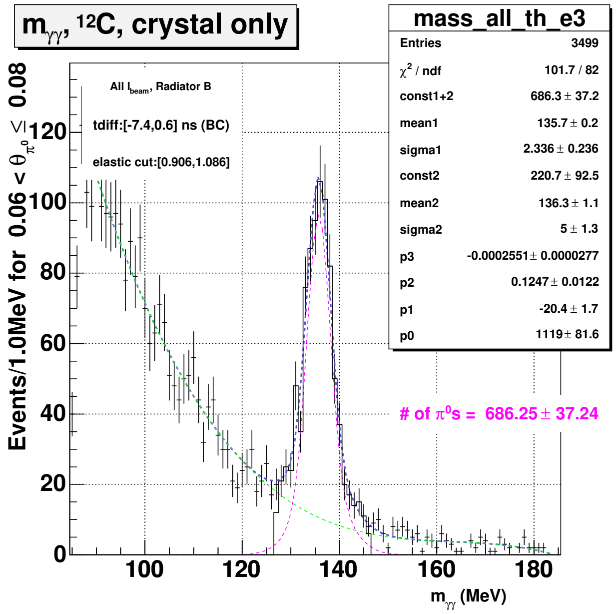

Figure 22: Distribution of two gamma invariant mass from the experimental data set for one production angle bin.

fire in one direction or (ii) two adjacent strips fire in both directions would have created a trigger.

However, in the commissioning period preceding the 2004 run, it was discovered that reasonable trigger rates are obtained using a trigger based on the total energy sum in HYCAL. For this reason, it was decided to take data with the more conservative and conceptually simpler total energy sum trigger. By using the energy sums already established for the trigger strips, only one additional level of signal fan-in was required to form the total energy sum. The energy sum trigger threshold was set at approximately 2 GeV for the 2004 run, and the trigger rate for the ^{12}C running was a modest, by Hall B standards, $1.2kHz$. We propose to use the same total energy sum trigger for the next *PrimEx* run.

The UVA120 and 125 linear fan-in and discriminator modules were chosen for the *PrimEx* trigger electronics because of the large number of channels (36 for the UVA120 module) and the economic advantage over commercial modules. The specific needs of the *PrimEx* trigger required some special modifications to both the UVA120 and its sister module, the UVA125. One significant modification in the UVA120 design was to make both outputs inverting. This allows the module itself to be used as both a splitter and inverter for the dynode signals, eliminating the need for additional hardware. The UVA125 is used for the last stage of fan-in and discrimination, and has four separate sections. Each section has a nine-input linear fan-in and two built-in discriminators. The timing of the discriminators is determined by the discriminator with the lower threshold, making the timing properties better than single leading edge discriminators. The UVA125 modules can have the discriminator thresholds set via externally supplied voltages. These voltages will be supplied via a CAMAC DAC module (digital-to-analog converter) so that the thresholds may be adjusted remotely without making an access to the experimental hall.

Figure 23: The light monitoring box mounted under HYCAL.

The only user controlled part of the trigger is the DAC, which is housed in a CAMAC crate in Hall B. The DAC is used to set the threshold for the energy sum trigger. The CAMAC crate is controlled remotely over the internet, through a Kinetic Systems GPIB CAMAC controller and National Instruments GPIB E-Net device.

5 Preliminary Results from the 2004 Run

5.1 π^o Photoproduction Cross Section Extraction

The *PrimEx* Collaboration has implemented three parallel data analysis procedures to extract the neutral pion lifetime. The primary considerations in event selection involve (1)HYCAL - Tagger timing information, (2) the invariant mass of the photons detected in the HYCAL, and (3), the elasticity of the candidate π^o events, where elasticity is defined as $\frac{E_{\gamma_1}+E_{\gamma_2}}{E_{tagger}}$.

5.1.1 Analysis I

The first analysis involves an event selection procedure which utilizes normalized probability distributions for each of the above mentioned quantities. In this analysis, the total probability of a valid event is given by the product of each of these probabilities as follows:

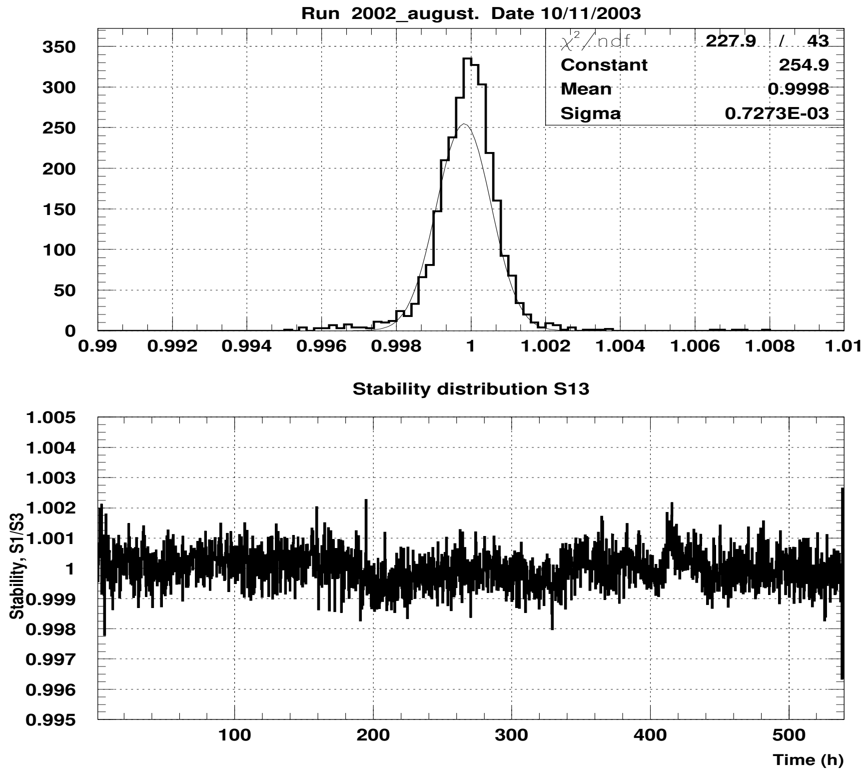

Figure 24: Stability of the light monitoring system.

$$Total\ Probability = Timing \quad \times \quad Invariant\ Mass \quad \times \quad Elasticity \tag{14}$$

An example of such a likelihood spectrum is shown in figure 28. For pion candidate events which are in coincidence with multiple photons on the tagger, this enables the selection of the best photon. Extensive studies of the inefficiencies of this selection procedure have been performed and found to have negligible effect on the resulting yield.

With this event selection procedure, the correlation between elasticity and reconstructed invariant mass is examined, and a new quantity, termed the "hybrid mass" is defined for each event. As indicated in figure 29, the hybrid mass is a quantity which contains combined information on the elasticity and invariant mass.

A plot of the hybrid mass *versus* pion angle is shown in figure 30. A cut on the hybrid mass provides a clean separation of the pion events and the resulting angular distribution is shown in figure 31.

5.1.2 Analysis II

The event selection criteria for Analyses I and II are very similar, utilizing nearly the same runs, energy thresholds, timing cuts and fiducial volumes. One difference is that Analysis II does not use a likelihood analysis to select the best energy clusters and Tagger hit in

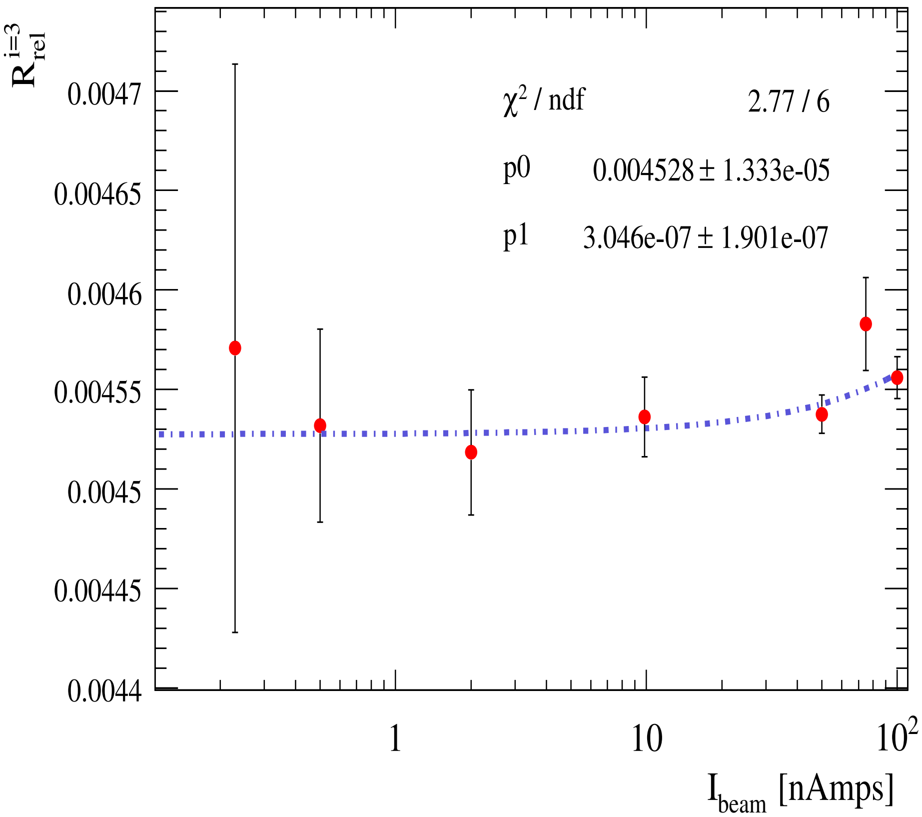

Figure 25: Relative tagging ratios measured over a range of photons rates spanning those of the normalizations runs to those of the π^o production runs.

events where there are multiple events in HYCAL and/or the Tagger. In the case of three or more HYCAL hits, all permutations of the two-photon invariant mass are considered and are allowed to increment the two-photon invariant mass distributions. In the case of multiple Tagger hits, a cut is applied to the HYCAL-Tagger timing distribution, shown in figure 32, and all tagger hits within this window are analyzed. Peak and background fitting is applied to the timing distribution to estimate the number of in-time accidental events within the accepted time window.

Both Analysis I and II utilize the correlation of coherent pion production to cluster at two photon invariant mass $m_{\gamma\gamma} = 135MeV$, and at Elasticity=$(E_1 + E_2)/E_{tag} = 1$. In Analysis II, the data at fixed angle are binned into slices in Elasticity, and for data within a given slice in Elasticity a histogram is constructed for the two-photon invariant mass distribution. An example of this is shown in figure 33, and there is a corresponding histogram for each slice of elasticity and at each angle. The π^o signal can be clearly seen in figure 33, and the number of π^o counts is found by fitting the data with a double Gaussian peak and polynomial background. The next step is to plot the number of π^o events at a fixed angle as a function of elasticity. An example of this is shown in figure 34, which shows a strong coherent signal at Elasticity=1, and very significant inelastic π^o production at lower elasticities. The elasticity distributions, one at each pion angle, are fit with a double Gaussian peak and polynomial

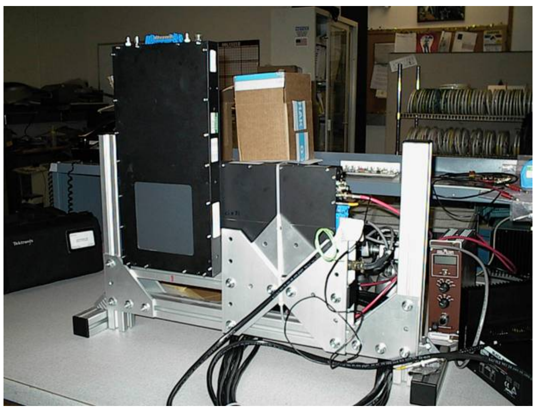

Figure 26: The *PrimEx* photon beam position detector.

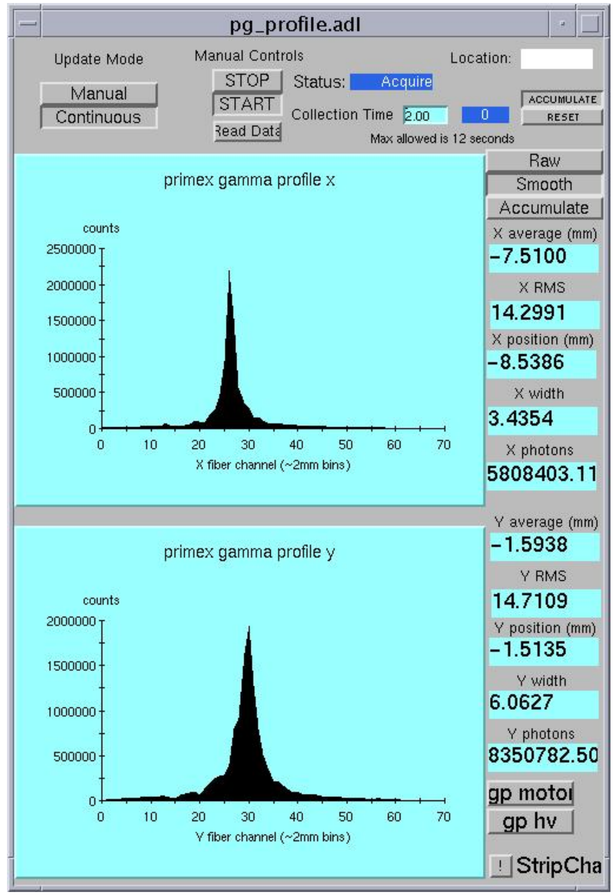

Figure 27: Photon beam position on-line display.

backgrounds. The resulting coherent π^o yields as a function of angle are shown in figure 35. The data exhibit a very prominent Primakoff peak at low angles, and then the strong nuclear coherent peak at angles from 1 to 2 degrees. Fits to this yield curve are used to extract the radiative width of the π^o. Figure 36 shows the extracted yields for ^{208}Pb. For the lead target, the nuclear coherent production is strongly suppressed by final state absorption.

The event selections for Analysis II and III are similar, with the biggest difference being the method for handling multiple tagger hits. In Analysis III, no effort is made to find the "best" Tagger hit, and the first Tagger hit reported in the database within the HYCAL-Tagger timing cut is utilized for the analysis. Because a narrow range of Tagger energies was utilized in the first *PrimEx* experiment, 10%, it turns out that this procedure has little effect on the elasticity resolution.

5.1.3 Analysis III

Event selection for Analysis III is similar to Analyses I and II, although a more restrictive set of runs was used in the analysis. The statistics in Analysis III are approximately 50% of the statistics in Analysis I and II.

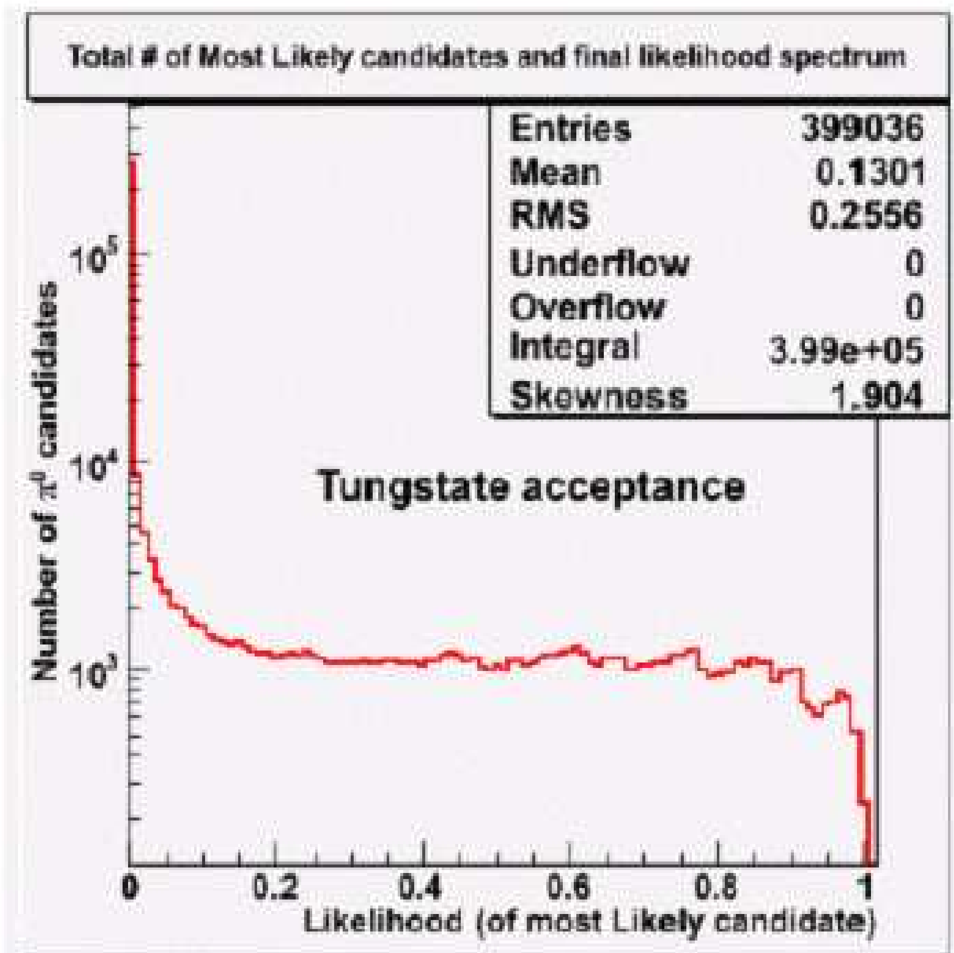

Figure 28: Event selection for Analysis I: Final likelihood for most likely entries.The "choppiness" of the distribution is an artifact of the electron beam time structure.

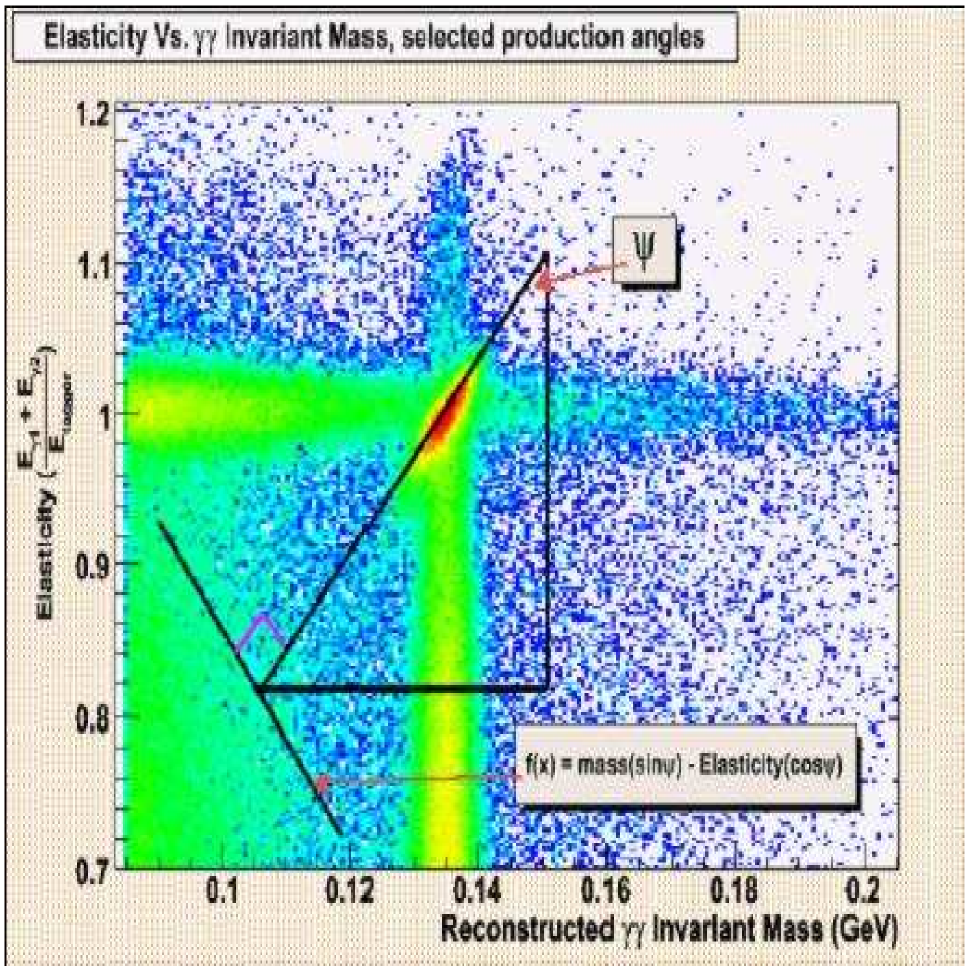

Figure 29: Correlation between mass and elasticity for selected angles.

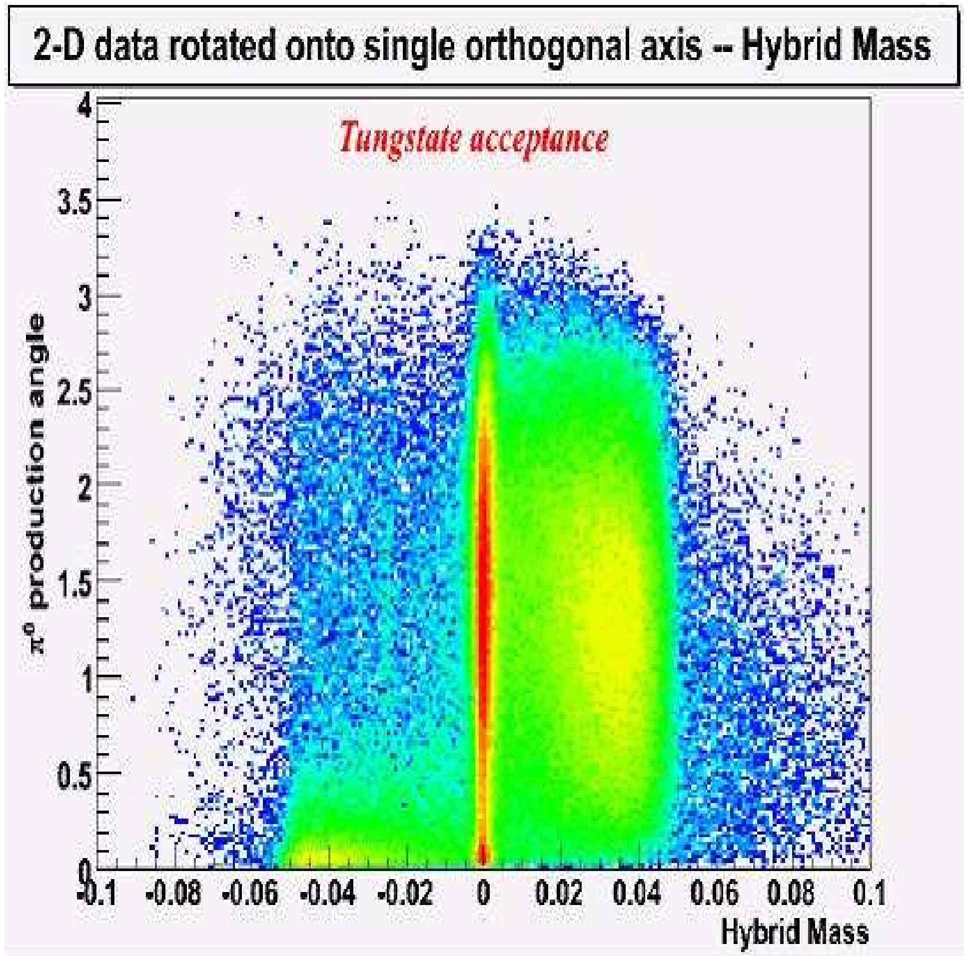

Figure 30: Projection of data onto the orthogonal axis indicated in the previous figure.

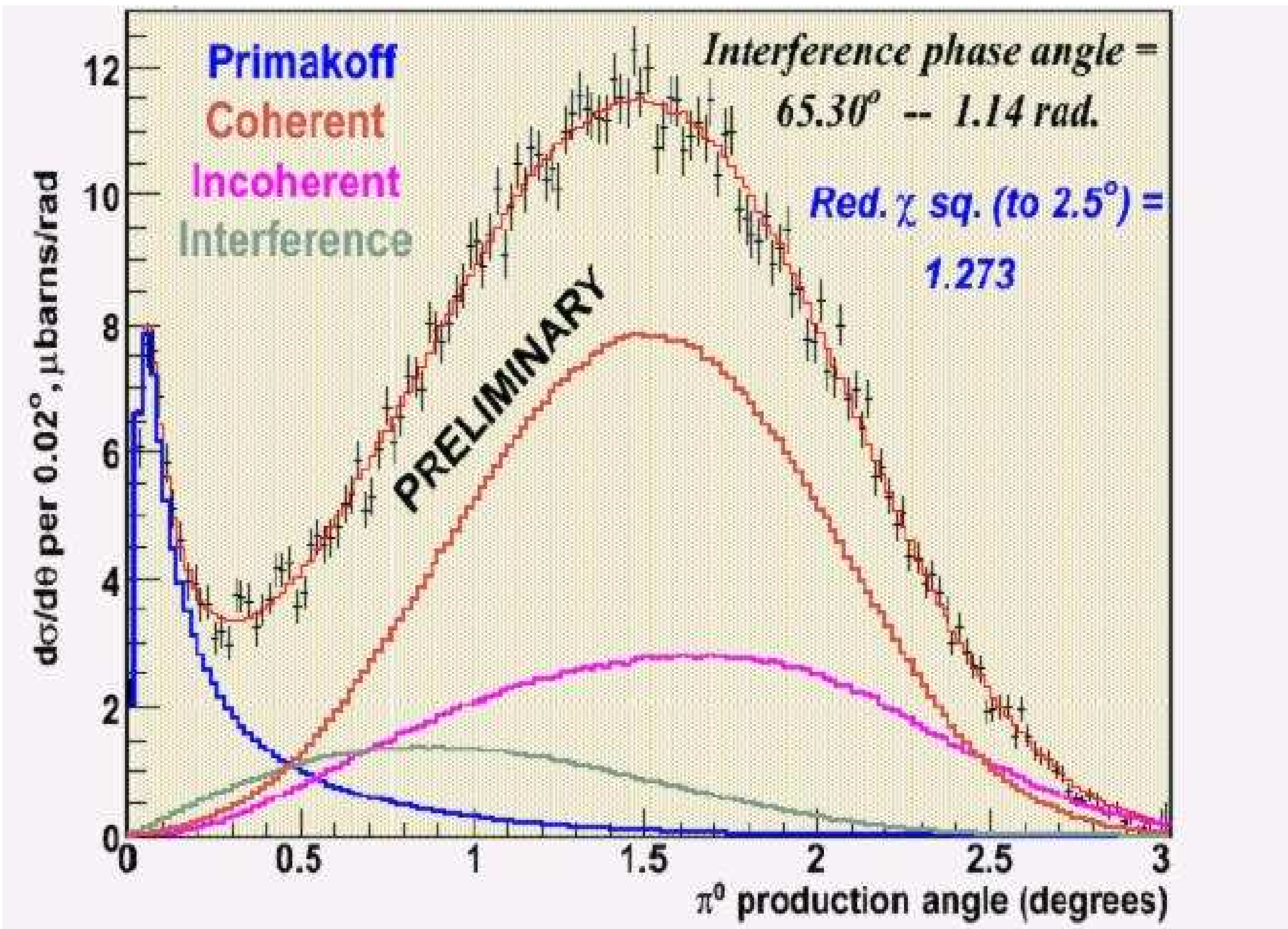

Figure 31: Normalized yields with fit to 2.5°, HYCAL lead tungstate acceptance.

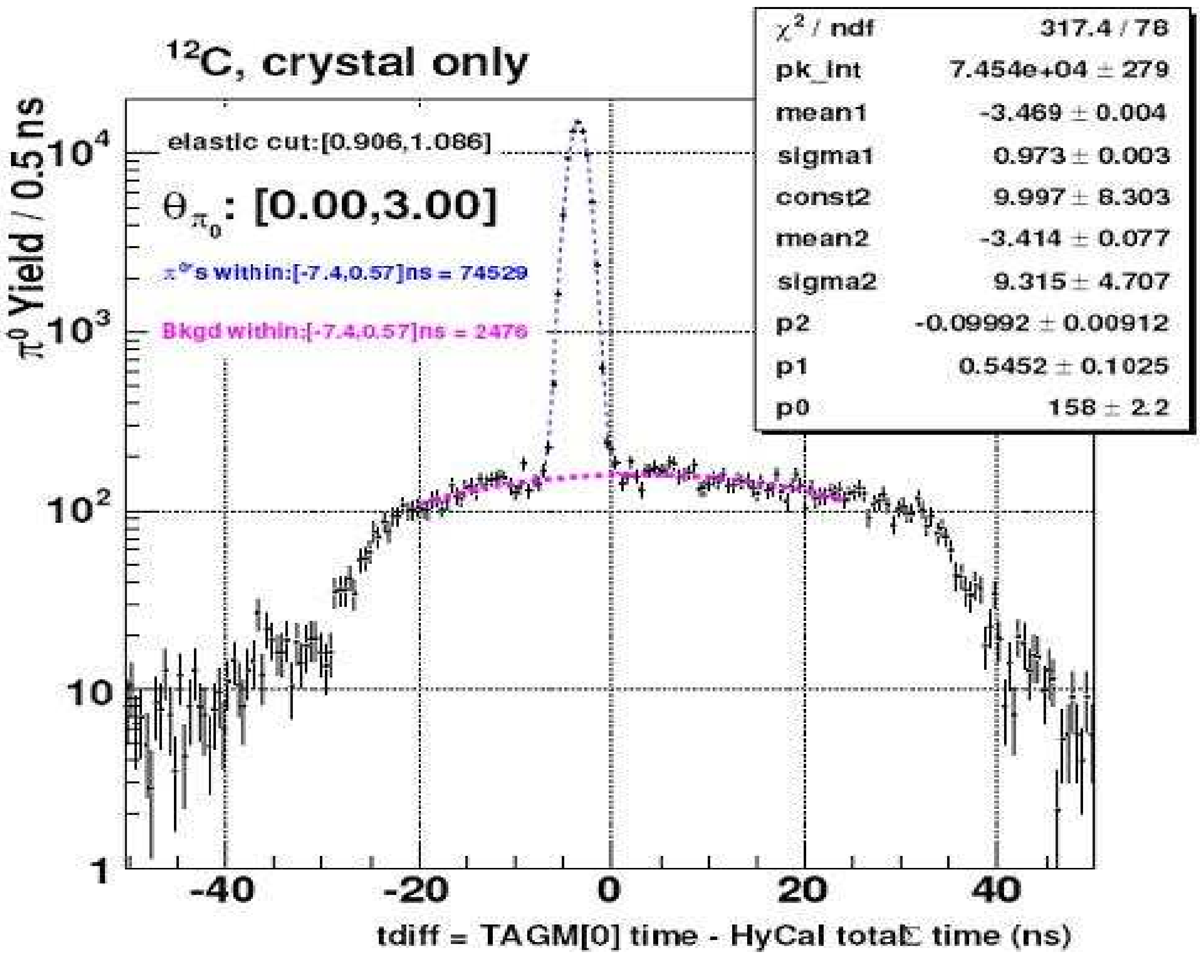

Figure 32: π^o HYCAL - Tagger timing spectrum for ^{12}C using "best" candidate approach. Each data point comes from a fit to the $m_{\gamma\gamma}$ distribution formed for its particular 0.5 ns wide timing slice.

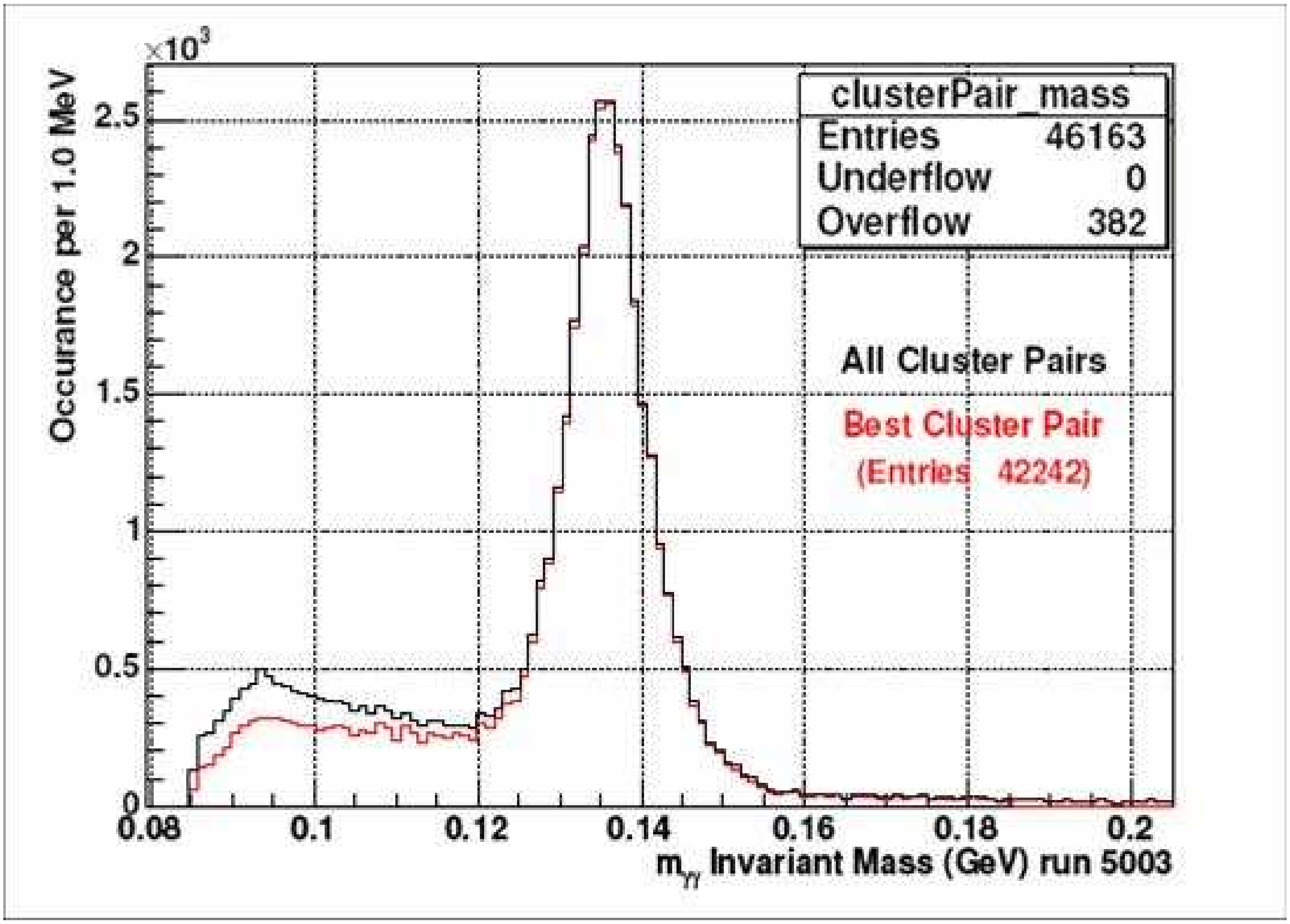

Figure 33: Cluster pair invariant mass distributions using two different collection methods. The black histogram is formed by considering all possible pair combinations. The red histogram is formed by using only the best pair combination (the one closest to the overall peak mean.)

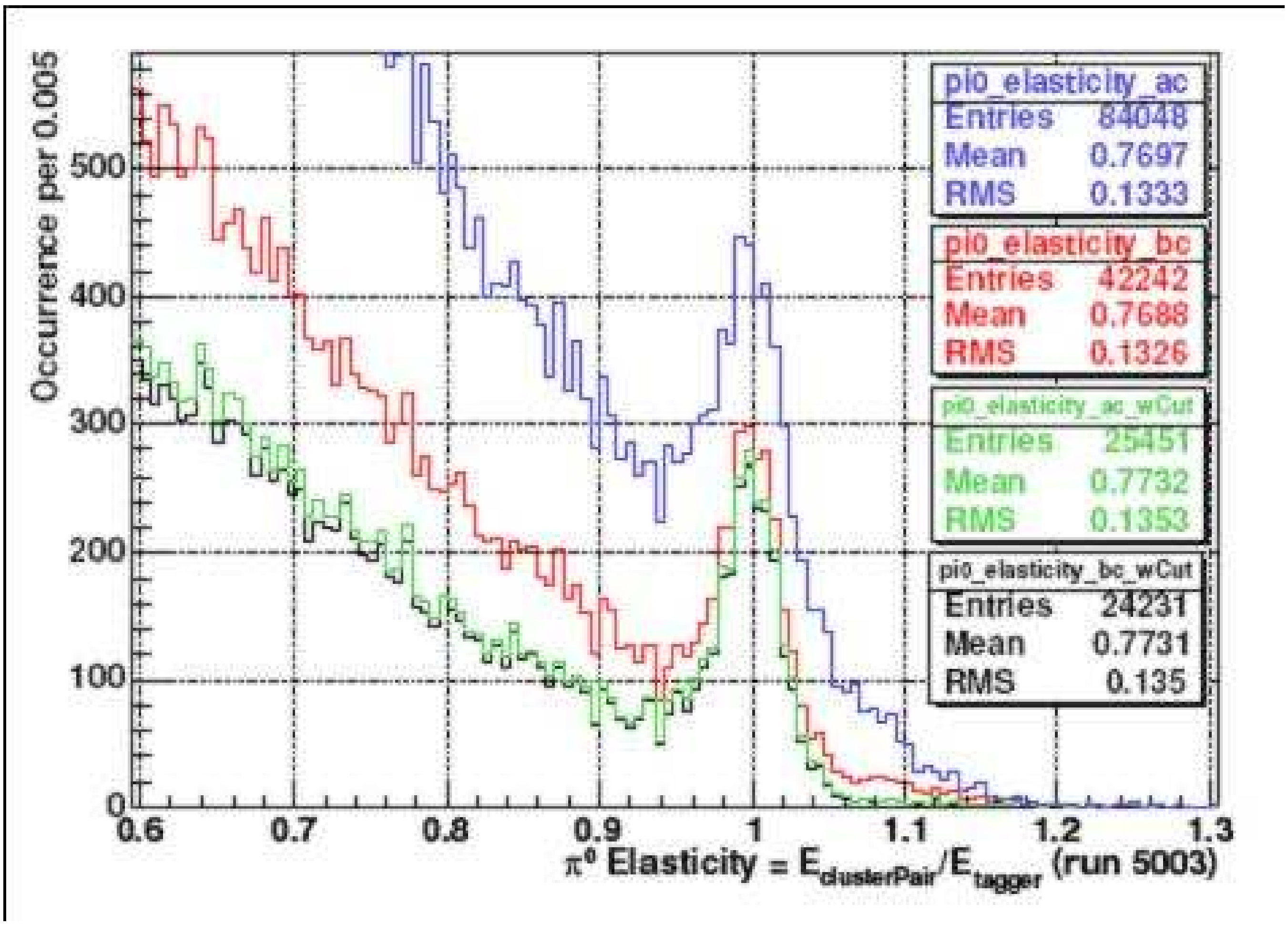

Figure 34: π^o elasticity study. The top two histograms (blue and red) are for a $\pm 100ns$ timing cut, the bottom two histograms (green and black) are for a $-7.4, +0.6$ ns timing cut. The "ac" and "bc" labels refer to all candidate and best candidate approaches, respectively.

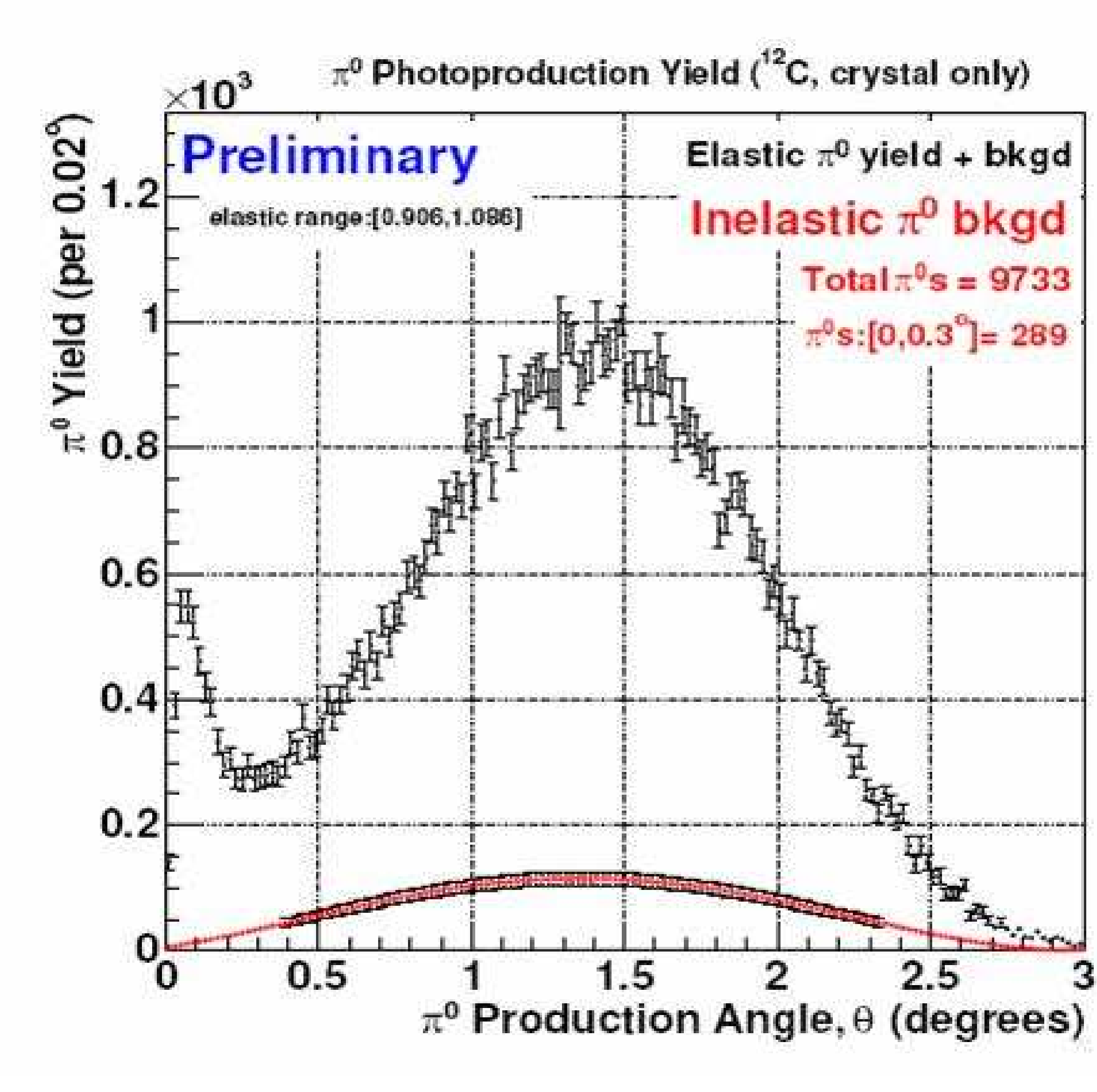

Figure 35: Uncorrected elastic π^o yield for ^{12}C shown with background correction in red.

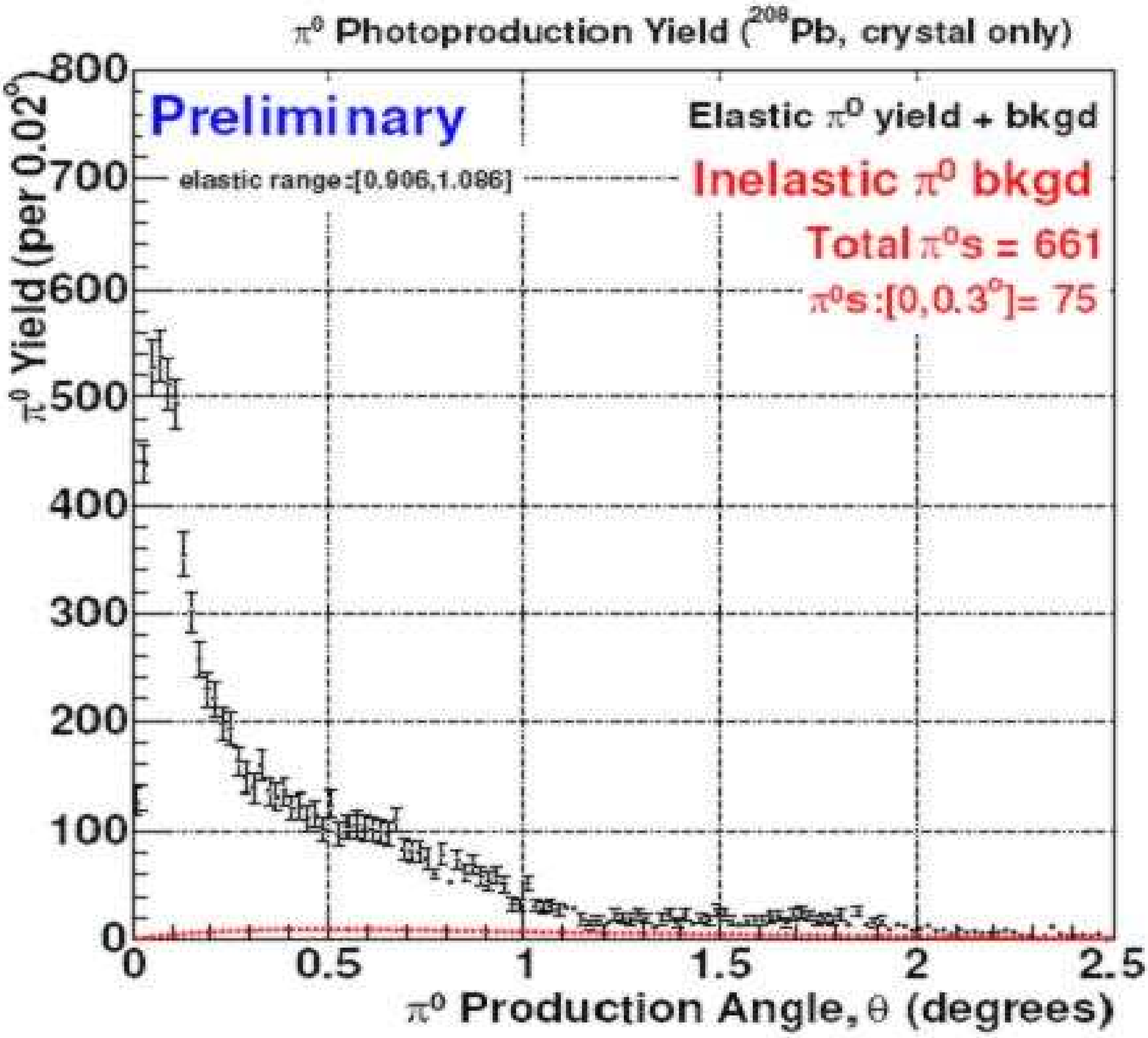

Figure 36: Uncorrected elastic π^o yield for ^{208}Pb shown with background correction in red.

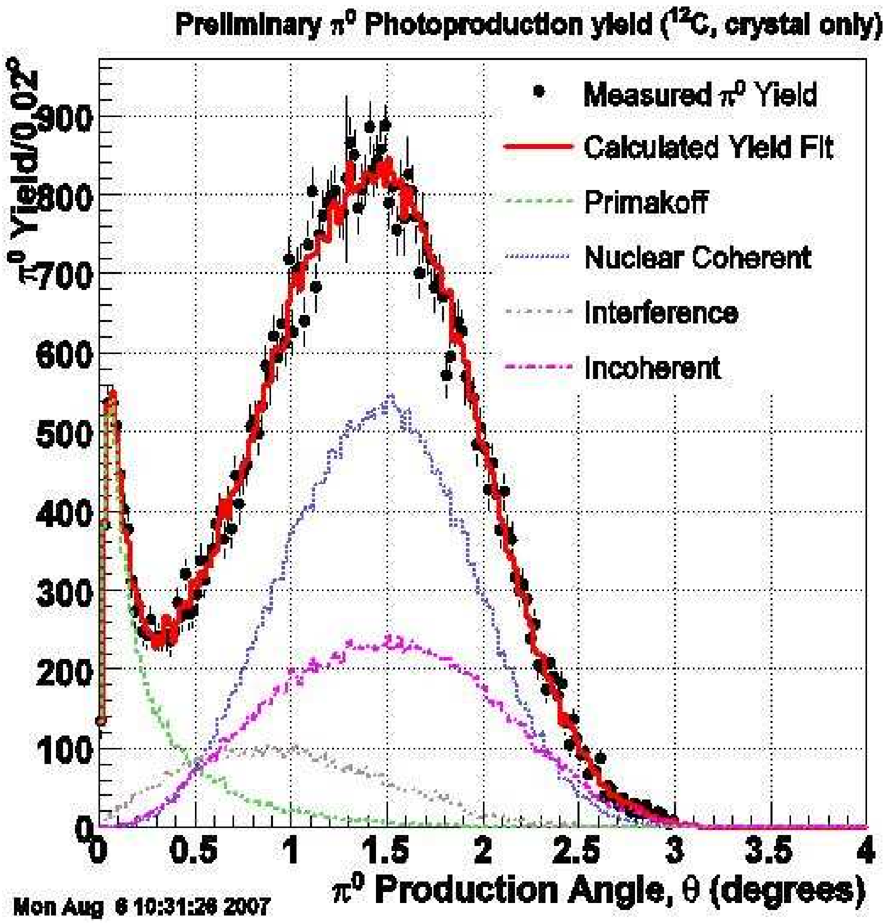

Figure 37: Yields *versus* pion angle from Analysis method II, ^{12}C.

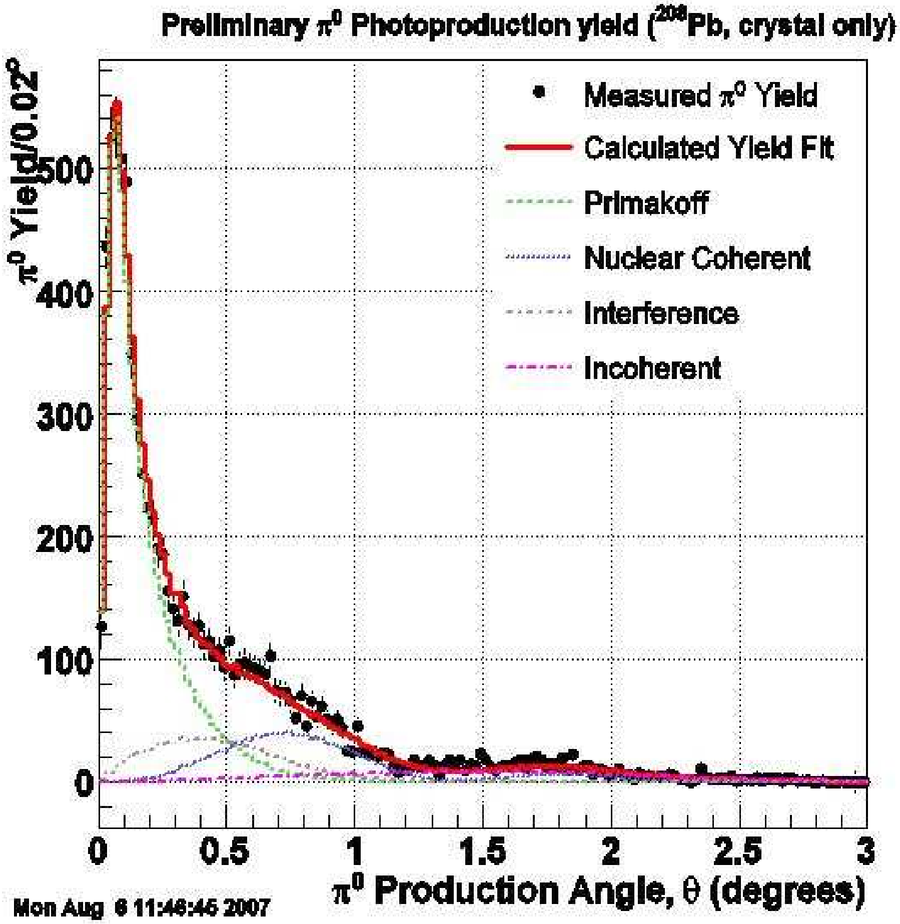

Figure 38: Yields *versus* pion angle from Analysis method II, ^{208}Pb.

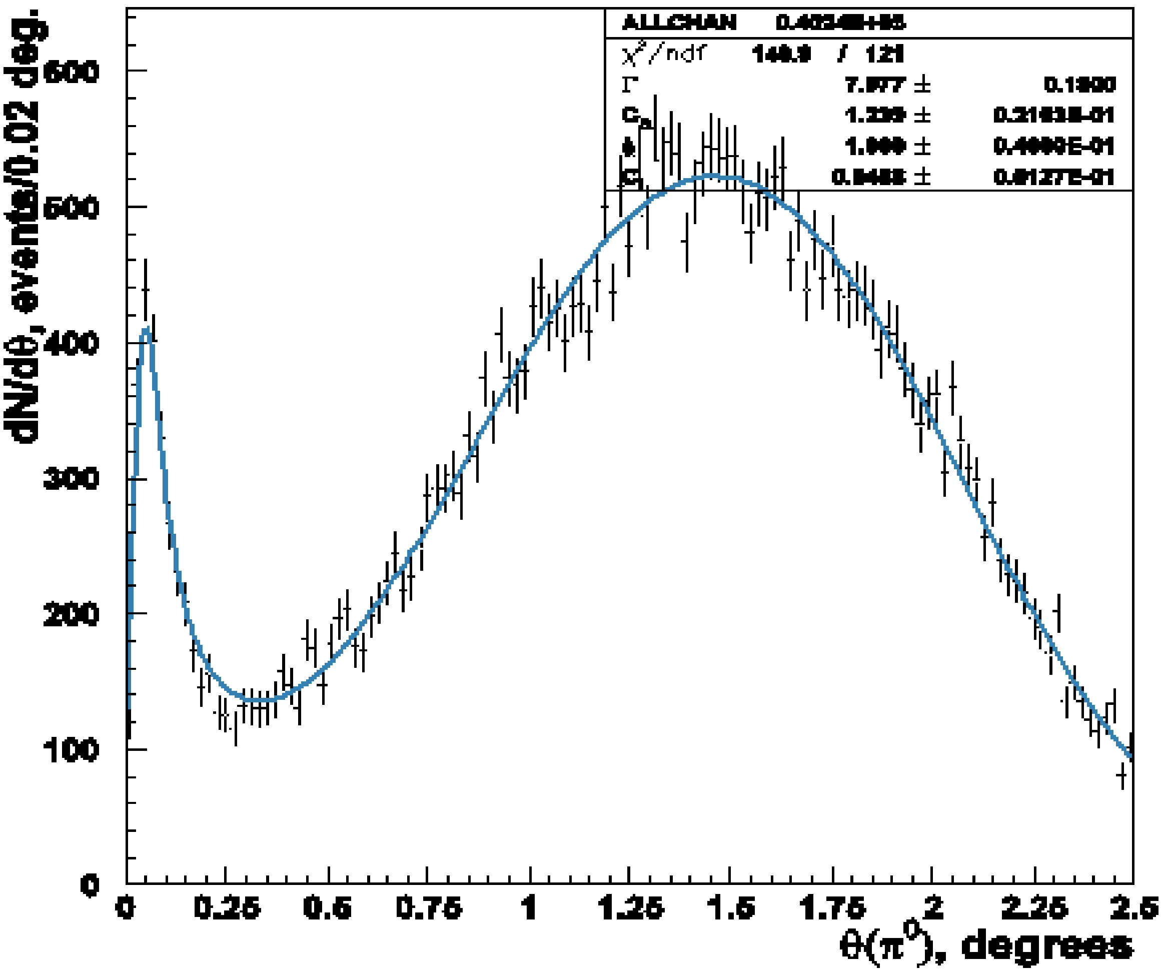

Figure 39: Fit to the experimental yields, Analysis method III, ^{12}C.

Kinematic fitting is used in Analysis III to find the yield of coherent pions. At each pion angle, the energies of photon pairs are varied to fit the condition Elasticity=1 with the constraint that chi-squared is minimized. This procedure optimizes (i) the two-photon invariant mass, and (ii) the π^o angular resolution. The resulting pion yields are shown in figures 39 and 40.

Comparing the three analyses, both Analysis I and III minimize the number of distributions that must be fit with a peak and background, which is exactly equal to the number of pion angular bins, whereas in Analysis II approximately 1000 spectra must be fit. It can be expected that Analyses I and III will have comparable two-photon invariant mass resolutions, and Analysis III will have the better pion angular resolution. We expect that Analysis II will have the simplest, most non-structured background of the three analyses. Analyses I and II have the greatest statistics, and Analysis III utilized only the very best production runs.

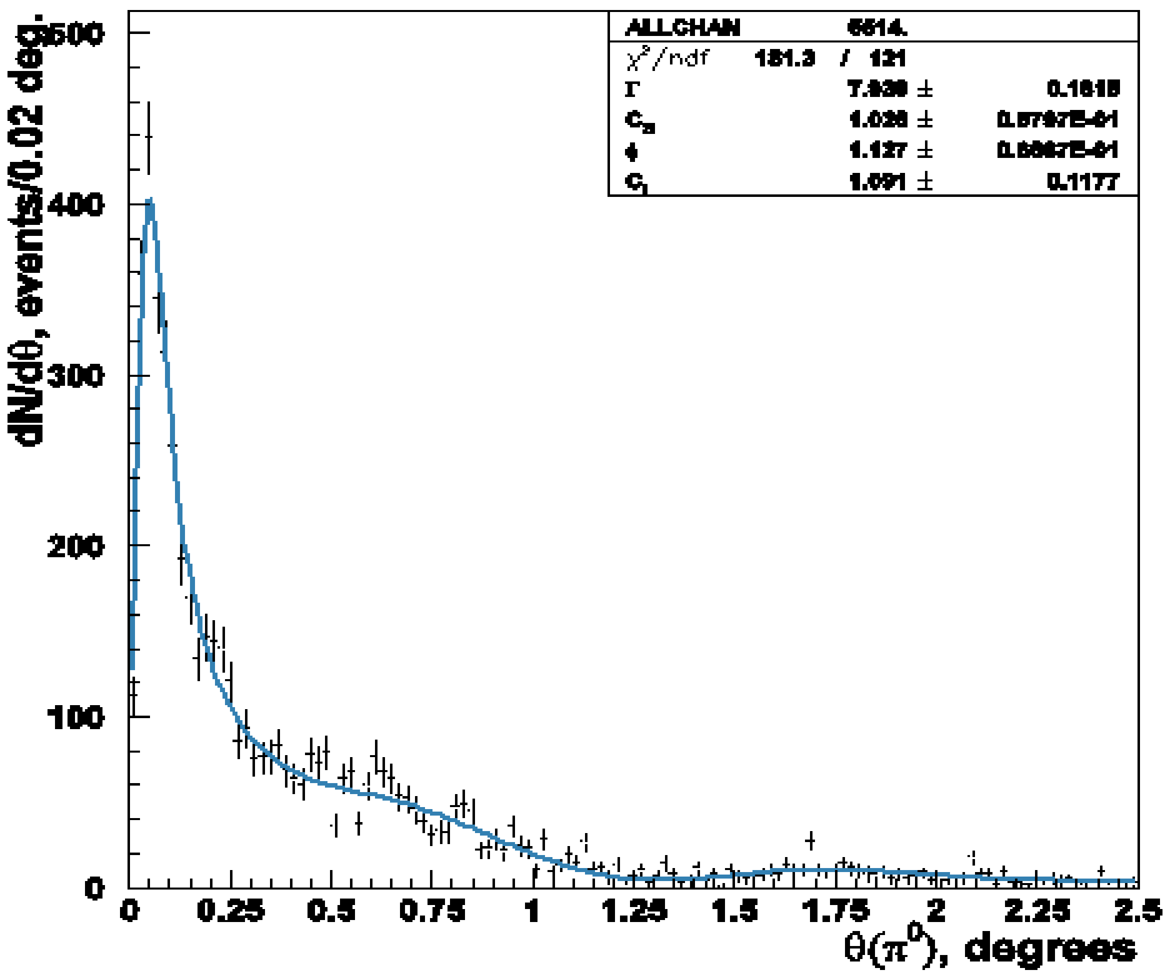

Figure 40: Fit to the experimental yields, Analysis method III, ^{208}Pb.

5.2 Theoretical Study of π^o Forward Photoproduction off Complex Nuclei

The coherent photoproduction of pions:

$$\gamma + A \rightarrow \pi^0 + A \tag{15}$$

can be described by the sum of Coulomb T_C and Strong T_S amplitudes. Including incoherent production, the differential cross section is:

$$\begin{aligned} \frac{d\sigma}{d\Omega} &= \frac{k^2}{\pi}\frac{d\sigma}{dt} = \mid T_C + T_S \mid^2 + \frac{d\sigma_{inc}}{d\Omega} \\ &= |T_C|^2 + |T_S|^2 + 2(ReT_C ReT_S + ImT_C ImT_S) + \frac{d\sigma_{inc}}{d\Omega} \end{aligned} \tag{16}$$

where $\frac{d\sigma_{inc}}{d\Omega}$ is the incoherent cross section *i.e.* processes involving target nucleus excitation or break up. Each of these amplitudes factorizes into a photoproduction amplitude on a nucleon multiplied by a corresponding form factor. In addition, these form factors must be corrected for final state interactions of the outgoing pion as well as consideration of the photon shadowing effect in nuclear matter.

In order to extract the π^0 radiative decay width from the *PrimEx* data with high precision, the shapes of each term in equation 16 need be understood theoretically as accurately as possible. Below, we present the results of extensive studies of this subject.

5.2.1 The electromagnetic amplitude T_C

The effect of the pion Final State Interactions in nuclei (FSI) has been discussed in detail by Morpurgo [43]. In this work, the absorption of pions was considered by using the Distorted Wave Approximation (DWA). Calculations of the electromagnetic and strong form factors have been done with uniform nuclear density distribution $\rho(r)$. Based on these two assumptions, part of the correction to the form factors, which takes into account pion absorption in nuclei, was correctly obtained. However, the effect of pion rescattering to forward angles was not taken into account in this work. This effect is important in the Primakoff experiments since pions produced at modest angles can, as a result of final state interactions, rescatter to small angles. This effect was first considered by Fäldt [44] in non-diffractive production processes on nuclei in the framework of the Glauber theory of multiple scattering. For the strong amplitude, he started with a general expression, but only considered the case with equal total cross sections of incoming and produced particles. As to the electromagnetic amplitude, his expression (eq. 3.4 in [44]) does not describe the pion photoproduction correctly.

In the past several years, we developed a model [45, 50] based on Glauber theory of multiple scattering, taking into account the FSI of pions in nuclei and Fäldt's rescattering effect. The electromagnetic amplitude is expressed as [45]:

$$T_C = Z\sqrt{8\alpha\Gamma}(\frac{\beta}{m_\pi})^{3/2}\frac{k^2 sin\theta}{q^2+\Delta^2}F_C(q)$$

where the Coulomb form factor is given by:

$$\begin{aligned} F_C(q) &= \frac{q^2+\Delta^2}{q}\int J_1(qb)\frac{bd^2bdz}{(b^2+z^2)^{3/2}}e^{i\Delta z} \\ &\times \exp\left(-\frac{\sigma\prime}{2}\int_z^\infty \rho(b,z\prime)dz\prime\right)\int_0^{\sqrt{b^2+z^2}} x^2\rho(x)dx \end{aligned} \tag{17}$$

$$t=(k-p)^2=-q^2-\Delta^2=-4kpsin^2(\frac{\theta}{2})-(\frac{m_\pi^2}{2E})^2$$

$$\sigma'=\sigma\left(1-i\frac{Ref(0)}{Imf(0)}\right)=\frac{4\pi}{ik}f(0)$$

Here $\rho(r)$ is the nuclear density, $J_1(x)$ is the first order Bessel function, and f(0) is the amplitude for π^0 elastic scattering on the nucleon. One may notice that the Coulomb form factor F_C has an imaginary part due to longitudinal momentum transfer Δ and the presence of the ratio of the real to imaginary part of the pion-nucleon elastic forward amplitude in the absorption factor.

In the calculation of the electromagnetic form factors, we have developed and included three new items: (1) the contribution of the imaginary part as described above; (2) the new and updated nuclear density distribution extracted from elastic electron-nuclei scattering, with parameters taken from the Fourier-Bessel analysis [47]; (3) estimation of the contribution of the nuclear excitation effects by photon exchange described below.

In addition to the coherent photoproduction in the Coulomb field, the production of pions with nuclear collective excitation (for instance, the giant dipole resonance) is possible. As shown in [49], such excitations lead to the inelastic form factor:

$$|F_n(q)|^2 \approx \frac{1.4N}{2m_pZAE_{av}}|t| \tag{18}$$

where m_p and E_{av} are the proton mass and average excitation energy, Z and N are the nuclear charge and neutron numbers, and A is the atomic mass. This expression should be compared with the second term in the expansion of the square of the elastic electromagnetic form factor: $F^2(q)\approx 1-\frac{R^2}{3}|t|$. This correction for lead is on the level of 0.1% [49]. Our estimation for carbon nuclei is about 10% relative to the second term in the form factor expansion. On the other hand, however, the longitudinal momentum transfer in π^o photoproduction with nuclear collective excitation is : $\Delta_{in}=\Delta+E_{av}$. The ratio of the cross section of the π^o photoproduction in the Coulomb field with nuclear excitation to "elastic" electromagnetic production can be estimated as:

$$\frac{\frac{d\sigma_{in}}{d\Omega}}{\frac{d\sigma_{el}}{d\Omega}} \approx \frac{(q^2+\Delta^2)^2}{(q^2+\Delta_{in}^2)^2}\frac{|F_n(q)|^2}{|F(q)|^2} \approx \frac{1.4N}{2m_pZAE_{av}}\frac{(q^2+\Delta^2)^2}{(q^2+\Delta_{in}^2)}$$

Choosing the average exitation energy for carbon as: $E_{av}\approx 20-25MeV$, one obtains for this ratio at the Coulomb peak ($q=\Delta$) to be $\sim 10^{-7}$. Therefore, the contribution from nuclear excitations can be safely neglected for both carbon and lead nuclei.

Our new calculations of the electromagnetic form factors for carbon and lead are shown in figure 41 and figure42. The values for pion nucleon total cross section and the ratio of real to imaginary part of the elastic $\pi^o N$ forward amplitude were taken as the average of that of the charged pions [48]: $\sigma(\pi^0 N) = 27.60 \pm 0.01mb, \quad \frac{Ref(0)}{Imf(0)} = -0.2 \pm 0.05$.

5.2.2 Strong amplitude T_S

As pointed out earlier, the strong amplitude T_S in Fäldt's work [44] was obtained for the specific case of equal absorption of initial and final particles only. We obtain a general expression for the strong amplitude T_S. In addition, we take into account the photon shadowing effect, the issue widely discussed in diffractive production [52, 53]. The amplitude T_S can be written in factorized form [51]:

$$T_S(q) = Ae^{i\Phi} Lksin\theta F_S \tag{19}$$

where the factor $e^{i\Phi} Lksin\theta$ is the nonspin-flip nucleon amplitude [51]. It is proportional to $sin\theta$ due to the transversality of the photon and the conservation of angular momentum. The phase Φ and constant L are parameters fitted from the experiment.

The strong form factor F_S can be written as the sum of three terms [45, 50]:

$$F_S = F_1 + F_2 + F_3 \tag{20}$$

where the F_1 is the usual strong form factor [43]; F_2 is the part of the form factor describing the rescattering effect [44] of photopions; the term F_3 is our new contribution in the strong part, which takes in account the photon shadowing effect in nuclei.

$$\begin{aligned}
F_1 &= \int e^{i\vec{q}\vec{b}} \rho(b,z) d^2b dz e^{i\Delta z} \exp(-\frac{\sigma\prime A}{2} \int_z^\infty \rho(b,z\prime)dz\prime) \\
F_2 &= -\frac{A\pi\sigma}{q} \int J_1(qb)\rho(b,z_1) \frac{\partial\rho(b,z_2)}{\partial b} bdbdz_1dz_2 e^{i\Delta z_1} \\
&\times \exp(-\frac{\sigma\prime A}{2} \int_{z_1}^\infty \rho(b,z')dz') \\
F_3(q) &= \frac{\pi\sigma A}{q} \int J_1(qb)\rho(b,z_1) \frac{\partial\rho(b,z_2)}{\partial b} \theta(z_2 - z_1) bdbdz_1dz_2 \\
&\times e^{i\Delta_\rho(z_1-z_2)+i\Delta z_2} \exp(-\frac{\sigma\prime A}{2} \int_{z_1}^\infty \rho(b,z\prime)dz)
\end{aligned} \tag{21}$$

where $\Delta_\rho = \frac{m^2\rho}{2E}$ is the longitudinal momentum transfer in the elementary reaction $\rho + N \rightarrow \pi^0 + N$.

The shadowing effect is the result of a two-step pion photoproduction process. The high energy photon first produces a vector meson, which then produces a pion on the nucleon.

Only the contribution from the ρ meson in the intermediate state is taken in account, since the contributions from ω and ϕ vector mesons are an order of magnitude smaller.

The results of form factor calculations with and without the shadowing effect are shown in figure 43 and figure 44 for carbon nuclei. As seen from these plots, the shadowing effect is an important contribution to the strong form factor in a few GeV energy range.

5.2.3 Incoherent cross section $\frac{d\sigma_{inc}}{d\Omega}$.

Incoherent photoproduction is the production of π^o's accompanied by target excitation or break up:

$$\gamma + A \rightarrow \pi^0 + A' \tag{22}$$

Two different theoretical approaches have been applied to study this process.

Glauber Theory Approach

We adopt the following expression for the incoherent cross section [55, 56]:

$$\frac{d\sigma_{inc}}{d\Omega} = (\frac{Z}{A}\frac{d\sigma_p}{d\Omega} + \frac{N}{A}\frac{d\sigma_n}{d\Omega})N(0,\sigma)(1-G(t)) \tag{23}$$

The incoherent cross section in equation 23 is the product of three factors:

1. The differential cross section of π^o production off the nucleon. We separate the photoproduction on protons and neutrons, as the π^o production on the proton has a Coulomb (Primakoff) part [58].

2. The factor 1-G(t) is the Pauli suppression factor, which forbids the mesons' incoherent production at small momentum transfer. The incoherent form factor G(t) was taken from [57].

   For lead nuclei, it is

   $$1 - G(t) = \frac{3}{4}(\frac{q}{k_F}) - \frac{1}{16}(\frac{q}{k_F})^3 \tag{24}$$

   and for carbon nuclei

   $$1 - G(t) = (1 + (\frac{qR}{\sqrt{15}})^4)\exp(-\frac{2q^2R^2}{15}) \tag{25}$$

3. The effective nucleon number $N(0,\sigma)$ is given by expression:

$$\begin{aligned} N(0,\sigma) &= \int \frac{1-e^{-\sigma T(b)}}{\sigma} d^2b \\ T(b) &= \int \rho(b,z)dz \end{aligned} \tag{26}$$

The results of our calculations of the incoherent cross sections for carbon are shown in the figure 45.

Cascade Model Approach

The nuclear incoherent (NI) π^o photoproduction cross section is also calculated by using an extended version of the Monte Carlo Multicollisional intranuclear Cascade model (MCMC). The model uses the Plain Wave Impulse Approximation (PWIA) for the π^0 photoproduction. In this approach, the NI cross section is proportional to the single nucleon cross section times a factor that accounts for the short range correlations[60]. The π^0- nucleus FSI and the shadowing effect of the incoming photon distort the PWIA due to the π^0 absorption and re-scattering. Furthermore, additional neutral pions can also be produced at forward angles in secondary scatterings. Such a complicated scenario can be described semi-classically as two correlated intranuclear cascade mechanisms triggered by the produced π^o and struck nucleon. In this approach, the dynamics of the nuclear ensemble is taken into account using the concept of interaction probability in a relativistic and time-dependent Monte Carlo algorithm.

The basic features and improvements of the MCMC model [61, 62, 63, 64] are: i) the inclusion of the π^0 photoproduction mechanism within 4.0 to 6.0 GeV in terms of ρ and ω exchange, constrained by the available data[65, 66], ii) the use of two different nuclear densities for carbon and lead[67], iii) the incorporation of an accurate momentum distribution for ^{12}C based on the global $1s$ and $1p$ proton knock-out data[68], iv) a rigorous non-stochastic Pauli-blocking both for the photoproduction and multiple $\pi^0 N$ scatterings, v) the implementation of the shadowing effect using a VMD model with formation time constraint[69], and vi) a consistent analysis of the full π^0- nucleus FSI, as well as the use of realistic (diffractive) angular distributions for the $\pi^0 N \to \pi^0 N$ elastic channel.

Most of the $\pi^0 N \to X$ channels relevant for the *PrimEx* were incorporated in the routine combining the properties of isospin invariance and time reversal of the strong interactions with the experimental results of charged pions. Collisions of the type $\pi N, \pi N^*, \pi\Delta, NN, NN^*$ and $N\Delta$ are taken into account. The collisions between pairs of pions are not considered due to a much lower pion density.

The comparison between Glauber and Cascade calculations on NI differential cross section is shown in figure 46. Their shapes are in reasonable agreement in the angular range of 1–5 degrees.

5.2.4 Conclusion

We used Glauber multiple scattering theory to study the electromagnetic and strong form factors in the $\gamma + A \to \pi^0 + A$ reaction on carbon and lead targets. These calculations include: (1) pion final state interaction in the nucleus, and (2) the photon shadowing effect. The nuclear incoherent π^0 photoproduction is extensively investigated by using both Glauber theory and the Cascade model. This study provides a solid foundation for us to fit the existing *PrimEx* data in order to extract the π^0 radiative decay width with high precision.

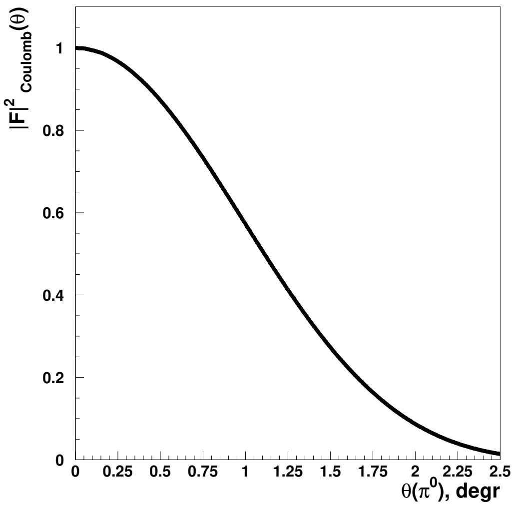

Figure 41: The square of the electromagnetic form factor for carbon.

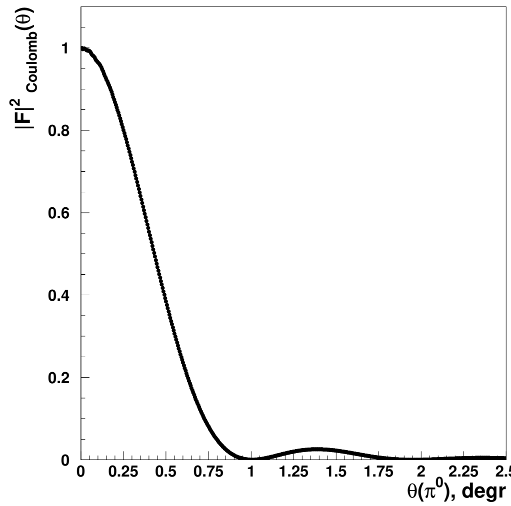

Figure 42: The square of the electromagnetic form factor for lead.

5.3 Physics Backgrounds

In this experiment, many physics processes with an energetic π^o in the final state can potentially contribute to the extracted yield of the π^o distributions and therefore create background in the cross section measurement. The photoproduction of ω's in the nuclear target is the main source of background because of its relatively large cross section and its consequent decay into π^o's through the $\omega \to \pi^o\gamma$ channel with a sizable branching ratio. The π^o from this decay channel may carry most of the initial photon energy and potentially contribute to the "signal" in this experiment. To estimate the background contributions from ω and ρ photoproduction, we have done an extensive Monte Carlo simulations based on the *GEANT3* package with a full description of the experimental setup. The cross sections for the elastic coherent and incoherent processes were taken from the experimental results published in the literature, as described in [70]. The results from these simulations for the angular distribution of background events from ω photoproduction on a carbon target, normalized to the experimental yields, are shown in figure 47. The background contribution from ρ photoproduction is about ten times less than from ω and is not shown in the plot. The 20% uncertainty corridor from the knowledge of the experimental cross sections is also shown. The effect of this background subtraction on the π^o decay width is demonstrated in figure 48. The fit of the experimental data with subtracted background has a 6% smaller χ^2 for the "Primakoff" region ($\theta = [0^o...0.5^o]$), and changes the extracted π^o decay width by 1.4% with an uncertainty of 0.24%. This quoted uncertainty in the decay width is a result of the errors on the experimental cross sections used for these background simulations.

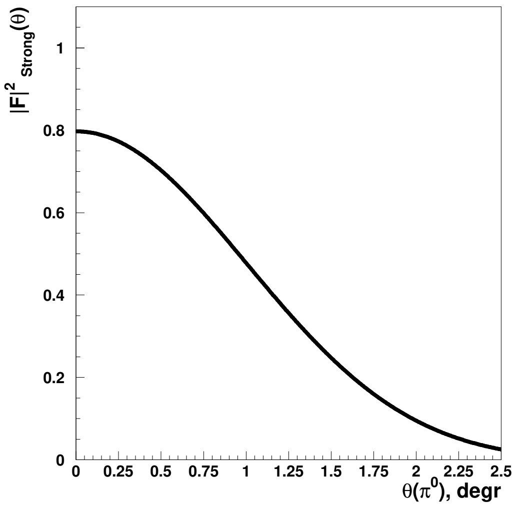

Figure 43: The square of the strong form factor $F_S(q)$ for carbon without photon shadowing $F_3 = 0$.

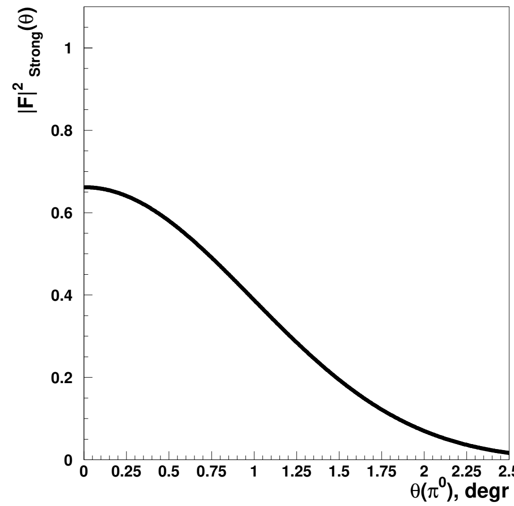

Figure 44: The square of the strong form factor $F_S(q)$ for carbon with photon shadowing $F_3 = 0$.

The experimental cross section measurements of the simulated processes have ∼20% uncertainties. To investigate the contributed systematic errors from these uncertainties, we have done a similar simulation with the cross sections increased and decreased by 20% (see figure 48). These 20% variation of the subtracted background causes a 0.24% variation of the extracted π^o width.

5.4 Determination of $\Gamma_{\pi^o\to\gamma\gamma}$: the *PrimEx* Preliminary Result

The experimental cross sections for the π^o forward photoproduction on two targets, described in the previous sections, were fitted to extract the π^o decay width with the following procedure: for each $\Delta\theta_\pi$ angular bin, the number of expected events $n_i(\theta_\pi)$ was calculated for each component of the cross section, described in the previous subsection by folding in the bremsstrahlung spectrum and the detector angular resolution and acceptance. Then the total number of expected events ($n(\theta_\pi)$=$n_{prim}(\theta_\pi)$+$n_{nucl.coh}(\theta_\pi)$+$n_{interf.}(\theta_\pi)$+ $n_{incoh.}(\theta_\pi)$) normalized to the photon flux and number of target nuclei in the experiment, were compared with the experimental yield distribution. Four parameters (the π^o decay width, the magnitude of nuclear coherent amplitude, the phase factor between these two coherent processes and the height of the nuclear incoherent cross section) were kept free to be optimized during the fit procedure. Since the Primakoff production is peaked in the extreme forward direction, the precision extraction of the π^o decay width is strongly dependent on the experimental resolutions in the production angle. Several different methods have been developed by the analysis groups to minimize this effect. An example of a fit to the experimental yields is shown in figure 49.

The combined average for the π^o decay width from the three analysis group is: $\Gamma_{\pi^o} = (7.93eV \pm 2.1\%(stat.) \pm 2.0\%(syst.)$ and is shown in figure 50 together with the previous

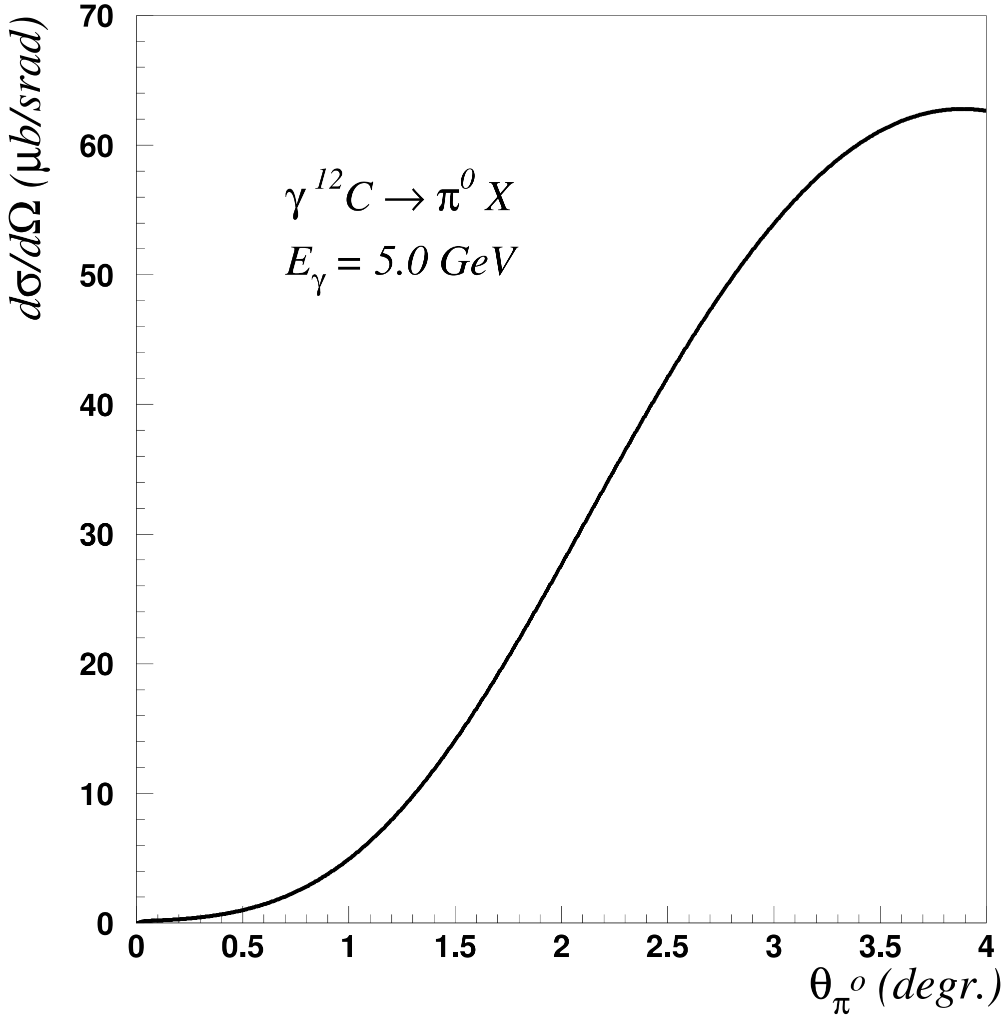

Figure 45: Incoherent cross section for carbon.

experimental results and the theory predictions. Within the experimental errors, our preliminary result is in good agreement with the theory predictions.

5.4.1 Experimental Uncertainties in the *PrimEx* Preliminary Result

We have analyzed a part of the total accumulated experimental data set from the Fall 2004 run. These runs were selected for the stability of the beam conditions and the HYCAL calorimeter as well as the entire experimental setup. To improve the statistical error in the extracted result it is possible to use more experimental data, but that would significantly add more uncertainty in the estimation of the final systematic errors. This is the major limitation to reducing the total experimental error on the extracted π^o decay width from the first *PrimEx* run. We have performed extensive Monte Carlo studies to determine all

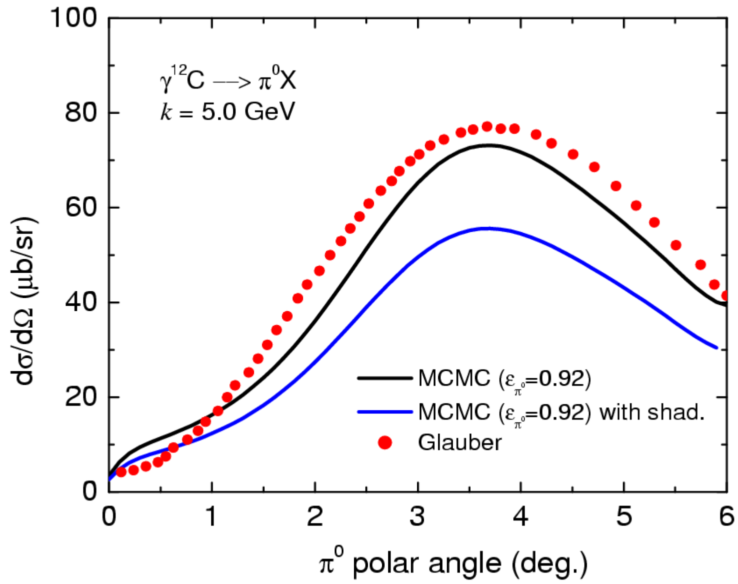

Figure 46: Comparison of calculations by Glauber and Cascade models on nuclear Incoherent (NI) cross section $\left(\frac{d\sigma}{d\Omega}\right)$ for π^0 photoproduction on carbon. The ε_{π^0} is for π^0 elasticity cut.

possible contributions to the total systematic error. Currently, the statistical error on our preliminary result is 2.1%. The relevant details are presented in three *PrimEx* Analysis Notes. The table below summarizes the major contributing items to the total systematic error.

photon flux	1.0%
target thickness (atoms/cm^2)	0.1%
background subtraction	1.0%
model error in π^o width extraction	1.0%
analysis cuts	0.5%
HYCAL response function	0.5%
beam energy and parameters	0.4%
π^o detection acceptance	0.3%
physics background	0.25%
Total	2.0%

The total error is estimated by adding the individual errors in quadrature and represents the combined average from the three analysis groups.

With this new proposal, we are requesting beam time for a follow up *PrimEx* run to get enough stable experimental data to provide 0.4% statistical errors for two nuclear targets,

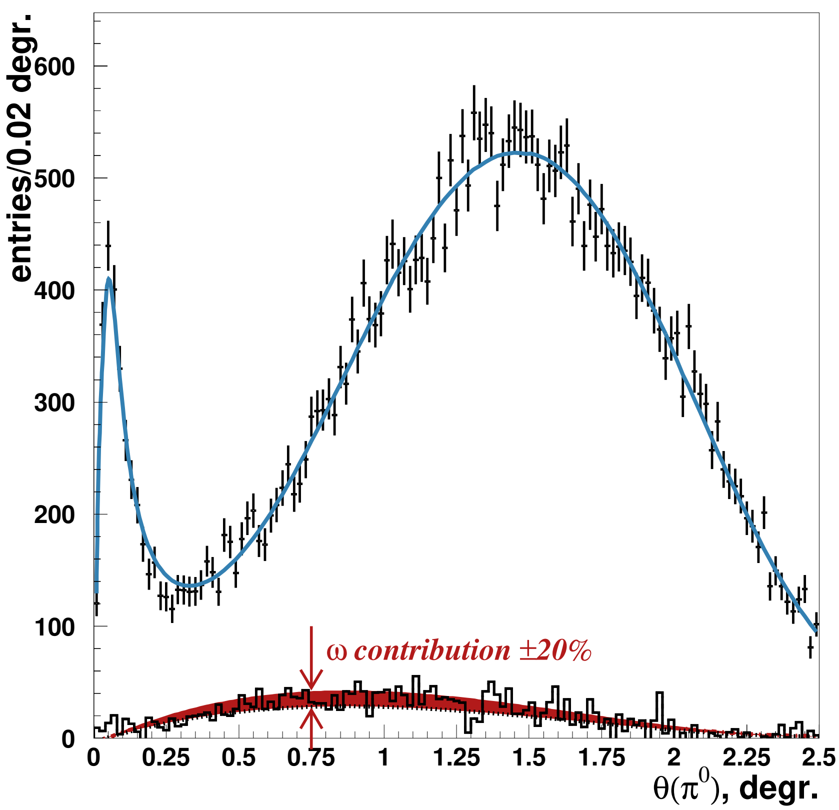

Figure 47: Distribution of simulated background from ω photoproduction normalized to the π^o experimental yield on a carbon target. The 20% uncertainty in the background is a result of the experimental cross sections used for these simulations.

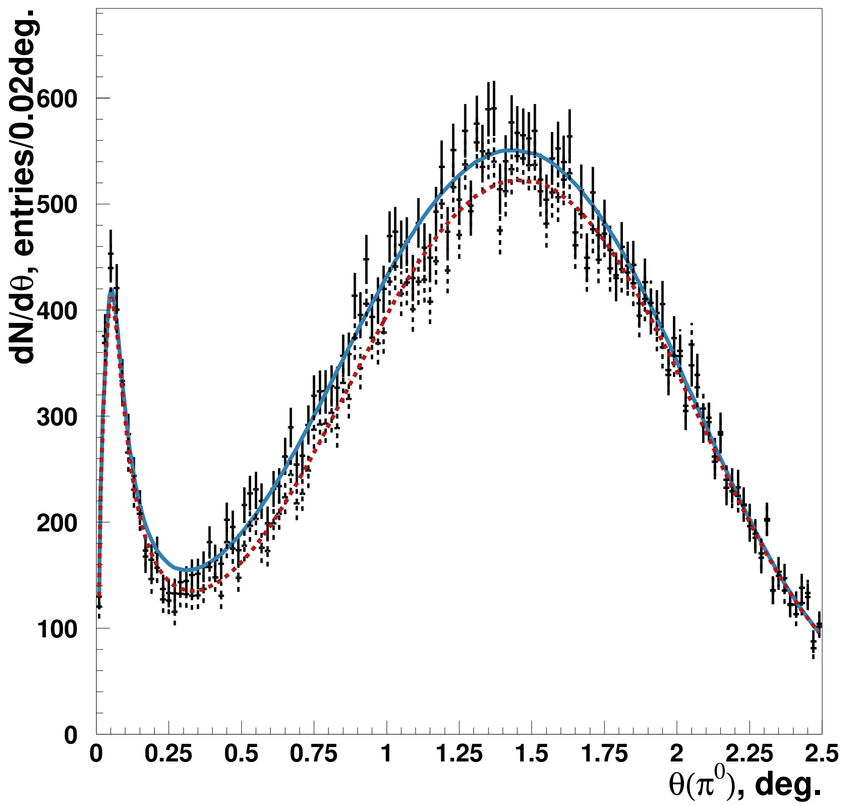

Figure 48: π^o yield vs. production angle with a fit applied. Solid histogram and line - before background subtraction. Dotted histogram and line - with subtracted background from ω and ρ photoproduction.

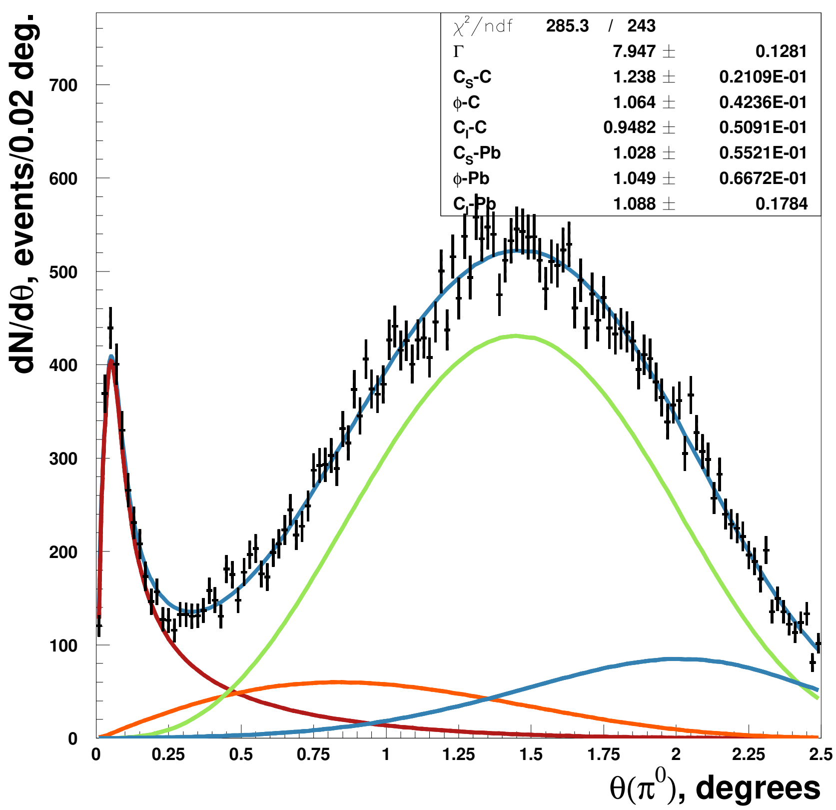

Figure 49: The result of the fit done by one of the analysis groups for the carbon target. Contributions from all four processes: the Primakoff; nuclear coherent; nuclear incoherent and interference term are shown according to their fit parameters.

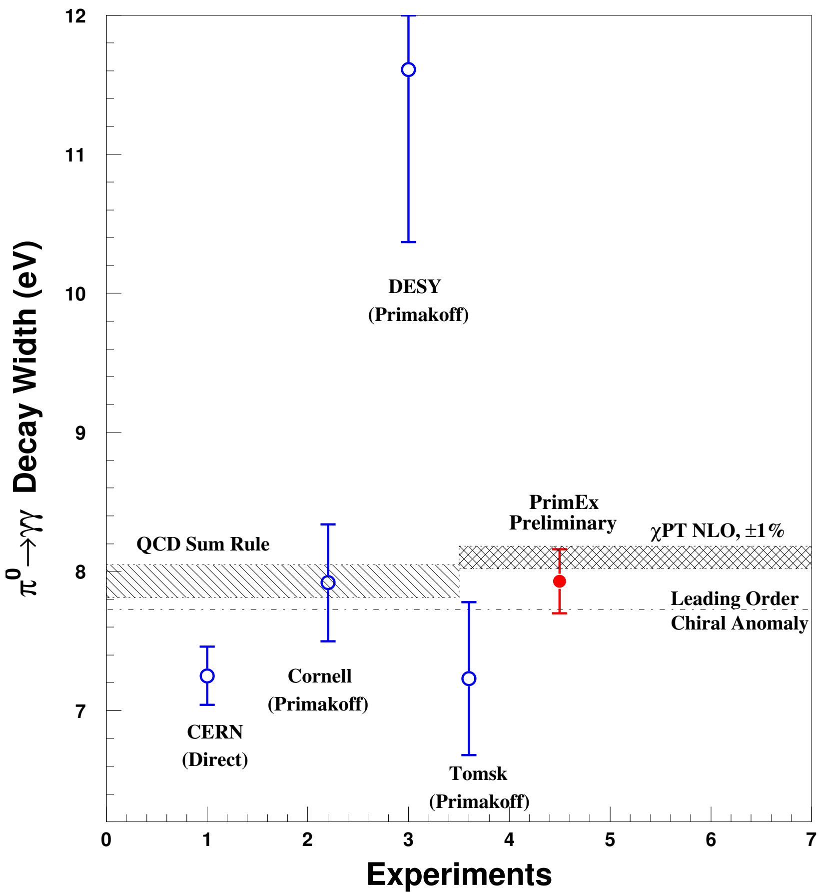

Figure 50: Preliminary result for the π^o decay width from the carbon data of the PrimEx experiment together with the previous experiments and the theoretical predictions.

^{12}C and ^{208}Pb. The new, high statistics data set with the periodically executed empty target and calibration (Compton and pair production) runs will improve the systematic errors on all major contributing items in this table, including the background subtraction and analysis cuts. As described below, in the photon flux control we have already reached our projected 1.0% experimental error, which is verified by the sub-percent level agreement of the extracted pair production and the Compton cross sections with the QED calculations. We have also succeeded in determining target thickness uncertainties to a level better than 0.1%. In conclusion, with a new run of 28 days of beam time, we believe that our collaboration will have the ability to extract the π^o decay width with the projected 1.4% total experimental error.

5.5 Results of high precision calibration experiments

5.5.1 The absolute cross section for pair production

The *PrimEx* experimental setup provides a unique opportunity to verify the luminosity normalization procedure (including both photon flux and target thickness) by measuring the absolute cross-section for a well known electromagnetic process, namely (e^+e^-) pair-production, without any additional hardware development.

Cross-section calculations for the photo-production of e^+e^- pairs on ^{12}C at photon energies of a few GeV and small momentum transfer $|\vec{Q}| \sim 10keV$ relevant for the *PrimEx* experiment were provided by A. Korchin[31]. A summary of different contributions included in the cross-section calculation are listed below in decreasing order of significance:

- The Bethe-Heitler mechanism for pair production on the nucleus. To account for screening effects due to atomic electrons, two models of the atomic form factor, Thomas-Fermi-Moliere and Hartree-Fock, were considered. The Coulomb distortion effects have been included according to the work of Bethe and Maximon. (This contribution to the e^+e^- cross section is $\sim 80\%$).

- Pair production on atomic electrons, taking into account the excitation of all atomic states and correlation effects due to the presence of other electrons and the nucleus. (Contribution of $\sim 20\%$.)

- QED radiative corrections (of order α/π with respect to the dominant contributions): (i) virtual-photon loops and (ii), the real-photon process $\gamma + A \rightarrow e^+ + e^- + A + \gamma'$. (Contribution of $\sim 1 - 2\%$).

- Nuclear incoherent contribution – quasi-elastic, or quasi-free processes on the proton $\gamma + p \rightarrow e^+ + e^- + A + p$. (Contribution of $< 0.05\%$).

- Nuclear coherent contribution, *i.e.* virtual Compton Scattering, a two-step process – $\gamma + A \rightarrow \gamma^* + A \rightarrow e^+ + e^- + A$ (Contribution of $\sim 10^{-5}\%$).

As an example, figure 51 shows the calculated energy distribution of electrons produced by $5.46 GeV$ photons on a ^{12}C target. The calculations, based on three different models of atomic form factors, are shown: Hartree-Fock (HF), Thomas-Fermi-Moliere (TFM) and a simpler monopole approximation introduced by Tsai. As one can see from the figure, the cross section slightly decreases compared to TFM if the HF form factor is used. The difference between the cross-section based on the Hartree-Fock atomic form factor and the one based on the Thomas-Fermi-Moliere model is of the order $< 1\%$, which is indicative of the accuracy of the calculations.

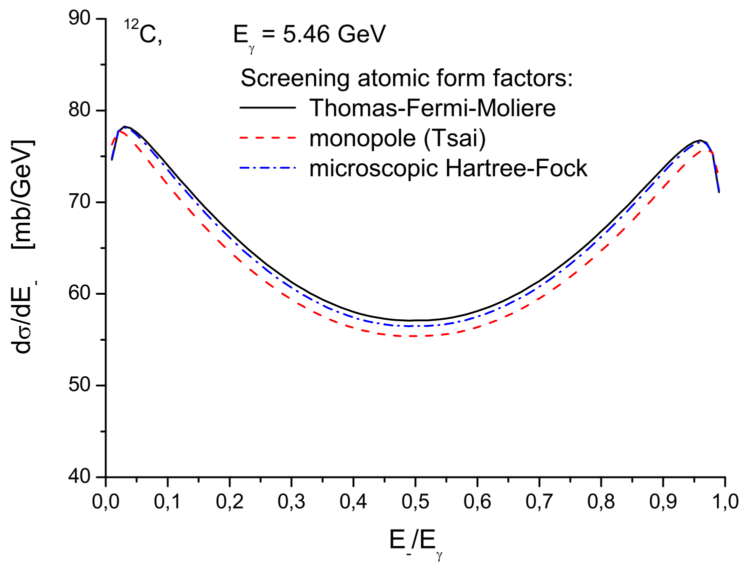

Figure 51: Calculated energy spectrum of electrons in pair production on ^{12}C for $5.46 GeV$ photons.

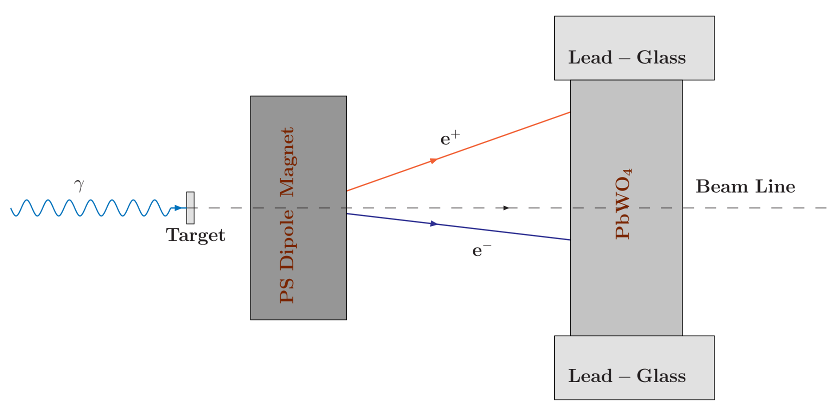

Figure 52: Schematic of a pair-production event as seen by the *PrimEx* experimental setup (top view).

A schematic of a pair-production event, as seen by the *PrimEx* experimental setup downstream of the tagger, is shown in Figure 52. For the pair production cross-section measurements, both the incident photon energy and timing information were determined by the tagger. The strength of the magnetic field of the pair spectrometer dipole was lowered (to $\sim$ 0.220 and 0.293 $Tesla \times m$), and the electron-positron pairs were swept into the calorimeter where the energy and position of the each particle was measured. The trigger signal, a coincidence between Tagger MOR and HYCAL, provides timing information of the $e^+ - e^-$ pair.

Figure 53 shows the distribution of x and y coordinates and the energy-position correlation for events with incident photon energy in the range $5.145 - 5.201 GeV$ after a timing cut of $(-5\sigma, +8\sigma)$. The negative x coordinates correspond to positrons and the positive x coordinates represent electrons.

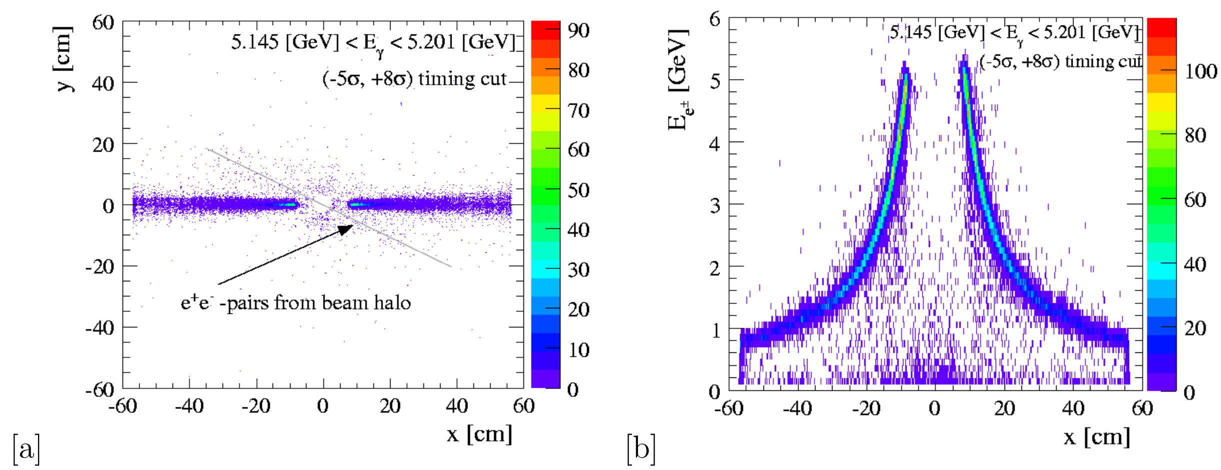

Figure 53: (a) Distribution of x and y coordinates of clusters reconstructed in HYCAL. (b) Correlation of energy and deflection in the magnetic field for clusters reconstructed in HYCAL.

In part (a) of Figure 53, one can see a ring of "Compton" photons around the central opening of the HYCAL and a faint line with a negative slope due to pair production generated by the halo of the beam hitting the photon beam collimator upstream of the experimental target. The electrons and positrons created by the halo on the collimator are first deflected in the field of the permanent magnet in the vertical direction and then by the pair spectrometer dipole magnet in horizontal direction creating the sloped line.

To eliminate the e^+e^- pairs created by the beam halo and most of the Compton photons, a cut on the y coordinate $|y| < 5cm$ was used. Pair production data were taken with various settings of pair spectrometer dipole. For the highest field setting of $\sim$ 0.293 $Tesla \times m$, momenta of $1.6GeV$ and less correspond to deflections in the field of the dipole of $\sim 37.17cm$ or more, *i.e.* deflections into the outer Lead-Glass layer of the calorimeter. A cut of $E_{e^\pm} > 1.695GeV$ on the lepton energy limits the analysis to the inner, high resolution lead-tungstate portion of the HYCAL (which extends out to $\pm 35.275cm$) and enables comparison of data from runs with different field settings.

Compton electrons take most of the energy in the kinematic regime of the *PrimEx* experiment, thus a cut $E_{e^\pm} > 1.2GeV$ would also eliminate a large amount ($\sim$ 59.9%) of Compton photons, some of which would otherwise be reconstructed in the lead-tungstate part of the calorimeter. It is worth noting that the distributions of x and y coordinates for Compton photons are identical due to the azimuthal symmetry of Compton scattering. To subtract the background due to Compton scattering under the electron arm, a *GEANT4* simulation involving detector resolution was performed and the resulting distribution was subtracted from the data.

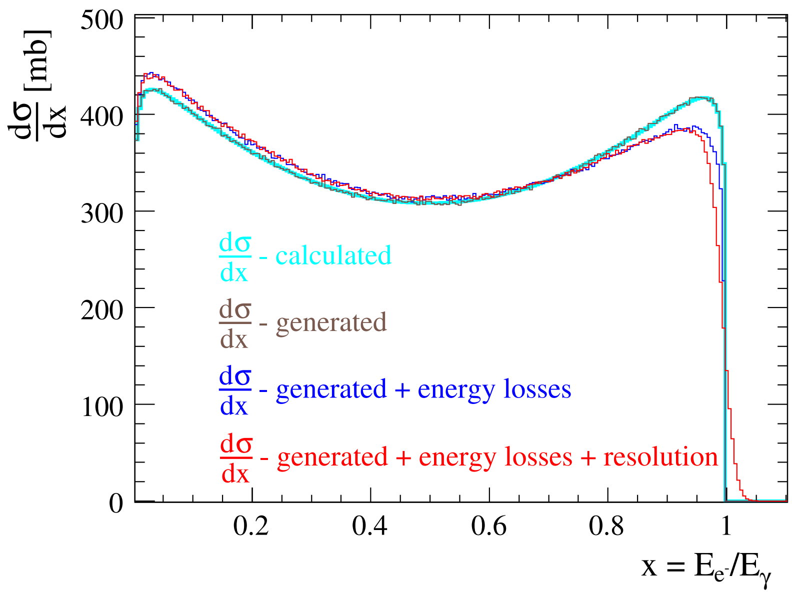

Figure 54: Absolute cross-section for pair-production differential in fraction of energy of photon taken by the electron for $E_\gamma = 4.91 - 5.46 GeV$. The effect of energy losses in the target and the helium bag is also shown as a blue histogram.

The effects of secondary interactions (multiple scattering, Compton scattering, bremsstrahlung, *etc.*) in the target and experimental setup were simulated in *GEANT4* by generating events according to theory and propagating them through the experimental setup. As seen in figure 54, for electrons or positrons with energy fraction $0.75 < x < 1.0$ the percent difference between calculated cross section and the one modified by energy losses and detector resolution is large. Hence, for this region of x one could expect a significant discrepancy between experimental cross sections and theory (modified by energy losses and resolution) due to the uncertainty of the *GEANT4* calculation of the energy losses. To minimize the potential systematic errors, it is preferable to compare the experiment and theory for $0.4 < x < 0.75$ where the effect of the energy losses on the cross section is less than 5%. Figures 55, 56, 57, and 58 show the comparison between experimentally determined cross sections for electrons and positrons and theoretical calculations, the latter convoluted with detector resolution and acceptances.

Table 1 lists the theoretical and experimental pair production cross sections for two separate runs integrated between x_{min} and x_{max}, where x is the fraction of energy of the incident photon taken by the electron or positron ($x = E_{e^\pm}/E_\gamma$). Statistical errors for the integrated cross section (integrated over the x range indicated) are 0.30% and 0.44% for runs 5141 and 5142, respectively. As can be seen, the experimentally obtained cross section for $0.4 < x < 0.755$ is in excellent agreement with theory in each case. This is strong confirmation of the validity of the luminosity determination in the 2004 *PrimEx* run.

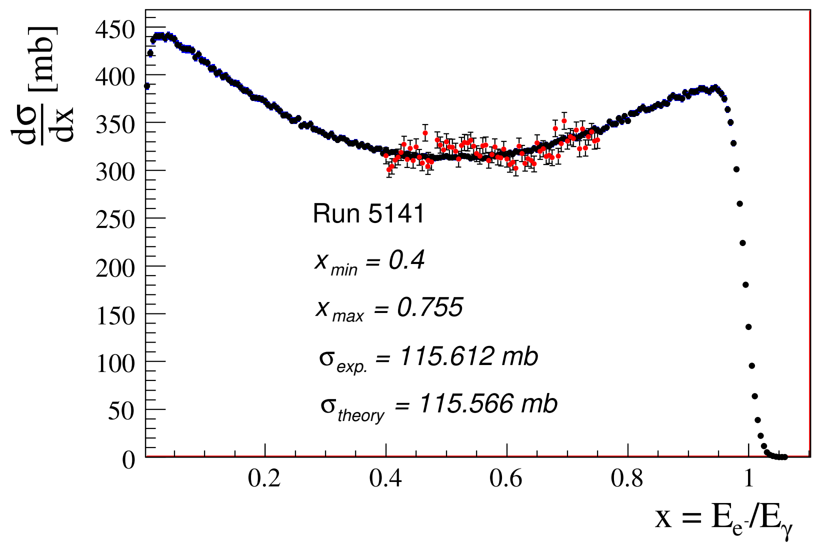

Figure 55: Differential single arm cross section on electron arm, run 5141, compared with theory.

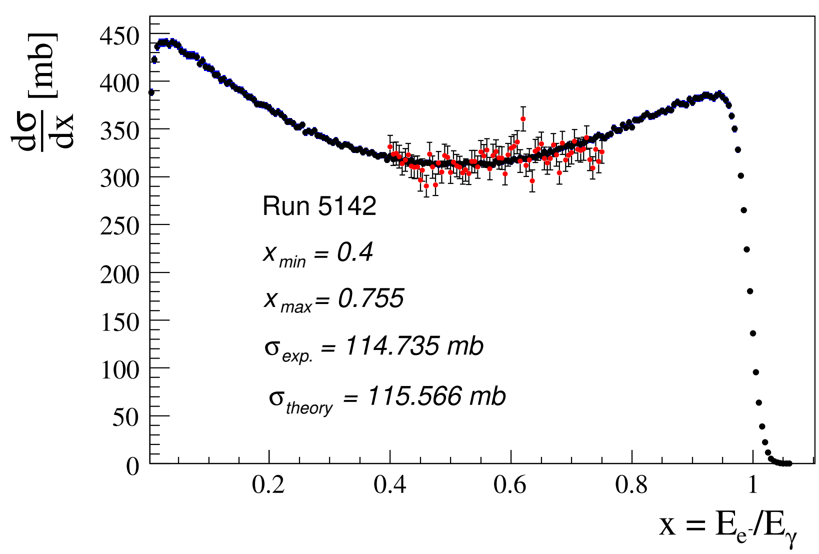

Figure 56: Differential single arm cross section on electron arm, run 5142, compared with theory.

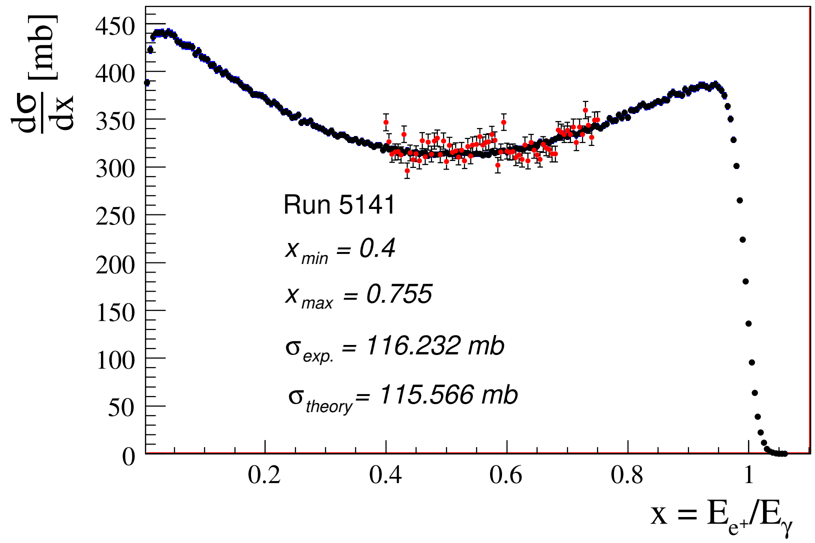

Figure 57: Differential single arm cross section on positron arm, run 5141, compared with theory.

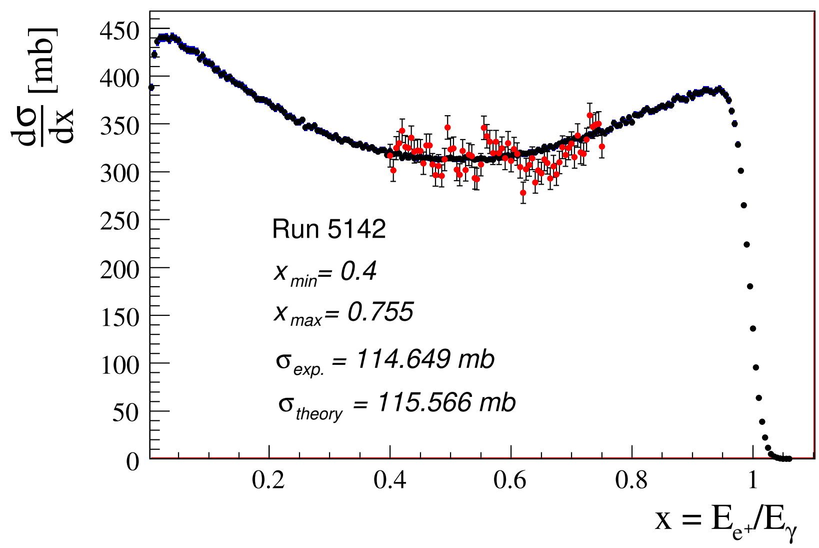

Figure 58: Differential single arm cross section on positron arm, run 5142, compared with theory.

5.5.2 Absolute cross section for electron Compton scattering

In addition to pair production, we used atomic electron Compton scattering as a tool to control systematic errors on absolute cross section measurements and to monitor the stability of the experimental setup. Whereas pair production is primarily a check of the luminosity, electron Compton scattering provides a more comprehensive check of the overall setup, as

Table 1: Pair production cross-section integrated between x_{min} and x_{max}.

Run Number	x_{min}	x_{max}	$\sigma_{experiment}[mb]$	$\sigma_{theory}[mb]$	particle	$(1 - \sigma_{experiment}/\sigma_{theory})[\%]$
5141	0.4	0.755	115.612	115.566	electrons	-0.04
5142	0.4	0.755	114.735	115.566	electrons	0.7
5141	0.4	0.755	116.232	115.566	positrons	-0.6
5142	0.4	0.755	114.649	115.566	positrons	0.8

its kinematics are in many ways similar to those involved in detecting neutral pions via $\pi^o \to \gamma\gamma$.

The scattering of photons by free electrons $\gamma + e \to \gamma' + e'$ is one of the simplest and most basic quantum-electrodynamic processes that is experimentally accessible. The lowest order Compton scattering diagrams were first calculated by Klein and Nishina in 1929 [33], and by Tamm in 1930 [34]. There are two types of corrections to the basic Klein-Nishina formula which must be considered when studying Compton scattering at energies above 0.1 GeV. These are radiative corrections, and double Compton scattering contributions. The interference between the basic first order single Compton scattering amplitude and the radiative and double Compton scattering amplitudes have been studied extensively in the literature [35]-[37], [38],[39], and the errors on the theoretical calculations are less than 1%. The total Compton cross section and forward cross section on ^{12}C with radiative and double Compton corrections, calculated by different numerical methods[41][42], are compared as shown in figures 59 and 60. In the case of the total cross section they are also compared to the National Institute of Standards and Technology (*NIST*) values. They are in good agreement within 0.5%. As such, Compton scattering provides an excellent means to control the systematic errors of the *PrimEx* experiment, including the photon flux, target thickness, and HYCAL calorimeter detection efficiency.

The Compton data were taken periodically, once per week, during our experiment in 2004. The pair spectrometer magnet was off in order to detect both scattered photons and electrons in the HYCAL, and a lower beam intensity was used due to the higher Compton cross section compared with the π^o production. The rest of the setup was the same as that of the π^o production runs. Detection of a Compton event is shown schematically in figure 61. The energy and positions of the scattered photon and electron were measured in the calorimeter. In conjunction with the beam energy which was determined by the photon tagger, the full kinematics of the Compton events were determined, thus facilitating the event selection.

Three groups in the *PrimEx* collaboration analyzed the Compton data independently. The results of different analysis are in good agreement within their error bars. The preliminary result from one of the groups will be described in detail below.

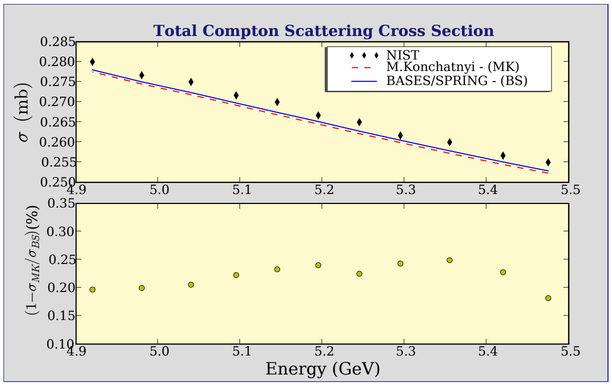

Figure 59: Comparison of theoretical calculations on Compton total cross with radiative corrections by different methods. The bottom plot shows the deviation between two calculations by different numerical methods (MK[41] and BS[42]) is less than 0.3%.

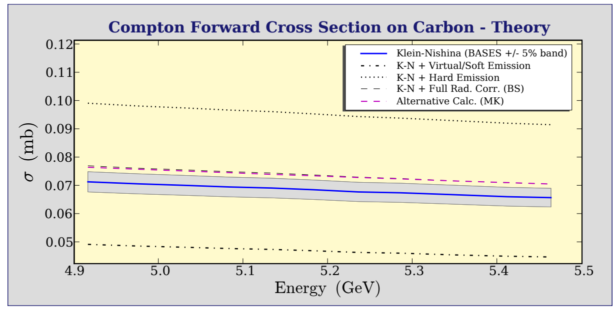

Figure 60: Radiated Klein-Nishina cross section integrated over HYCAL solid angle.

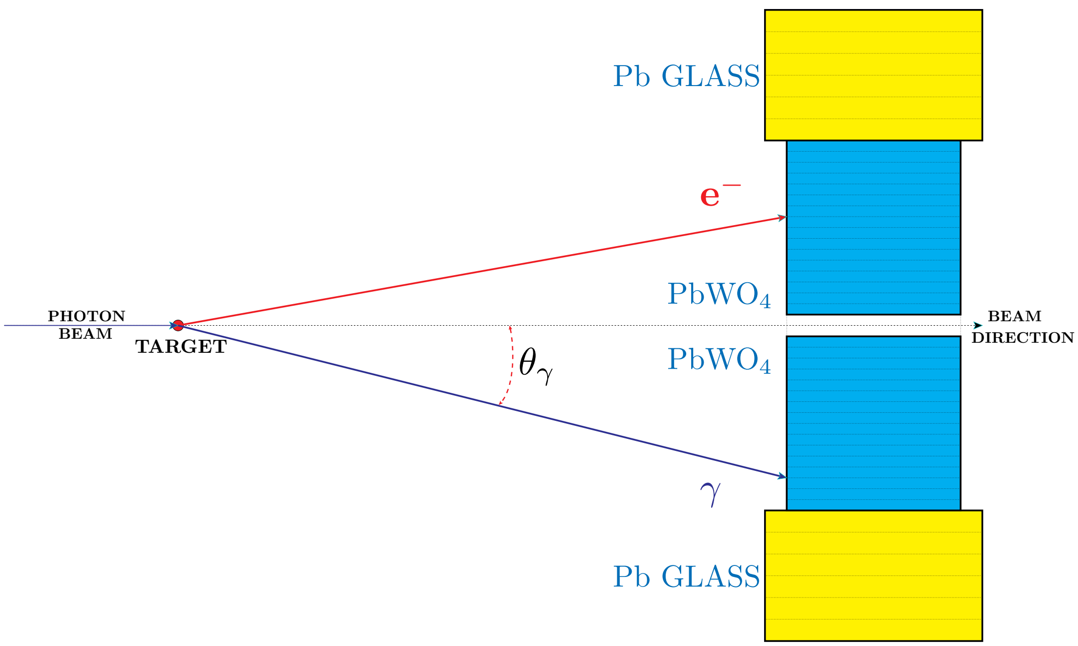

Figure 61: Detection of a single Compton event in HYCAL.

Data Selection

The Compton data set in this analysis was collected on a 5% radiation length ^{12}C target with incident photon beam energies of 4.85 - 5.45 GeV. To select Compton events, the data were processed in two stages: (1) initial selection, where loose cuts were applied on the raw data, and (2) final events selection, where an optimized set of cuts based 4-momentum conservation or spatial signatures of the Compton process stemming from its elastic nature, were applied on the initial selected data.

The cuts in stage one included:

- $|\mathrm{T_{TAG}} - \mathrm{T_{HyCal}}| < 20$ ns, the coincidence time between the photon tagger and HYCAL total sum,
- Total energy sum on HYCAL $\sum_i E_i > 3.5$ GeV,
- $E_i > 0.5$ GeV, where $i = \mathrm{e}',\ \gamma'$

The cuts in the stage two included:

- $|\mathrm{T_{TAG}} - \mathrm{T_{HyCal}}| < 5.35$ ns, - 5σ coincident timing cut, see figure 62,
- $\Delta\phi < 34^o$ - coplanarity of e', andγ' cut, see figure 62,
- $4.154\ \mathrm{cm}\ <\ |\mathrm{x_i}|\ <\ 33.232\ \mathrm{cm}$ - HYCAL fiducial cut, $i = \mathrm{e}',\ \gamma'$,
- $4.150\ \mathrm{cm}\ <\ |\mathrm{y_i}|\ <\ 33.200\ \mathrm{cm}$ - HYCAL fiducial cut, $i = \mathrm{e}',\ \gamma'$,
- $-0.6\ \mathrm{GeV} < \mathrm{E_{TAG}} - \mathrm{E_{CALC}} < 1.2$ GeV - momentum conservation cut,
- $625\ \mathrm{cm} < \mathrm{z} < 825$ cm - interaction vertex cut,
- $R_{min} > 16.0$ cm - minimal separation of scattering e and γ on HYCAL,
- *criss-cross* cut aimed at removing the pair production background.

where z is the distance from the target to HYCAL calculated by using two cluster coordinates on the calorimeter; E_{CALC} is the incident photon energy determined from the scattering particles' energy and position measured by HYCAL. A *GEANT* Monte Carlo simulation indicates that the pair production background shown in figure 63 mainly comes from the collimator located upstream of the *PrimEx* target. The permanent magnet located between the collimator and the target bent the trajectories of electrons and positrons to HYCAL. Without the presence of the magnetic field, the pairs would have proceeded undetected through the central opening in the calorimeter. About 25% of the events were lost due to the cut to eliminate the pair production contamination, so that about one quarter of HYCAL was inaccessible for the calibration by the Compton process. We plan to solve this problem in the future run by increasing the magnetic field of the sweeping magnet downstream of the collimator, preferably with an active magnet. The last two cuts are shown in the figure 63.

Yield Extraction and Result

To extract the final Compton yield, the elasticity distribution ($\Delta E = E_0 - (E'_\gamma + E_e)$, where E_0, E'_γ and E_e are measured energy of incident photon, scattered photon and electron) of the events, selected by using the cuts described above, were fitted with the signal and background distributions for every $\sim 1\%$ energy bin defined by one photon tagger T-counter. The signal distribution is generated by Monte Carlo simulation based on the well known theoretical angular distribution of Compton scattering including the radiative correction

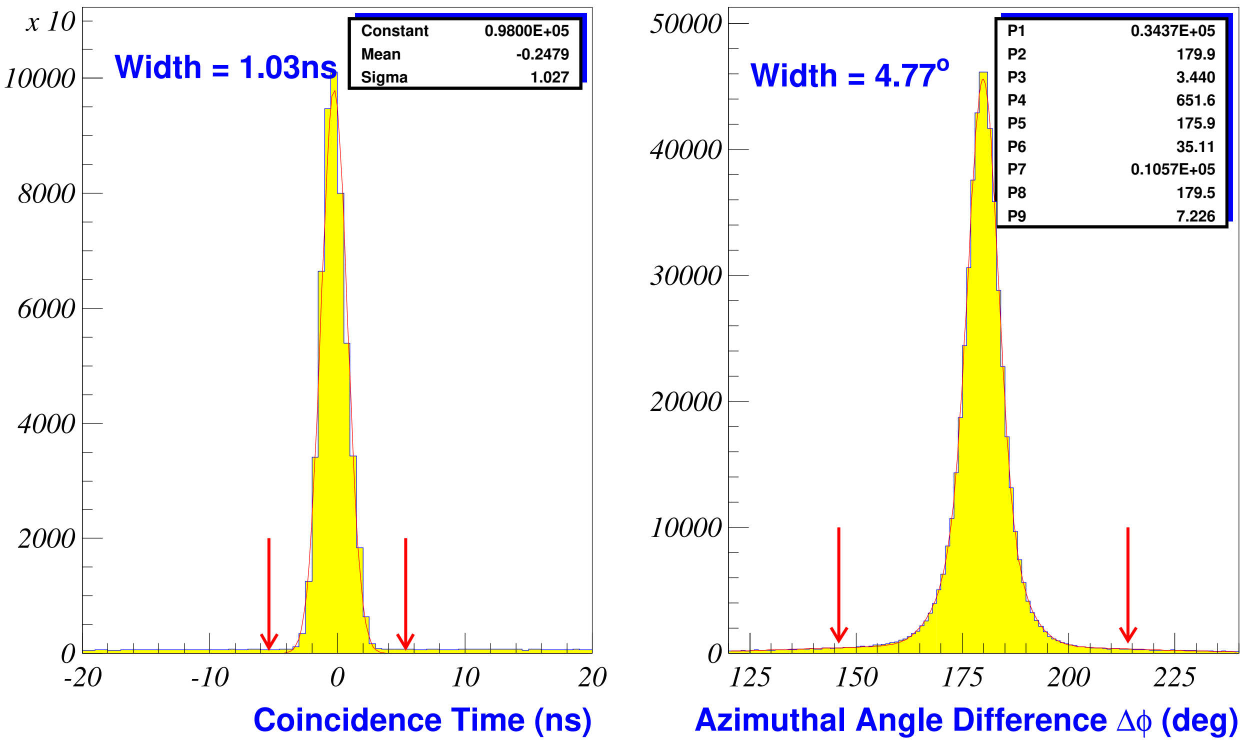

Figure 62: (Left) Time difference between a hit in the tagger and HYCAL total sum signal, (Right) Difference of the photon and the electron azimuthal angles - coplanarity.

and double Compton contribution, detector resolution and acceptance. The same Monte Carlo program was also used in the π^0 data analysis. The shape of the background is modeled with the accidental events selected from the data using the same cuts described above except for timing, which was changed to $|\mathrm{T_{TAG}} - \mathrm{T_{HyCal}}| > 5.35$ ns. The signal and background distributions were then fit to the data using the maximum likelihood method, as shown in figure 64. This two-parameter fit maximizes the likelihood function by finding the best overall strengths for the signal and background. Then the yield is obtained by the number of events in the data after background subtraction.

From the extracted yield, combined with luminosity and detector acceptance information, the preliminary results for the total Compton cross section and average differential cross section in the forward direction over the HYCAL acceptance were obtained, as shown in Figures 65 and 66. Both the measured total cross section and the forward differential cross section consistently agree with theory predictions with a 14% confidence level.

To determine the Compton cross section with the highest possible precision, various systematic studies were performed. They include the following contributions:

- incident photon flux,
- target compostion and thickness,
- coincidence timing,

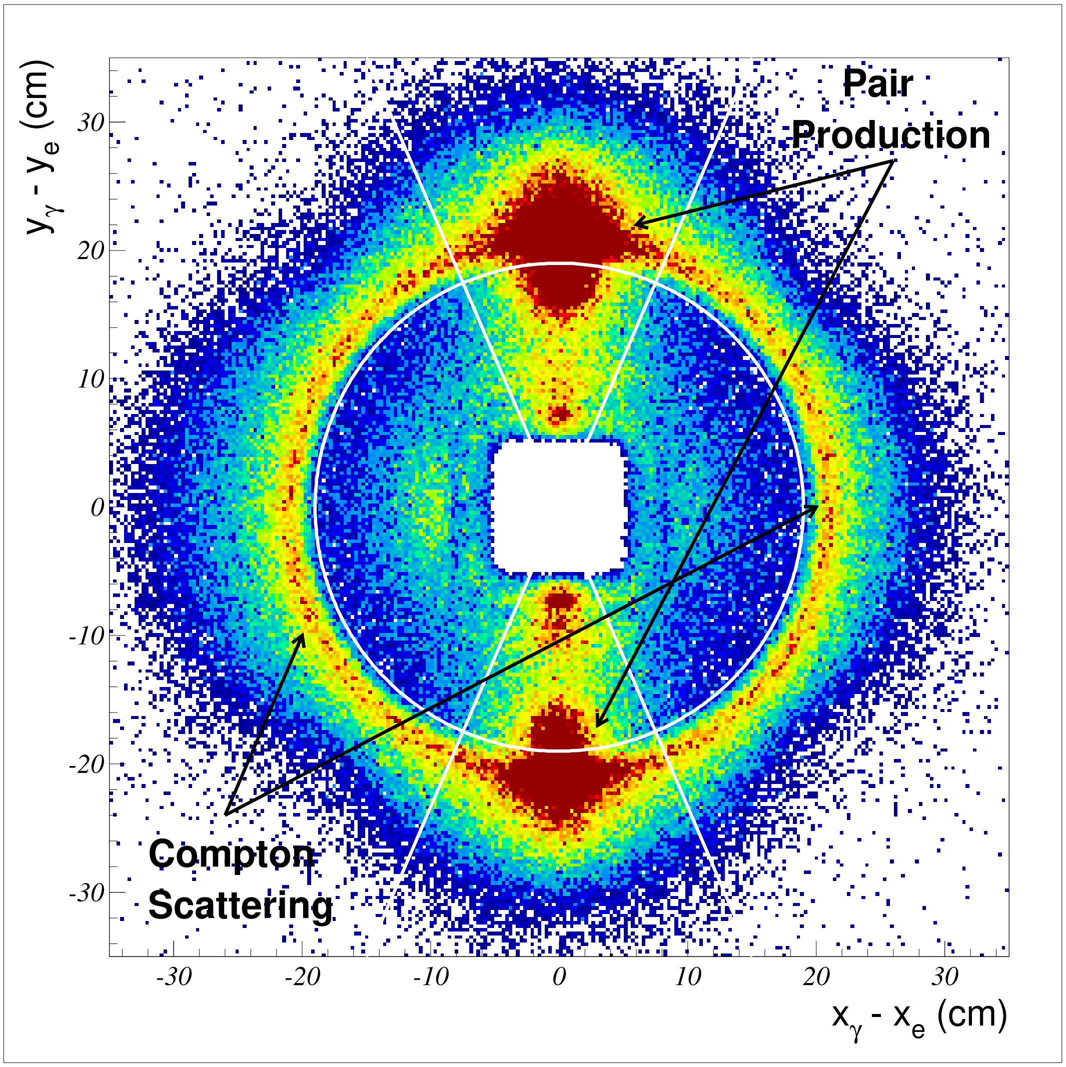

Figure 63: Event selection. Shown in the plot are two geometric cuts: (1) minimum separation cut - white circle, (2) *criss-cross* cut, white lines, that aims at removing pair production background events.

- coplanarity,
- the dependence of the cross section on radiative tail cut,
- geometric cuts stability,
- signal-background separation,
- yield fit stability.

The result of the systematic studies for each T-counter ($\sim$ 1% energy resolution) is summarized in Table 2. In order to minimize the influence of statistics on systematic uncertainties, error analysis on combined two adjacent T-counters was also performed. The results of this study are summarized in the Table 3. The average systematic error on the cross

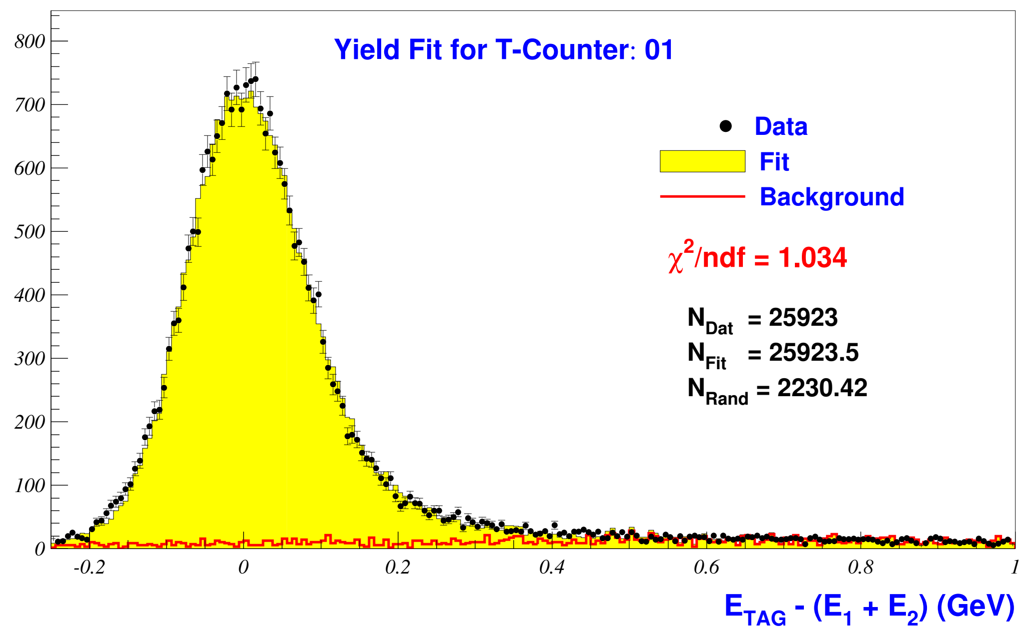

Figure 64: Yield fit, with background shown in red, for T counter 1.

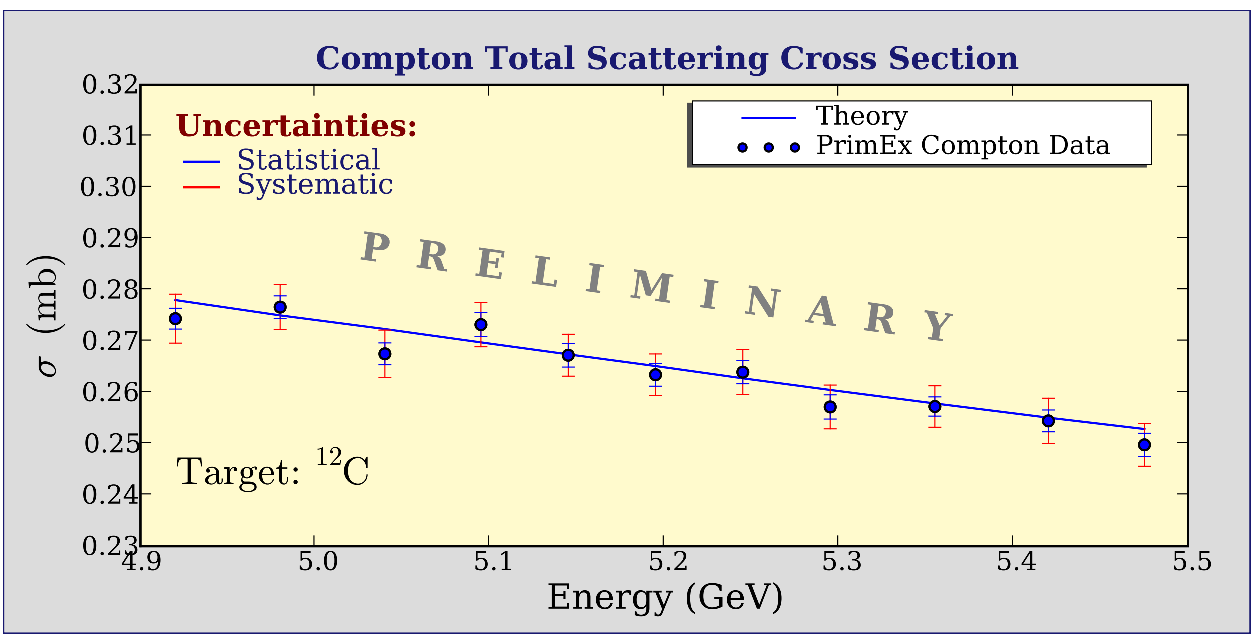

Figure 65: Total Compton cross section result. The statistical and systematic errors are shown in blue and red respectively. The energy resolution for each point is about 1%.

section measurement for 2% energy bin is about 1.28%, the statistical error is 0.59%, and the total error is about 1.41%. The two biggest contributors to the systematic uncertainty are background subtraction and the geometric acceptance. The first is related to the way

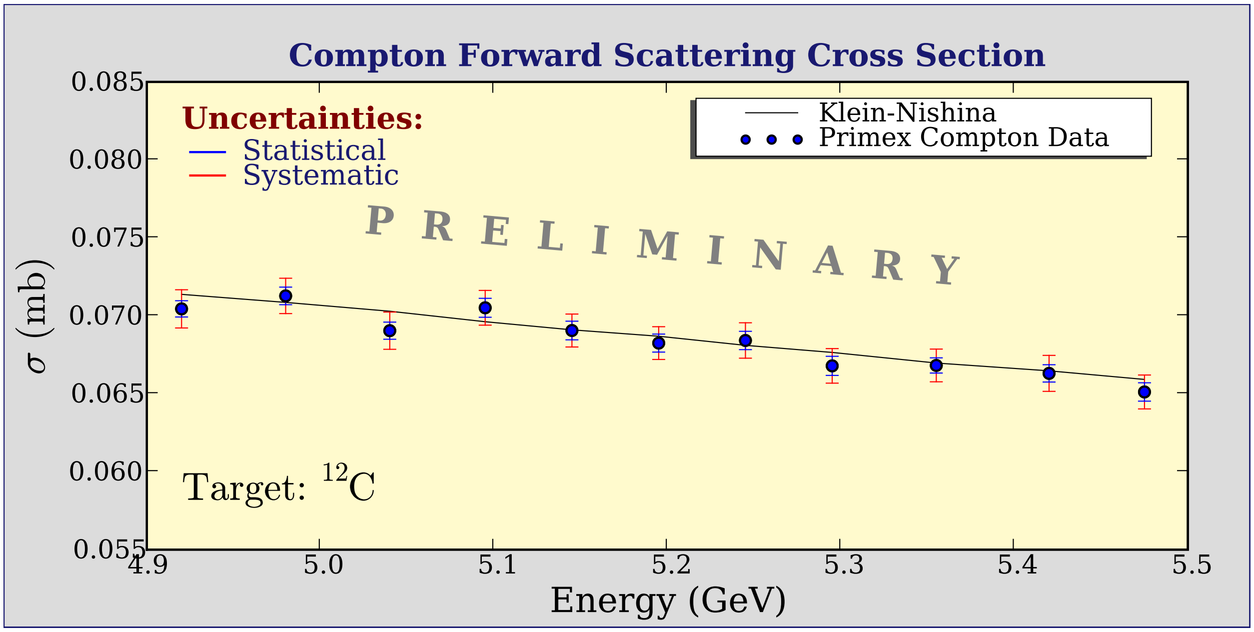

Figure 66: The forward Compton cross section averaged over the HYCAL acceptance. The statistical and systematic errors are shown in blue and red respectively.

the background is modeled. This error could be further reduced when all the background contributions are carefully simulated. The second one is associated with the beam direction, in turn, affecting the position and angles of the scattered photons and electrons.

TCtr	Flux	Tgt	ΔT_{coin}	$\Delta\phi$	Rad. Tail	Geom.	Sg/Bg	Fit	**Syst.**	**Stat.**	**Total**
1	1.0	0.05	0.09	0.17	0.001	0.62	0.78	0.075	**1.43**	**0.90**	**1.72**
2	1.0	0.05	0.01	0.18	0.010	0.68	1.01	0.075	**1.59**	**0.84**	**1.83**
3	1.0	0.05	0.01	0.13	0.095	0.53	0.60	0.075	**1.29**	**0.73**	**1.55**
4	1.0	0.05	0.03	0.17	0.340	0.31	0.74	0.075	**1.35**	**0.92**	**1.65**
5	1.0	0.05	0.13	0.18	0.033	0.71	0.52	0.075	**1.36**	**0.86**	**1.64**
6	1.0	0.05	0.08	0.17	0.310	0.30	0.40	0.075	**1.18**	**0.85**	**1.50**
7	1.0	0.05	0.03	0.19	0.120	0.60	0.24	0.075	**1.22**	**0.87**	**1.53**
8	1.0	0.05	0.03	0.17	0.130	0.65	0.41	0.075	**1.28**	**0.86**	**1.58**
9	1.0	0.05	0.08	0.16	0.230	0.35	1.05	0.075	**1.52**	**0.80**	**1.77**
10	1.0	0.05	0.03	0.21	0.027	0.56	0.60	0.075	**1.31**	**0.79**	**1.59**
11	1.0	0.05	0.06	0.21	0.160	0.42	1.07	0.075	**1.55**	**0.74**	**1.77**

Table 2: Experimental uncertainties for each T-counter. All values are in %. Statistical error accounts for yield and photon flux fluctuations.

Experimental Stability

In addition, measuring the Compton cross section periodically allows one to monitor the stability of the experiment. Figure 67 shows the measured total Compton cross section *versus* run number. This comparison reveals the departure of the experimental cross section from the theoretical value for the points around the run number 5150 and later. This could

TCtr	Flux	Tgt	ΔT_{coin}	$\Delta\phi$	Rad. Tail	Geom.	Sg/Bg	Fit	**Syst.**	**Stat.**	**Total**
1–2	1.0	0.05	0.03	0.065	0.098	0.91	0.46	0.063	**1.44**	**0.61**	**1.56**
3–4	1.0	0.05	0.03	0.065	0.098	0.68	0.42	0.063	**1.29**	**0.57**	**1.41**
5–6	1.0	0.05	0.03	0.065	0.098	0.46	0.40	0.063	**1.18**	**0.60**	**1.32**
7–8	1.0	0.05	0.03	0.065	0.098	0.33	0.37	0.063	**1.13**	**0.61**	**1.28**
10–11	1.0	0.05	0.03	0.065	0.098	0.85	0.36	0.063	**1.37**	**0.54**	**1.47**

Table 3: Experimental uncertainties for combined two T-counters. All values are in %. Statistical error accounts for yield and photon flux fluctuations.

be related to a drop in relative tagging ratios for that time period, which was identified by the pair production luminosity monitoring technique described in this proposal.

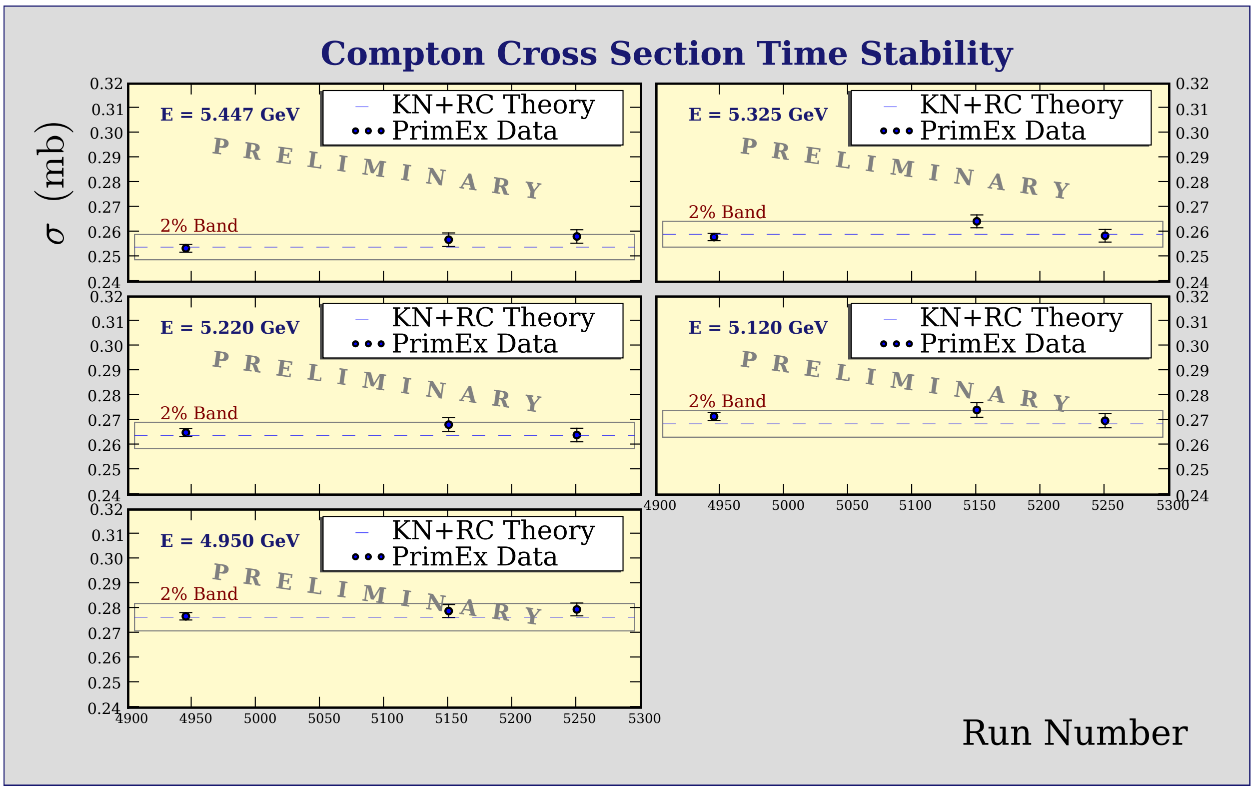

Figure 67: Measured total Compton cross sections change over the run numbers. The error accounts for the statistical fluctuations in both yield and photon flux.

Conclusion

In conclusion, the total cross section and the forward differential cross section for Compton scattering in the 4.85 - 5.45 GeV energy range were measured with the *PrimEx* setup. They are in excellent agreement with theory predictions with a 14% confidence level. For each data point with an energy resolution of 2% defined by two T-counters, an average systematic error of 1.28%, a statistical error of 0.59%, and an average total error of 1.41% (see Table 3) have been reached. The time stability of the Compton cross section measurement was also performed. It reveled a 2% stability during the entire *PrimEx* running period. Since Compton scattering in this energy range mimics the π^0 lifetime experiment, the precision obtained from the Compton measurement demonstrates that the *PrimEx* experimental setup has the capability to measure the absolute cross section π^o production with a $\sim 1.5\%$ accuracy.

6 Count Rate Estimates and Beam Time

Based on our experience and results from the first *PrimEx* experimental run, for this run we have decided to get high statistical data sets for two targets only: one for a low Z nucleus (^{12}C), and one for a high Z nucleus (^{208}Pb). The selection of these targets is also motivated by the fact that we already have well developed and understood theoretical models for the pion photoproduction processes in these nuclei. In addition, the accuracies in the target thickness and density measurements for these two targets are currently at the sub-percent level.

For the count rate estimates, we use the experimental cross sections extracted from our first *PrimEx* run. We plan to run with a 6 GeV electron beam and intensity of 100 nA, which will produce a bremsstrahlung photon beam with the Q=6.2×10^7 eq.photons/sec intensity on the 10^{-4} X_0 tagger radiator. For the accepted energy interval $E_\gamma = (0.85 - 0.95)E_o$ the rate will be 7×10^6 photons per second.

The total π^o rate for the 5% radiation length ^{208}Pb target, integrated for the $\theta_\pi = 0° - 2°$ angular interval, and for the beam parameters listed above is expected to be:

$$Rate = N_\gamma \times N_{nuclei} \times \Delta\sigma \times E_{eff} \tag{27}$$

$$\approx 7 \cdot 10^6 \times 9.2 \cdot 10^{20} \times 2.16 \cdot 10^{-2} \cdot 10^{-27} \times 0.7 \approx 0.1 events/sec \approx 8700 events/day. \tag{28}$$

Therefore, to accumulate a data sample with statistics of 0.4% for the integrated energy interval, we request 6 days of beam time for the lead target. Similar estimations for the carbon target show that for the same 0.4% statistical accuracy we will need 7 days of beam time.

To check the systematic errors as well as the stability of the experimental setup during the relatively long period of run time, we plan to measure the Compton cross section with a statistical error of 0.5% or less. As shown in this proposal, this will provide ~1.5% total error in the Compton cross section, which is appropriate for the goal of the desired pion lifetime extraction accuracy. The Compton runs will be done once a week with the minimum pion run configuration change. For these measurements, the beam intensity will be reduced to ~10nA with the pair spectrometer dipole turned off to detect the recoil electrons in the calorimeter. To accumulate a Compton data sample with statistics of 0.5% per energy bin, nine hours of beam time will be needed per Compton run. For a total of six such high statistics Compton runs, we will need $\sim$ 3 days of beam time including the time needed for the configuration change. The e^+e^- pair production cross section also will be measured periodically, once per day or after each major change in the beam or accelerator tune, to control the uncertainty in the photon flux during the entire run period. The beam time for these activities is estimated to be one day in total.

A summary of the requested beam time, specified for each major activity, is shown in the table below:

^{12}C target	7 days
^{208}Pb target	6 days
Compton and e^+e^- pair prod.	4 days
Empty target runs	2 days
Tagger efficiency, TAC runs	1 day
Setup calibration and checkout	6 days
HYCAL configuration change and alignment before data collection	2 days
Total	28 days

To reduce the uncertainties on the background subtraction, we plan to make runs with the same conditions as the physics runs but with the target removed from the beam line – the so called empty target runs. This will be done for each physics measurements (π^o, Compton and pair production). A total of two accumulated days will be required for these measurements. To control the photon flux in the experiment at the required 1% level, we will periodically measure the tagging efficency with the Total Absorption Counter. This will require a minimum configuration change, and we estimate total of one day for these measurements. Based on our experience from the first run, we request a total of six days for the experimental setup calibration and complete checkout with the beam. The major part of this time will be used for the HYCAL calorimeter precision calibration, optimization, and checkout of the trigger organization for the calorimeter. Special measurements will be done for a better understanding of the HYCAL trigger efficiency. This item is currently one of the largest contributions to the total uncertainty on the extracted pion decay width (0.5%). Finally, after the calibration and checkout, the configuration of the calorimeter will be changed from the transporter to the run configuration with the consequent 0.7 mm accuracy in alignment in the plane perpendicular to the photon beam. We estimate using two days of beam time for these activities based on our previous experience.

In conclusion, we are requesting a total of 13 days of tagged photon beam time for the physics production data taking: 7 days for ^{12}C and 6 days for ^{208}Pb, In addition, we estimate 4 days of beam time to perform calibration and control experiments (Compton and pair production), 2 days of empty target runs, 1 day for the calibration and control of the tagger efficiency, 6 days of experimental setup calibration and checkout with beam and an estimated 2 days for the HYCAL configuration change and alignments. Therefore, we request a total of 28 days of beam time for the precision measurement of the $\pi^o \to \gamma\gamma$ decay width with the 0.4% statistical errors for each physics target.

7 Improvements for an Upcoming Run

During our first *PrimEx* run, the Collaboration gained a lot of experience on how to setup and calibrate the experimental equipment efficiently, and how to control the systematic errors. There are several improvements planned for a future run:

1. We plan to place a small calorimeter behind the HYCAL during the gain calibration run. This will allow us directly to measure the HYCAL detection efficiency.

2. Improve the performance of the HYCAL gain monitoring system by adding more magnetic insulation on the reference detectors' PMTs and possibly replacing the existing PMTs with less magnetic field sensitive photodetectors. In addition, we will repair the contacts of the optical cables to the front face of HYCAL modules in order to maintain long term stability.

3. A permanent magnet in the beam line located between the collimator and the physics target was designed to sweep away the pair production background produced from the collimator due to the beam halo. It worked effectively during the π^o production run when the pair spectrometer magnet downstream of the target was on. As pointed out earlier, however, it delivered those pair production leptons as backgrounds to the HYCAL during the Compton runs when the pair spectrometer magnet was off. As a result, about one quarter of HYCAL was inaccessible for the calibration by Compton scattering. We plan to solve this problem in future runs by increasing the magnetic field of this magnet, and preferably replacing it with an active magnet.

4. We will reduce the prescale factor for the clock trigger in Compton runs in order to increase the statistics for the photon flux measurement.

5. We will take more empty target runs for the background study.

6. We will mount the photon beam position monitor independent of the total absorption counter so that the photon beam position will be monitored during normalization runs.

8 Summary

We are requesting the continued support of the Jefferson Laboratory management in our efforts to perform a high precision test of the axial anomaly in quantum chromodynamics. The fundamental importance of this experiment is evidenced by the fact that, in anticipation of the results, three independent theoretical calculations of the decay rate have been performed. The calculations, based on both next-to-leading order chiral theory and QCD sum rules, have indicated an increase in the width as compared to the leading order. As a fundamental quantity in QCD, we argue that it is of utmost importance to measure it at a level which puts these state of the art theoretical calculations to the test. The *PrimEx* Collaboration is at present the only collaboration in a position to perform these measurements.

The Collaboration has designed, developed and constructed a multi-million dollar experimental setup which was commissioned during the first *PrimEx* run in 2004. We have verified the quality of the data obtained and the validity of our analysis procedures by measuring the cross sections for well known QED processes, pair production and electron Compton scattering, with a systematic error of less than1.3% . The preliminary result from this data set, $\Gamma_{\pi^o} = (7.93eV \pm 2.1\%(stat.) \pm 2.0\%(syst.)$, has been obtained with an error of 3%. The analysis result indicates that the Collaboration has the capability to control the systematic error at the required level. In order to reach our final goal of 1.4% precision, we are requesting 28 days of 6 GeV beam time in Hall B. This will be one of very few fundamental tests of QCD that can be performed in the low energy region.

References

[1] See *e.g.* Dynamics of the Standard Model, J.F. Donoghue, E. Golowich, and B.R. Holstein, Cambridge University Press (1992).

[2] J.S. Bell and R. Jaciw, Nuovo Cimento 60A, 47 (1969). S.L. Adler, Phys. Rev. 177, 2426 (1969).

[3] R.M. Barnett *et al.*, Review of Particle Physics, Phys. Rev. D54,1 (1996).

[4] H. Leutwyler, Phys. Lett. **B378** (1996) 313 and hep-ph/9602255.

[5] J. Bijnens, A. Bramon and F. Cornet, Phys. Rev. Lett. 61 (1988) 1453.

[6] J.F. Donoghue, B.R. Holstein, Y.C.R. Lin, Phys. Rev. Lett., vol. 55, (1985), 2766; J.F. Donoghue, B. Wyler, Nucl. Phys., B316, (1989), 289.

[7] B. Moussallam, Phys. Rev. **D51** (1995) 4939.

[8] J. L. Goity, A. M. Bernstein, J. F. Donoghue, and B. R. Holstein, manuscript in preparation; J. L. Goity, talk at Baryons 2002.

[9] B. Ananthanarayan and B. Moussallam, preprint hep-ph/0205232.

[10] B.L. Ioffe and A.G. Oganesian, Phys. Lett. B647, (2007) 389.

[11] H.W. Atherton *et al.*, Phys. Lett., vol. 158B, no. 1, (1985), 81.

[12] G. Bellettini et al., Il Nuovo Cimento, vol. 66, no. 1, (1970), 243.

[13] V.I. Kryshkin *et al.*, Sov. Phys. JETP, vol. 30, no. 6, (1970),1037.

[14] A. Browman et al., Phys. Rev. Letts., vol. 33, no. 23, (1974), 1400

[15] A. Browman *et al.*, Phys. Rev. Lett., vol. 32(1974) 1067.

[16] H. Leutwyler, private communication.

[17] Compact Muon Solenoid Technical Proposal, CERN/LHCC 94-38, LHCC/P1, (1994).

[18] K. Mengel *et al.* IEEE Trans. Nucl. Sci. **45**, 681-685 (1998).

[19] R.Y. Zhu, et. al. IEEE Transactions on Nuclear Science, v.45, no.3,(1998).

[20] A. Gasparian, Calorimetry in Particle Physics, 208-214, Pasadena 2002.

[21] A.V. Dolgopolov, *et al.* Preprint IHEP, IHEP-98-25, Protvino (1998)

[22] G. von Dardel *et al.*, Phys. Lett., vol. 4, no. 1, (1963), 51.

[23] D.A. Williams *et al.*, Phys. Rev. D, vol. 38, no. 5, (1988), 1365.

[24] H. Primakoff, Phys. Rev. 81, 899 (1951).

[25] A.M. Bernstein, Nucl. Phys. A623 (1997) 178c.

[26] G. Bellettini *et al.*, Il Nuovo Cimento, vol. 40, no. 4, (1965), 1139.

[27] Available at the *PrimEx* web site: http://www.jlab.org/primex/

[28] K. Mork and H. Olsen, Phys. Rev., vol 140, number 6B, (1965), B1661.

[29] *PrimEx* Conceptual Design Report, 2000 (http://www.jlab.org/primex/).

[30] R.Y. Zhu, *et al.* IEEE Trans. Nucl. Sci. **45**, 686-691 (1998).

[31] A. Korchin, Kharkov Institute of Physics and Technology, Kharkov 61108, Ukraine, private communication, 2007.

[32] S. Danagoulian, The Light Monitoring System, PrimEx Note 53.

[33] O. Klein and Y. Nishina, *Z. Phys.*, **52**, 853 (1929).

[34] I. Tamm, *Z. Phys.*, **62**, 545 (1930).

[35] I.M. Brown and R.P. Feynaman, *Phys. Rev.*, **85**, 231(1952).

[36] Till B. Anders, *Nucl. Phys.*, **87**, 721 (1967).

[37] K.J. Mork, *Phys. Rev.*, **A4**, 917 (1971).

[38] F. Mfandl and T.H.R. Skyrme, *Proc. R. Soc. London*, **A215**, 497 (1952).

[39] M. Ram and P.Y. Wang, *Phys. Rev. Lett.*, **26**, 476 (1971); *ibid.* **26**, 1210(E)(1971).

[40] A. H. Compton, Bull. Natl. Res. Counc. (U.S) 20, 19 (1922); *Phys. Rev.*, **21**, 483 (1923).

[41] Mykhailo Konchatnyi, PrimEx Note 37, http://www.jlab.org/primex/.

[42] A. Tkabladze, M. Konchatnyi, and Y. Prok, PrimEx Note 42, http://www.jlab.org/primex/.

[43] G. Morpurgo, Nuovo Cimento 31, 569 (1964)

[44] G. Fäldt, Nucl. Phys. , B43, 591 (1972)

[45] S.Gevorkyan, A.Gasparian, L.Gan, jlab.org/Primex/ Notes 45 , 2007

[46] E. Offermann et al., Phys.Rev. C44, 1096 (1991)

[47] C.Jager, H.Vries, C.Vries, Atomic Data and Nucl.Data Tables 60, 177 (1995)

[48] pdg.lbl.gov/2006/

[49] V.Glaser and R.Ferrell, Phys.Rev. 121,886 (1961)

[50] S.Gevorkyan, I.Larin, A.Gasparian, L.Gan jlab.org/Primex/ Notes 46 , 2007

[51] A.Browman et al., Phys.Rev.Lett. 33, 1400 (1974)

[52] T.Bauer, R.Spital, D.Yennie, F. Pipkin, Rev. of Mod. Phys. 50, 261 (1978)

[53] K.Gottfried and D. Yennie, Phys.Rev. 182, 1595 (1969)

[54] W.Meyer et al., Phys. Rev. Lett. 28, 1344 (1972)

[55] G. Bellettini et al., Nuovo Cim.LXVI A, 243 (1970)

[56] S.Gevorkyan, A.Gasparian, L.Gan, I.Larin, jlab.org/Primex/ Notes 50, 2007

[57] C. Engelbrecht, Phys.Rev. 133, B988 (1964)

[58] M.Braunschweig et al., Phys. Lett. 26B, 405 (1968)

[59] G.Fäldt, Nucl.Phys. B62, 86 (1973)

[60] C. A. Engelbrecht, Phys. Rev. **133**, B988 (1964).

[61] T. E. Rodrigues, J. D. T. Arruda-Neto, A. Deppman, V. P. Likhachev, J. Mesa, C. Garcia, K. Shtejer, G. Silva, S. B. Duarte and O. A. P. Tavares, Phys. Rev. C **69**, 064611 (2004).

[62] T. E. Rodrigues, J. D. T. Arruda-Neto, J. Mesa, C. Garcia, K. Shtejer, D. Dale and I. Nakagawa, Phys. Rev. C **71**, 051603(**R**) (2005).

[63] T. E. Rodrigues, J. D. T. Arruda-Neto, J. Mesa, C. Garcia, K. Shtejer, D. Dale and I. Nakagawa, Braz. J. of Phys., vol. **36**, no. 4b, 1366 (2006).

[64] T. E. Rodrigues, *Incoherent* π^0 *photoproduction in the PrimEx kinematics via the MCMC intranuclear cascade model*, PrimEx Note # 52 (2007).

[65] M. Braunschweig, W. Braunschweig, D. Husmann, K. Lübelsmeyer and D. Schmitz, Nucl. Phys. B **20**, 191 (1970).

[66] R. L. Anderson *et al.*, Phys. Rev. D **4**, 1937 (1971).

[67] W. T. Meyer *et al.*, Phys. Rev. Lett. **28**, 1344 (1972).

[68] L. Lapikás *et al.*, Phys. Rev. C **61**, 064325 (2000).

[69] T. H. Bauer, R. D. Spital, and D. R. Yennie, Rev. Mod. Phys. **50**, 261 (1978).

[70] I.Larin, A. Gasparian, L. Gan, S Gevorgyan, Background contribution from ω photoproduction in the experiment Primex, PrimEx Note 44, 2007.

9 Appendix I: Previous Experiments

9.1 The direct method

A direct measurement of the π^o lifetime can be made by observation of the decay distance between the production and decay points. This has proven difficult because of the high spatial resolution which is required due to the short lifetime, $\tau \simeq 10^{-16}$ sec. To be able to discern distinct production and decay points, one must take advantage of relativistic time dilation to have the pion survive long enough in the laboratory frame. Additionally, good knowledge of the energy distribution of the produced pions is necessary in order to extract the lifetime via this method.

The most recent result employed direct method was carried out at the CERN SPS in 1985 (shown in figure 1). In this experiment, a 450 GeV/c proton impinged upon two tungsten foils whose separation was variable. The first foil served as the π^o production target, and the second foil converted the π^o decay photons to electron-positron pairs, and the positrons were subsequently detected. By measuring the positron rates for three different foil spacings ranging from 5 to 250μm, the authors were able to determine the lifetime. The dominant systematic errors arise from uncertainties in the π^o spectrum which was not measured but was assumed to be the arithmetic mean of the π^+ and π^- spectra. In addition, corrections had to be made for the Dalitz decay of the π^o's, conversion of the photons in the π^o production target, prompt positron and photon production, and positrons from the decay of η's. A pion lifetime of $\tau_{\pi^o} = (0.897 \pm 0.022 \pm 0.017) \times 10^{-16}$ seconds was reported[11], corresponding to a width of $\Gamma_{\pi^o} = (7.34 \pm 0.18 \pm 0.11)$ eV.

It is interesting to note that this experiment gives a result which is smaller than the leading order chiral anomaly prediction[1, 2]. Furthermore, with the latest calculations based on both next-to-leading order chiral theory and QCD sum rules described above, the discrepancy between this measurement and theory widens to more than three standard deviations. The experiment proposed here will directly address this discrepancy.

9.2 Measurements using $\gamma\gamma$ collisions

The π^o width has been measured using electron-positron collisions at DESY via $e^+e^- \rightarrow e^+e^-\gamma^*\gamma^* \rightarrow e^+e^-\pi^o \rightarrow e^+e^-\gamma\gamma$ [23]. The incident leptons are scattered at very small angles and are not detected in the final state. In so doing, they radiate quasi-real photons that couple to the π^o which is subsequently identified in an invariant $\gamma\gamma$ mass spectrum. The photons were detected using the Crystal Ball detector which consists of a large array of NaI(Tl) crystals providing 93% solid angle coverage. Contributions to the systematic error included luminosity normalization, detector efficiencies, cosmic ray rejection, and beam-gas collisions. The latter effect arises from the production of π^o's via the interaction of the leptons with the residual gas in the beam pipe. The resulting width obtained was $\Gamma_{\pi^o} = (7.7 \pm 0.5 \pm 0.5)$ eV, very close to the prediction of the anomaly but with a relatively large error. The value obtained in this experiment is the same as the Particle Data Book average but was not included in this average[3].

9.3 Measurements using the Primakoff effect

The Primakoff effect, *i.e.* photopion production from the Coulomb field of a nucleus[24], has been used in a number of experiments to study the π^o lifetime [14, 12, 13, 26]. The production of π^o's in the Coulomb field of a nucleus by real photons is essentially the inverse of the decay $\pi^o \to \gamma\gamma$, and the cross section for this process thus provides a measure of the π^o lifetime.

Using bremsstrahlung beams of energy 4.4 GeV and 6.6 GeV at Cornell, Browman *et al.*[14] measured the Primakoff cross sections on several nuclei, and obtained a total decay width of $\Gamma_{\pi^o} = (8.02 \pm 0.42)$ eV. However, as was pointed out in [25, 23], the quoted error does not have any contribution from uncertainties in the luminosity or detection efficiency (see table 1 of [14]), and is an underestimate. An analogous measurement of the η width[15] using the Primakoff effect employing a very similar setup and analysis procedure is not in agreement with other experiments.

The other two Primakoff measurements shown in figure 1 were performed with bremsstrahlung beams of 1.5 and 2.0 GeV at DESY[12] and 1.1 GeV at Tomsk[13]. From figure 1 it can be seen that the DESY measurement is high compared to the theoretical prediction and the Particle Data Book average. Although both of these measurements have relatively large errors they were included in the Particle Data Book average[3]. An older Primakoff experiment performed with 0.95 and 1.0 GeV bremsstrahlung beams at Frascati[26] has not been included in the Particle Data Book average and is not shown in figure 1.

In view of the strong interest in the subject, the dispersion of the previous results, and the recent availability of high intensity, high energy tagged photon beams, a high precision, state-of-the-art measurement of the π^o lifetime is needed. In past several years, PrimEx collaboration has developed an experimental setup combining existing Hall B tagged photon facility at TJNAF with a newly developed a state-of-the-art, high resolution electromagnetic colorimeter. It will enable a measurement which will offer three distinct advantages over previous measurements involving bremsstrahlung beams: (1) the quasi-monochromatic nature of the tagged beam will enable a clean kinematical separation of the Primakoff mechanism from various background processes, (2) the tagging technique will enable significantly better control of systematic errors associated with the photon flux normalization, and (3) high resolution and high efficiency electromagnetic calorimeter will enable precise measurements on the invariance mass and production angle of the π^0's. The first PrimEx experimental data set was collected in Hall B in fall 2004. The preliminary result is $\Gamma(\pi^0 \rightarrow \gamma\gamma) = 7.93 eV + -2.1\%(stat) + -2.0\%(sys)$ eV. More beam time is requested in this proposal to reach our final goal of $\sim 1.4\%$ precision.

10 Appendix II: Systematic Effects Relating to Photon Flux Determination

10.1 Effects of incident electron beam intensity on absolute tagging ratios

Due to rate limitations of the TAC, the absolute tagging ratios can be measured only at beam intensities which are $\sim 10^3$ times lower than the intensity of a regular production run. It is important to demonstrate that the tagging efficiencies obtained at beam intensities of $\sim 80 pAmps$ are valid when applied to the data collected at the high beam intensities of about 80 to 130 $nAmps$. To investigate this, during our running period in Fall of 2004 we had normalization runs with various beam intensities $(40 - 120 pAmps)$.

Figure 68 (top) shows the absolute tagging ratios as a function of T-counter number measured at different beam intensities. An artificial shift was introduced on the horizontal axis in order to be able to distinguish the different measurements. As a result, one has 11 groups of 4 points (one group per T-counter). The weighted average was calculated for each of the 11 groups. Figure 68 (bottom) shows the percent deviation of each measurement from the mean value for the relevant group. No significant systematic dependence of tagging ratios on the incident beam intensity was detected when varying the beam intensity from $40 pAmps$ to $120 pAmps$.

10.2 Effects of collimator size

A decision was made for *PrimEx* to run with very loose collimation of the bremsstrahlung photon beam to cut out the beam halo. Together with careful monitoring of the beam position, collimation should increase the stability of the luminosity by keeping the photon beam focused at one spot on the target and thus reducing the effects of possible non uniformity of the target thickness.

Two different sizes of copper collimators were available for this purpose. In Figure 69 (top) the relative tagging ratios are plotted *versus* T-counter ID for data taken with two different collimators. For reference purposes, a result with no collimation is also plotted. For these measurements, the statistical error on each point is on the order of 0.15%. As can be seen from Figure 69 (bottom), the $12.7 mm$ collimator cuts out $\sim 1\%$ of the photon beam and $8.6 mm$ collimator cuts out $\sim 4\%$ of the photon beam.

10.3 Effects of collimator position misalignment

Figure 70 shows the position of the collimator on its ladder *versus* run number. The entire running period can be divided up into two groups of runs – group 1) with run numbers from 4100 to 4295 with collimator at $7.075 in$ and group 2) with run numbers from 4502 to 5447

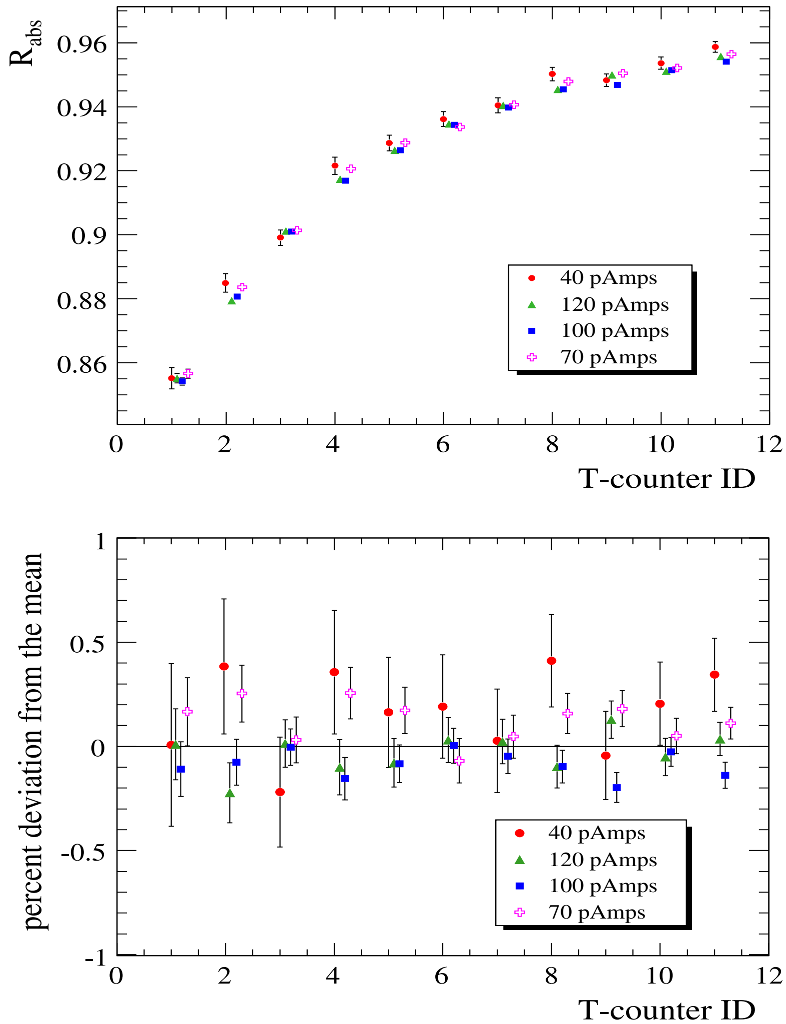

Figure 68: (top) Absolute tagging ratios plotted as a function of T-counter number for runs with different beam intensities, (bottom) The percent deviations from the mean for tagging ratio measurements made at different beam intensities for the first 11 T-counters.

with collimator at $7.02in$. Keeping in mind the required precision of 1% on the photon flux, it is important to investigate the extent to which the tagging ratios are affected by this shift.

The tagging ratios measured for five different positions are shown on Figure 71 (top). Figure 71 (bottom) shows the percent deviation of tagging ratios, measured at different positions of the collimator, from the value which was measured with the collimator in its nominal position (*i.e.* at $7.02in$). From Figure 71 (bottom) one can easily see that the shift in collimator position from $7.02in$ to $7.15in$ ($\sim 3.3mm$) lowers absolute tagging ratios by about 0.34%. One can also see that larger shifts in collimator position result in $\sim 1.2\%$ or more reduction in R_{abs}.

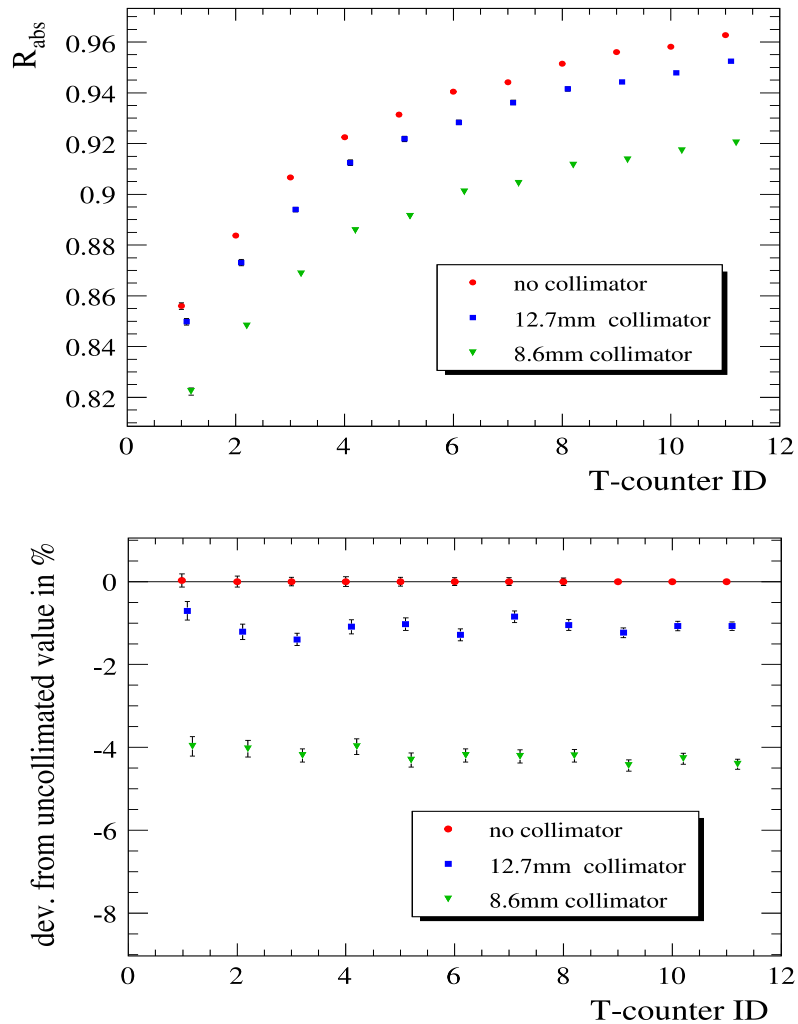

Figure 69: (top) R_{abs} measured for three different collimator sizes, (bottom). Percent deviation from the uncollimated value.

10.4 Effects of HYCAL scraping due to beam mis-steering (uncollimated beam)

The space between the pair spectrometer dipole vacuum window and the face of HYCAL is taken up by a helium bag. The HYCAL has a central opening to allow the uninteracted beam particles to pass through. A **G**amma **P**rofiler (GP) was installed directly behind the calorimeter to monitor the shape and the position of the photon beam during the experiment. Ideally, one would place the TAC at the position of the target, but given the technical constraints in the case of *PrimEx*, the TAC was mounted on the same moving platform as the GP behind HYCAL and was placed in the path of the photon beam interchangeably with the GP to perform a normalization run. In this configuration, the photons must travel

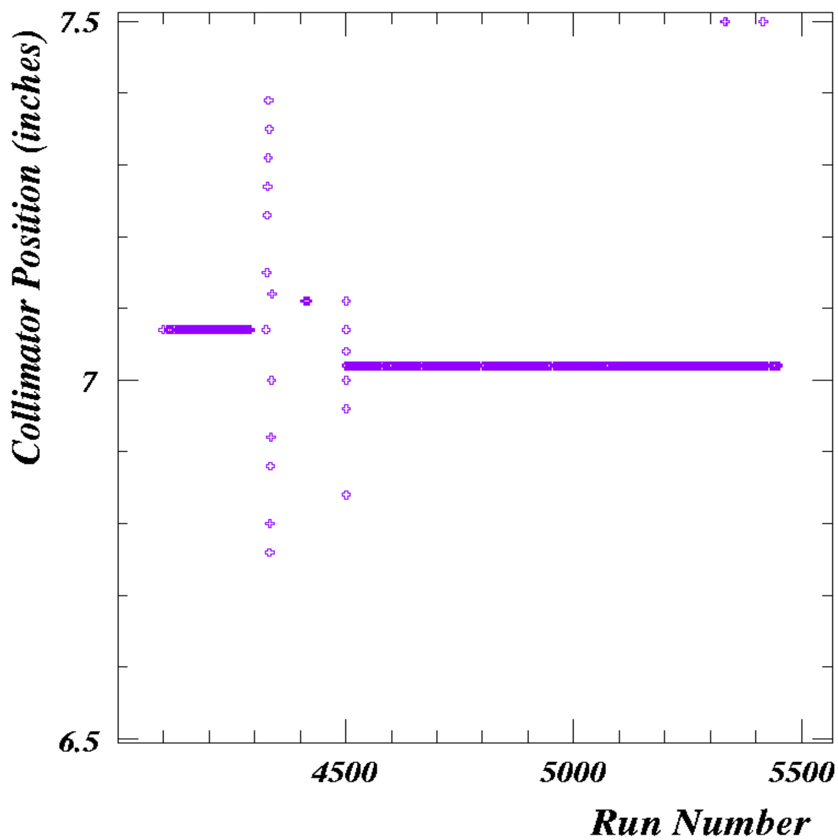

Figure 70: Collimator position vs. run number.

through a $4.15 \times 4.15 cm^2$ central opening in HYCAL before they can be registered in the TAC. Consequently, it is necessary to evaluate to what extent the size of the HYCAL central opening and the alignment of the photon beam with respect to the HYCAL axis affect the results of normalization runs. For this purpose the direction of the photon beam was purposefully altered and the tagging ratios were measured. To allow for larger artificial shifts in beam position, the collimator was retracted during this study. Due to the fact that this investigation was done with uncollimated beam it places an upper limit on the amount of the photon beam that can be cut by HYCAL due to scraping. Because the GP was mounted on the same moving platform as the TAC, photon beam position measurements were possible only before and after a normalization run. In light of this, the study described in this section should be considered only as qualitative exercise.

It was determined that in the absolute coordinate system of the GP, the nominal photon beam position is: $x_{av} = -0.83mm$ and $y_{av} = -1.45mm$. Figure 72 (top) shows several measurements of tagging ratios with different beam positions. Run 4338 was taken with the beam at its nominal position. For run 4340 the beam was steered a little over $5mm$ in positive y direction to $(-0.93, 4.09)$. For run 4341 the beam was at $(-6.54, -1.23)$. During run 4342 beam was at $(-9.45, -1.52)$ – *i.e.* about $8.5mm$ off of its nominal position. For run 4343 the beam was at $(5.12, -1.44)$ – *i.e.* about $6mm$ off of its nominal position.

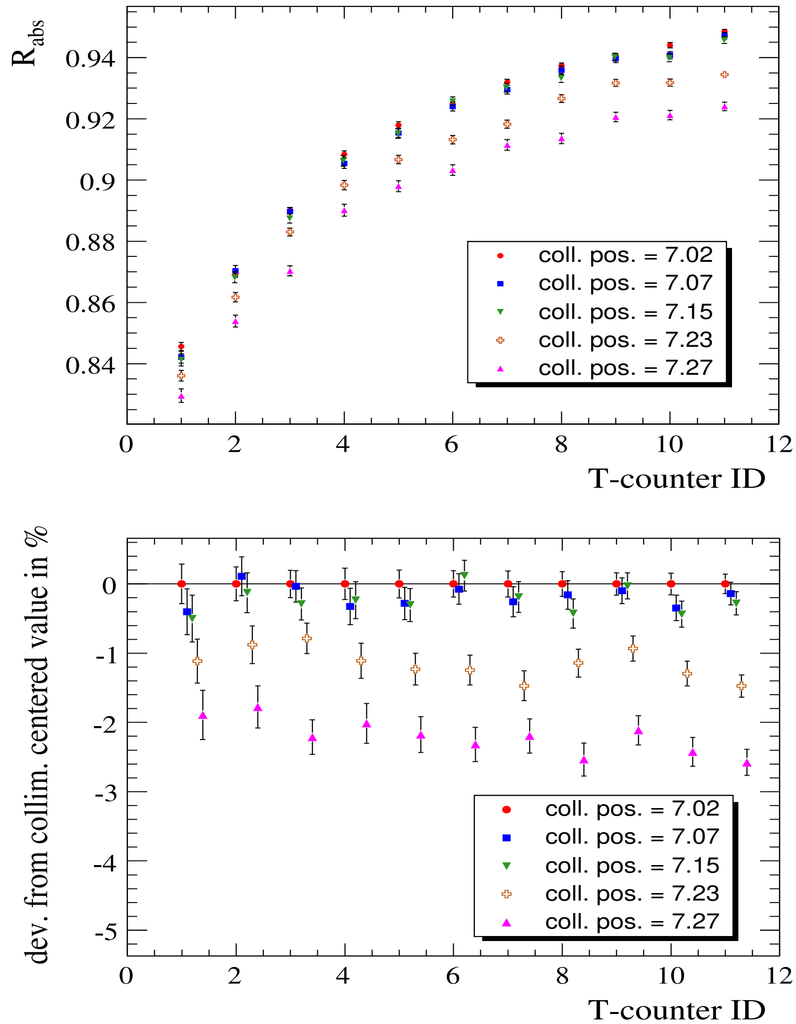

Figure 71: (top) R_{abs} measured for five different collimator positions measured in inches. (bottom) Percent deviation from the measurement taken with collimator in its nominal position ($7.02in$).

Runs 4342 and 4343 indicate that a $\sim 8.5mm$ shift in the beam position in the negative direction has the same effect on the tagging ratios as a $\sim 6mm$ shift in the positive direction along the x axis. Also runs 4340 and 4341 indicate a slight increase ($\sim 0.23\%$) in tagging ratios when the beam is steered $5mm$ in the positive y direction or $5mm$ in the negative x direction.

10.5 Long and short term reproducibility with uncollimated beam

To test our ability to perform a consistent measurement of the absolute tagging ratios, $R_{absolute}$, we had back-to-back normalization runs which were taken only $20 - 25$ minutes apart. The pair spectrometer magnet was operating at $\sim 900Amps$.

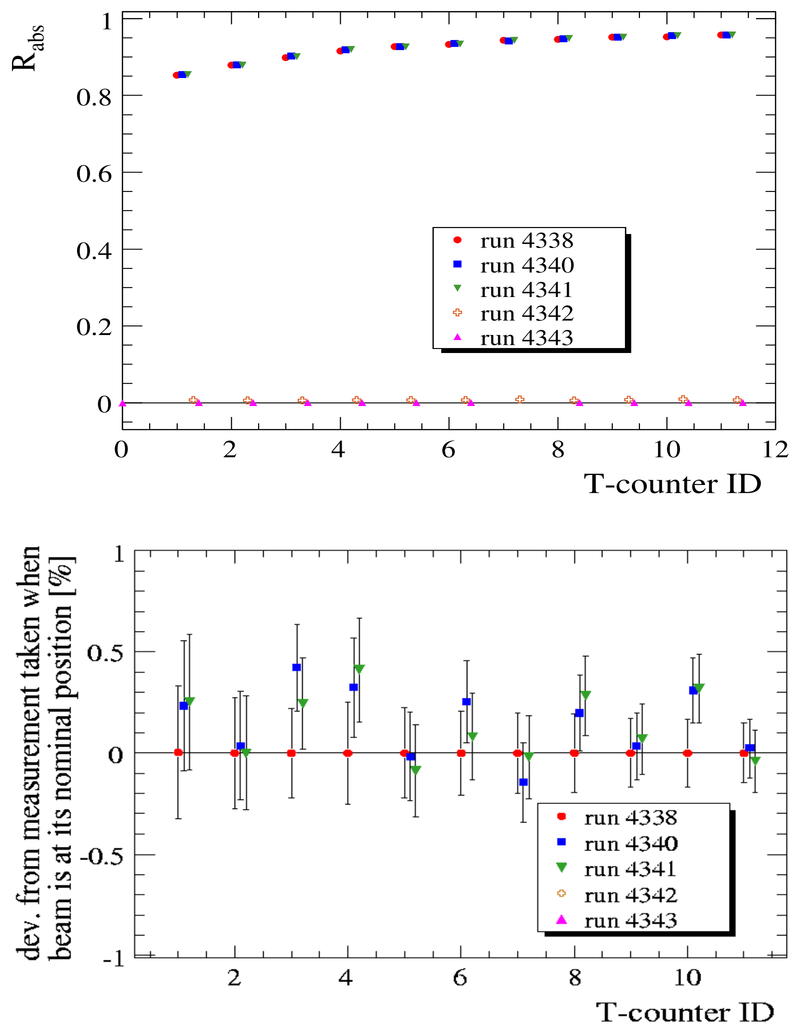

Figure 72: (top) R_{abs} measured for five different beam angles. (bottom) Percent deviation from the uncollimated value.

As can be seen from Figure 73, the study shows that all four runs agree within the limits of required precision and statistical errors. Figure 74 (top) shows the absolute tagging ratios measured for the first 11 T-counters. These runs were taken roughly four and a half hours and five days apart from each other. Figure 74 (bottom) shows the percent deviation of the tagging ratio for each T-counter from the relevant average value. The statistical error for each point is on the order of 0.2%. As seen from the plots, all three measurements are in very good agreement with each other (better than 0.3%). Note that since all three measurements were taken with different settings of the pair spectrometer dipole, this study also shows that there is no detectable dependence of absolute tagging ratios on the magnetic field of the pair spectrometer dipole when using an uncollimated photon beam.

10.6 Effects of the pair spectrometer dipole field with collimated beam

As demonstrated in Section 10.5, the pair spectrometer dipole field has no measurable effect on the tagging efficiencies in the case of an uncollimated photon beam. Due to technical difficulties with the pair spectrometer power supply, the normalization runs were performed at different values of the magnetic field of the pair spectrometer dipole, and the production data for *PrimEx* were taken with a 12.7mm collimator. It is therefore important to investigate the effect of the magnetic field on the tagging ratios measured for a collimated beam. The results of these studies are summarized in figure 75.

10.7 Absorption in the target

Some of the photons are absorbed in the target without producing a π^0. Special TAC runs with a carbon target placed in the beam were performed to study this effect. Figures 76 and 77 show a comparison of tagging efficiencies measured for target-in runs to those measured for target-out runs for measurements performed without and with photon beam collimation. Both studies yield consistent results indicating that $\sim 3\%$ of photons are lost in the target.

Since *PrimEx* is aiming for a $\sim 1.5\%$ level absolute cross-section measurement, one has to correct the yields for absorption of photons in the target. The main reaction of interest for *PrimEx*, ($\pi^0 \to \gamma\gamma$) and the consistency check reactions (Compton effect and e^+e^- production) are affected by the photon absorption in the target at different levels. In the case of Compton and Primakoff effects, not only the primary photon but also the secondary photons can be absorbed in the target. Since Compton scattering or π^o production can happen anywhere along the longitudinal direction of the target, the result of this study can be used to set an upper limit on the effect of photon absorption.

11 Appendix III: Target Thickness Determination

We propose to use two targets in this experiment, ^{12}C and ^{208}Pb. The carbon target is approximately 380 mil thick (5% R.L.) and uses Highly Ordered/Oriented Pyrolitic Graphite (HOPG) as the target material. The lead target is a rolled metal target approximately 12 mils thick (5% R.L.) and uses 99% enriched ^{208}Pb as the target material. The uncertainties in the effective areal densities of the carbon and lead targets are 0.05% and 0.43%, respectively. Both targets were utilized in the first *PrimEx* run. In this section, the methodology for mapping the effective areal densities of the targets ($atoms/cm^2$) and the estimated errors are described. Most details of the analysis can be found in *PrimEx* note #28.

A micrometer with precision of $\pm$ 0.05 mils was used to make a map of the thickness of the HOPG target. Figure 78 shows the micrometer map points, and the measured thicknesses in the central region of the target are also shown. The thickness varies by approximately 0.04% over the central region of the target. The mass density of the HOPG material was measured using the water immersion technique. HPLC grade water was used, which is submicron filtered, packed under inert gas, and has a maximum limit of impurities of 1 ppm. Corrections were made for the temperature dependence of the water density. A microgram scale was used to weigh the target block in air and in the water. The mass densities of two identical HOPG blocks were measured three consecutive times, and the results are shown in figure 79. The HOPG mass density used in calculating the areal density of the target was the average of the first five measurements (trial #6 was excluded), and the error in mass density is taken from trial #3.

Two corrections were applied to ρT to obtain the effective areal density of the target. The first correction is for impurities in the target, which can produce neutral pions through the Primakoff process. The second accounts for the attenuation of the incident photon beam in the target. The NIST XCOM data base was used to calculate the effect of incident beam absorption. Magnetic Primakoff production from ^{13}C is very small compared to Coulomb Primakoff production, and can be neglected. The final result for the effective number of ^{12}C $atoms/cm^2$ in the target is: $N_{eff}(Z = 6) = 1.0461 \times 10^{23} atoms/cm^2 \pm 0.05\%$.

The lead target was manufactured by Oak Ridge National Laboratory, and is a rolled foil of isotopically enriched ^{208}Pb, with 99% purity. The thickness of the target is approximately 12 mils, which corresponds to 5% radiation length. Because the target is a thin foil that can be easily damaged, direct measurements of foil thicknesses using a micrometer were considered risky. For this reason, an alternative method was devised which utilized x-ray attenuation to measure the foil thickness. X-rays from the 60 keV line in ^{241}Am were collimated to a spot size of approximately 2 mm in diameter. X-rays that passed through the target were detected in a 1 inch diameter NaI detector located behind the target foil. By comparing the attenuation of x-rays through the foil at various points, the thickness at these points can be determined. X-Y stepper motors were used to scan the lead target over the ^{241}Am source, and a map of x-ray attenuation *versus* target (x,y) was obtained. Two target scans were performed. The first was a run with 200 mil step sizes, and then a second run about a month later with 100 mil steps. Since the x-ray absorption constant for lead is not known with sufficient accuracy for our needs, the constant was measured at four off-center points on the target. This was done by taking x-ray attenuation and micrometer measurements at those points during the 200 mil and 100 mil step runs. Figure 80 shows the results of the study. For a given step size, the four measurements of x-ray absorption agree. However, there is a shift when comparing the results with the 200 mil step versus the 100 mil step size. To keep the analysis consistent, the 200 mil absorption constant was applied to the 200 mil step data, and the 100 mil absorption constant was applied to the 100 mil step data. The consistency of the analysis can be checked by verifying that the target thicknesses obtained in both scans agree within errors. The target thickness map from the 100 mil step scan is shown in Figure 81. The plot indicates a plateau near the center of the foil. The apparent increase in thickness at the very corners of the data is most likely caused by the target frame. Figures 82 and 83 show crosscuts through the lead target along the y and x axes, respectively. Results from both the 100 mil and 200 mil step scans are shown on the plots, and there is good agreement between the two data sets. The crosscuts clearly indicate a plateau near the center of the target that extends out to a radius of 200 mil. During the 2004 *PrimEx* run, the target ladder was positioned so that the beam went through the center of the lead target to take advantage of the relatively uniform target thickness in this area of the target. The areal density of the lead target was calculated using the average of lead mass densities listed in the literature. Corrections were applied to account for the effects of impurities in the target, and for attenuation of the incident beam. The result is $N_{eff}(Z = 82) = 9.875 \times 10^{20} \pm 0.43\% atoms/cm^2$.

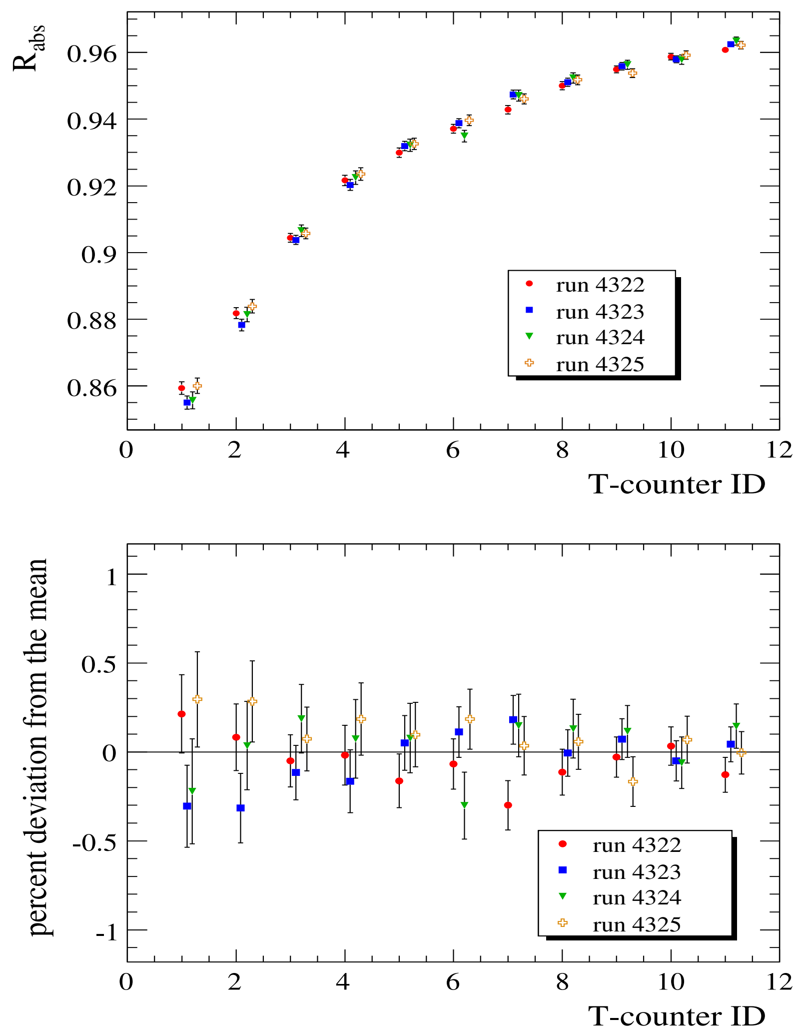

Figure 73: (top) R_{abs} measured for four consecutive runs. (bottom) Percent deviation from the mean.

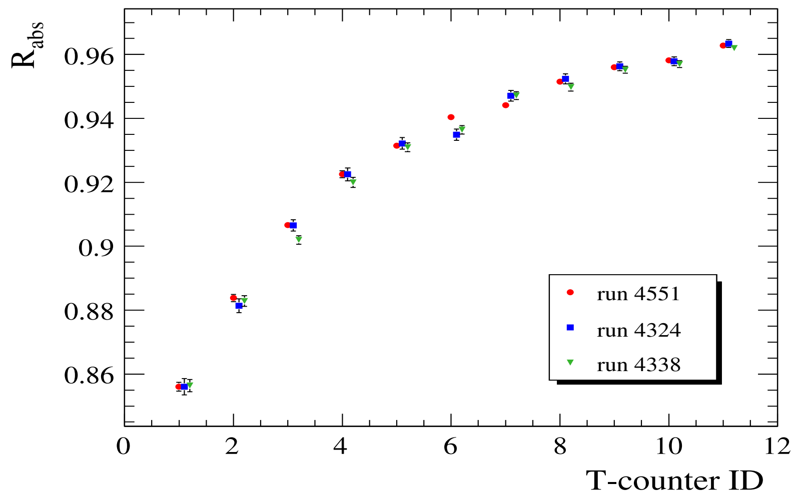

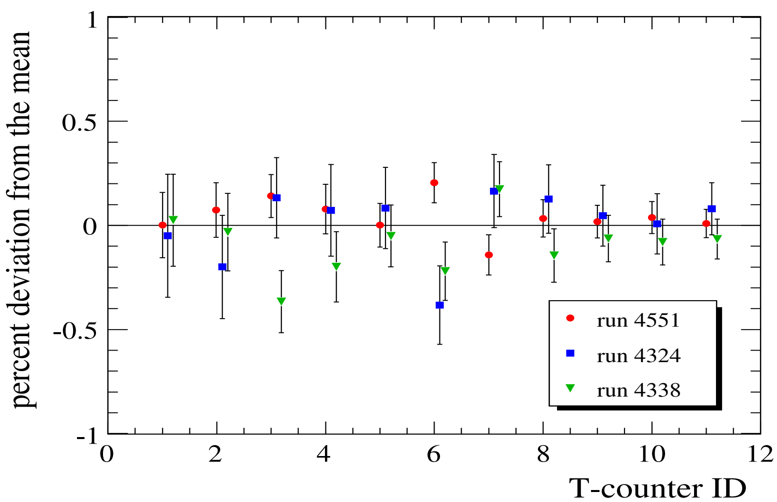

Figure 74: (top) R_{abs} measured for three runs which were separated in time during our data taking. (bottom) Percent deviation from the mean.

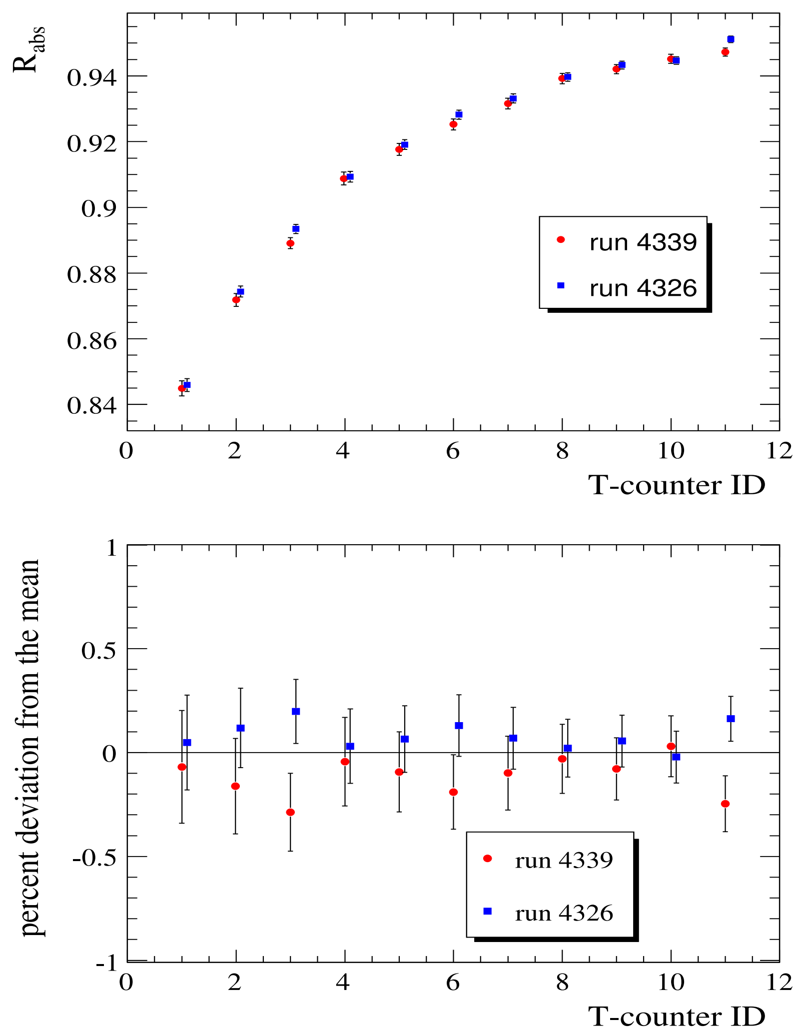

Figure 75: (top) R_{abs} measured for two runs which were taken with different settings of the pair spectrometer dipole magnet. (bottom) Percent deviation from the mean value.

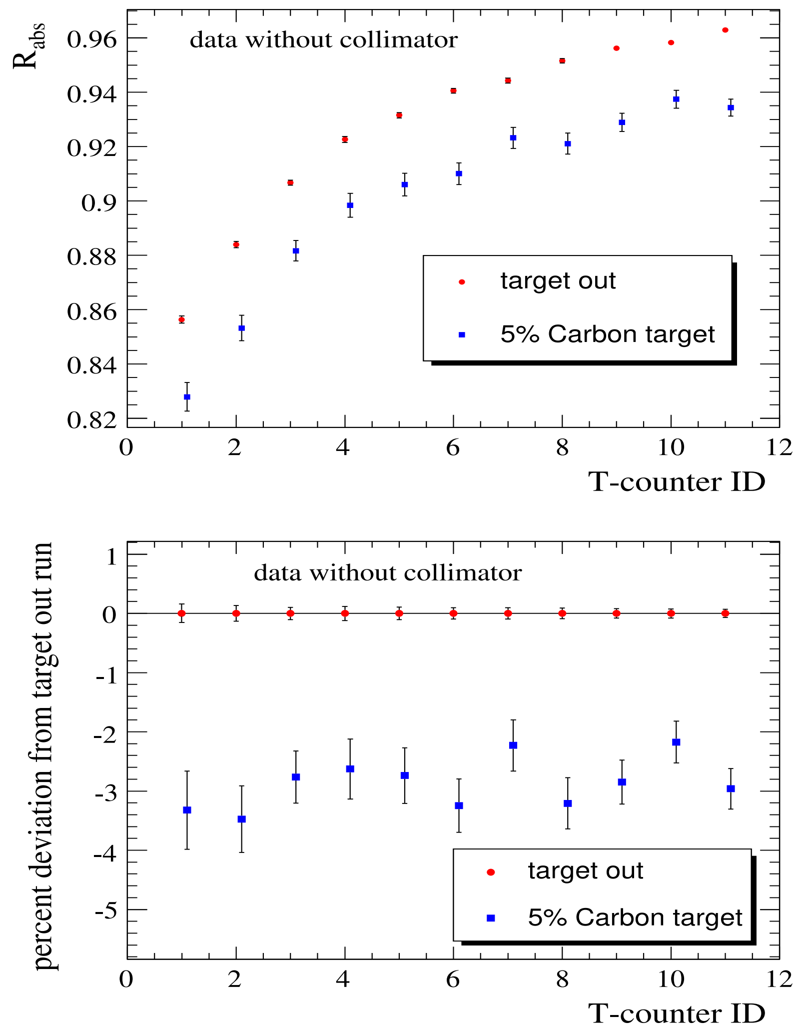

Figure 76: (top) R_{abs} measured for runs which were taken with target in and target out. (bottom) Percent deviation from the measurement obtained with physics target out; no photon collimation.

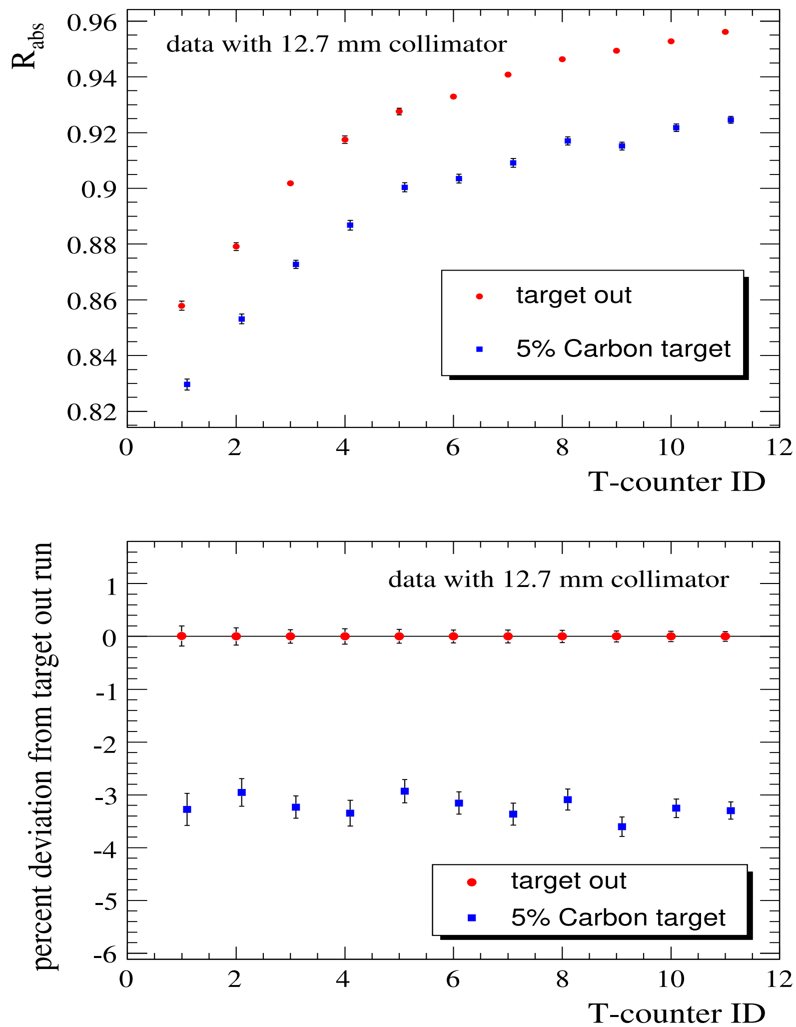

Figure 77: (top) R_{abs} measured for runs which were taken with target in and target out. (bottom) Percent deviation from the measurement obtained with physics target out; with photon collimation.

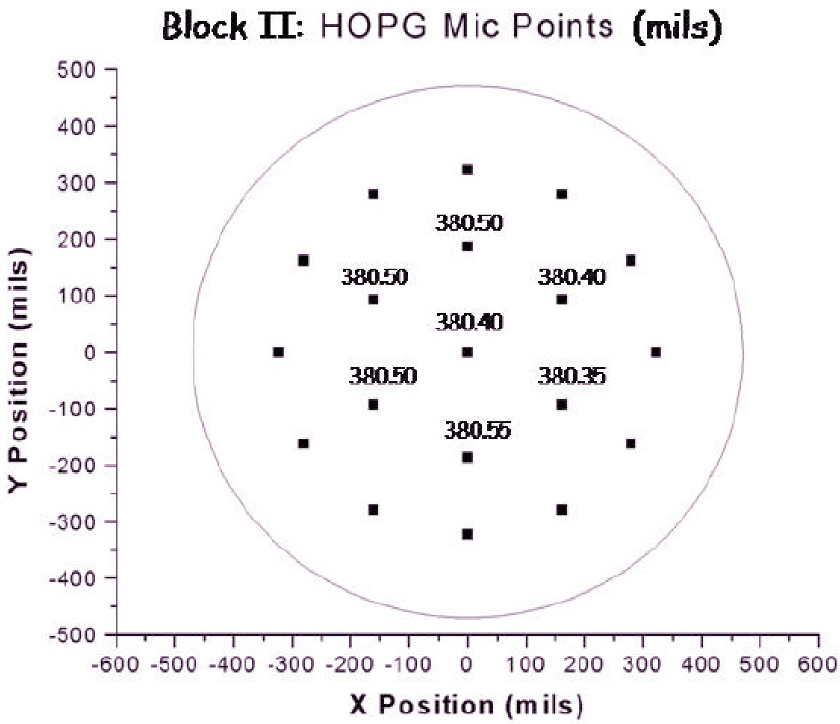

Figure 78: Thickness map of the HOPG target. Units are in mils.

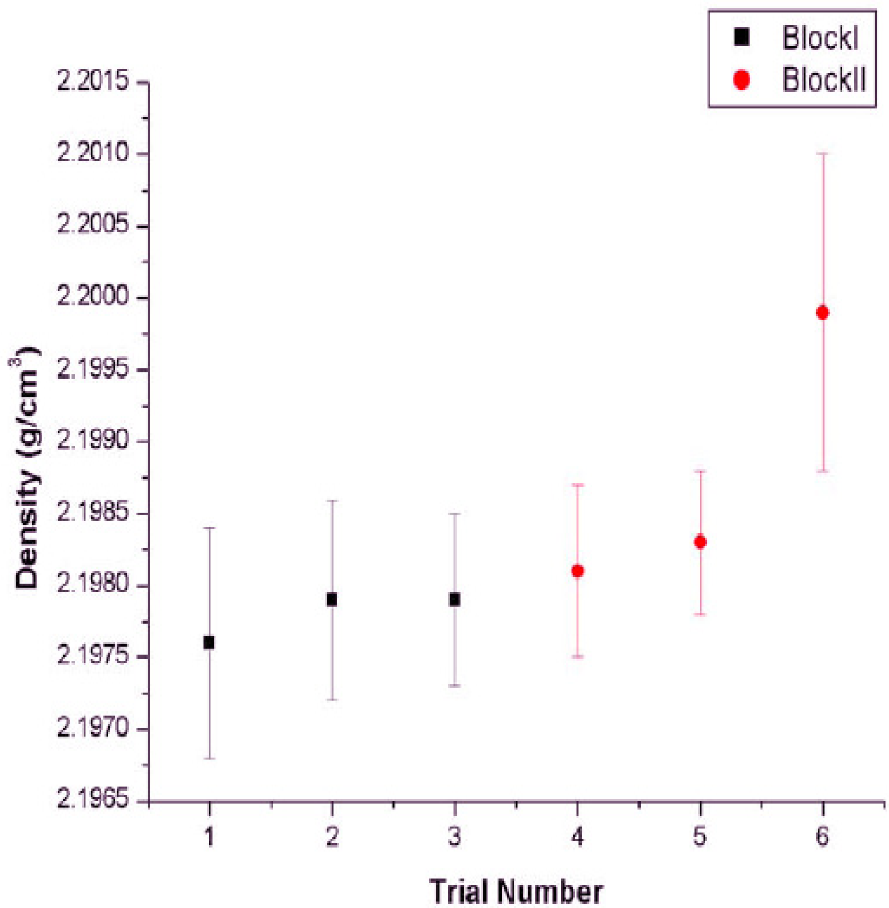

Figure 79: HOPG density measurements.

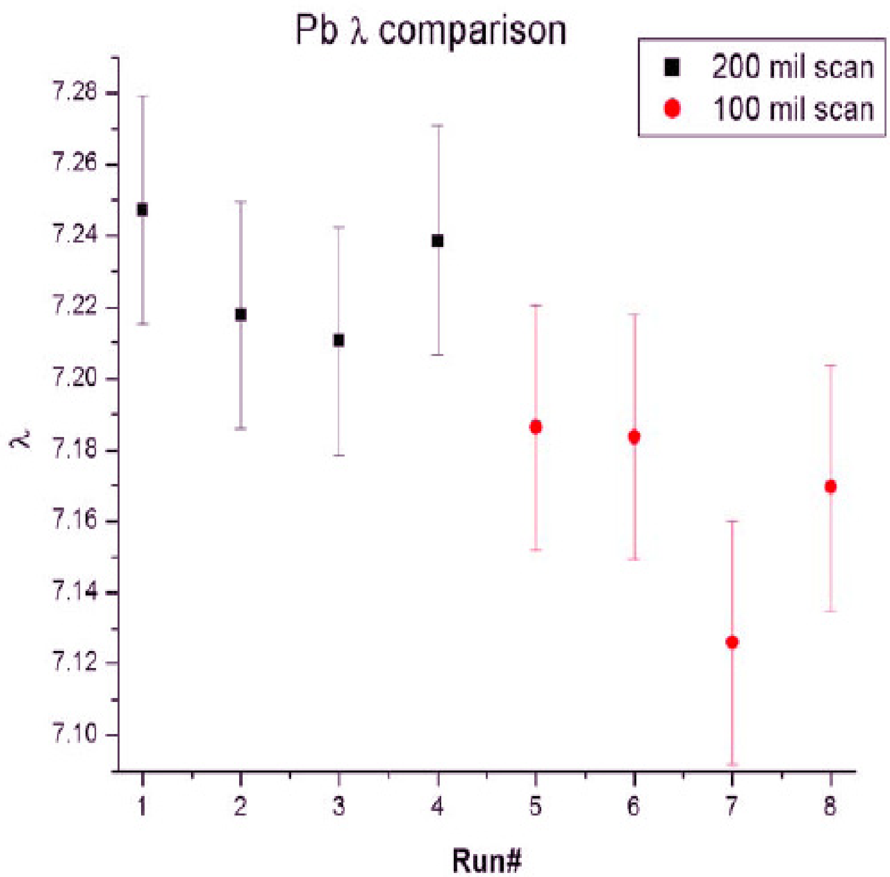

Figure 80: Measured x-ray absorption constants for the lead target.

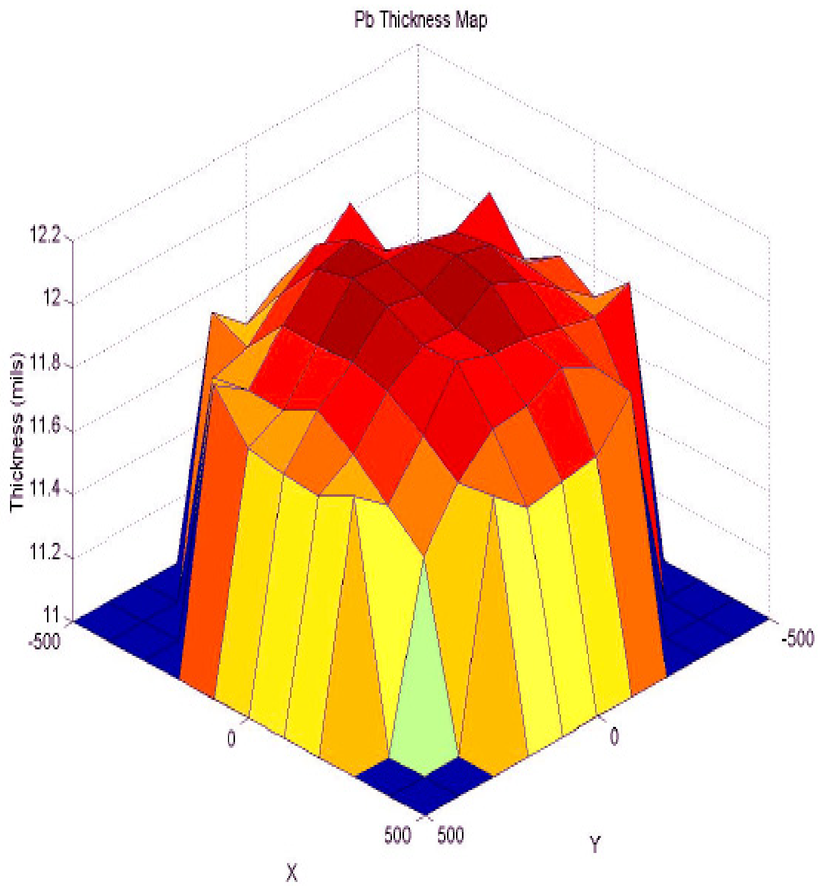

Figure 81: Lead target thickness map measured on a 100 mil grid.

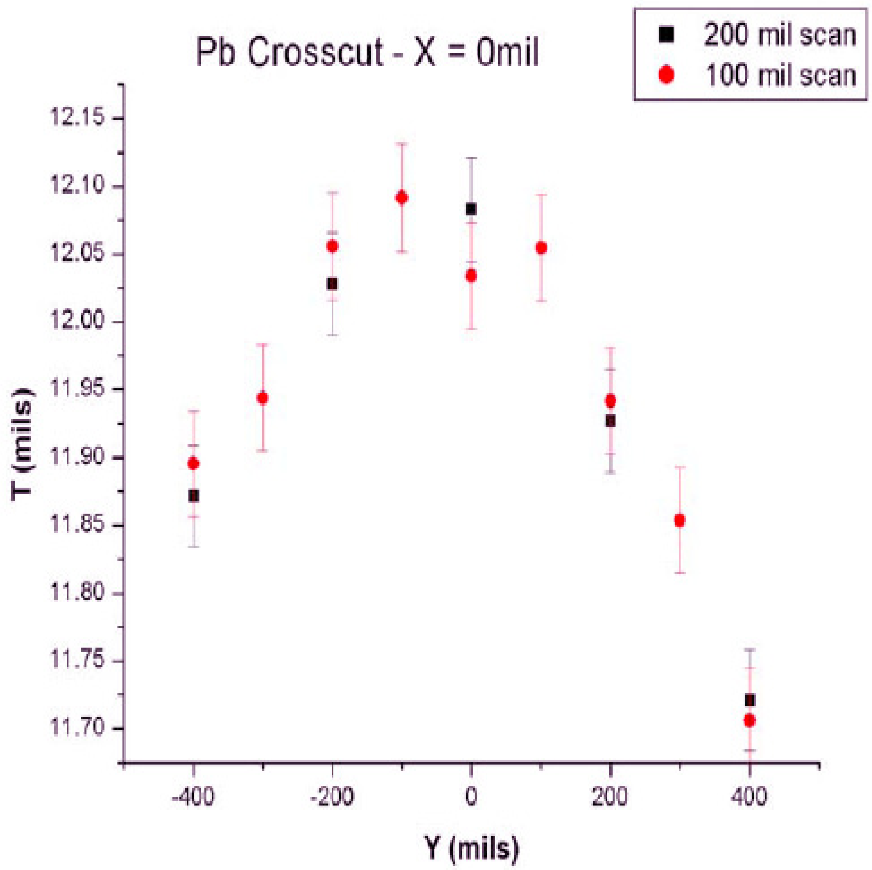

Figure 82: Crosscut of the lead target along the y axis.

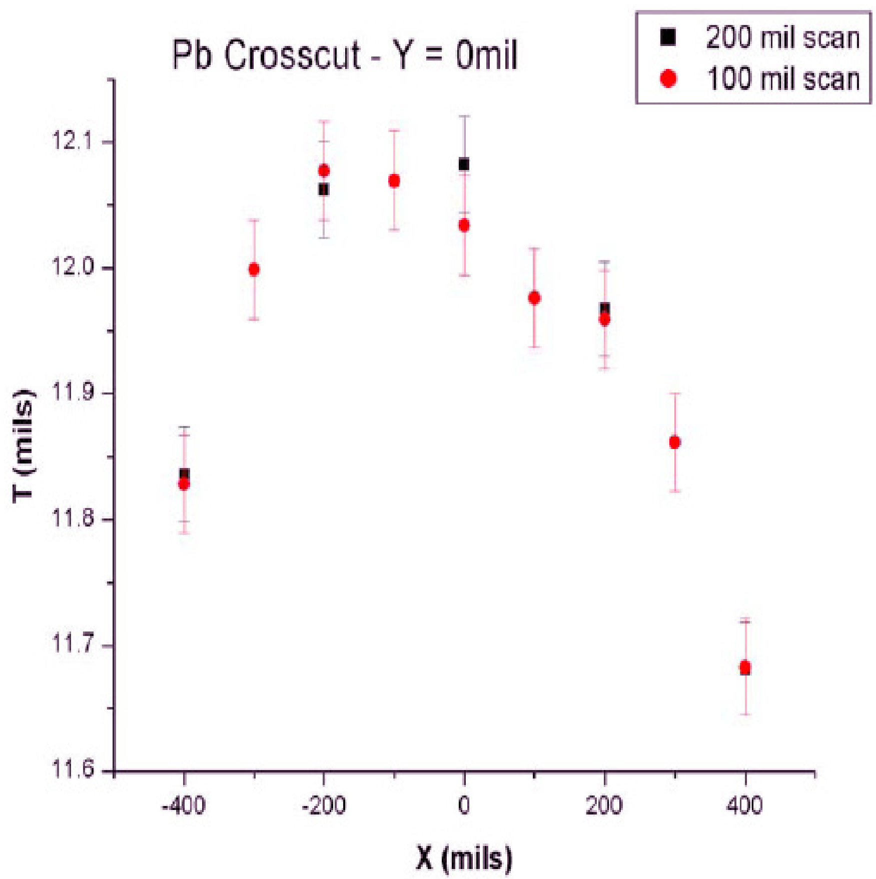

Figure 83: Crosscut of the lead target along the x axis.